FLOATECH

D1.2. Higher Order Hydroelastic Module

DATE OF DELIVERY - 23/12/2021

AUTHORS – JOSEPH SAVERIN, SEBASTIAN PEREZ-BECKER, ROBERT BEHRENS DE LUNA, DAVID MARTEN, JEAN-CHRISTOPH GILLOTEAUX, RUDDY KURNIA

TECHNICAL UNIVERSITY OF BERLIN

This project has received funding from the European Union's Horizon 2020 research and innovation programme under grant agreement No 101007142

FLOATECH
THE FUTURE OF FLOATING WIND TURBINES

Document track details

Project acronym	FLOATECH
Project title	Optimization of floating wind turbines using innovative control techniques and fully coupled open-source engineering tool
Starting date	01.01.2021
Duration	36 months
Programme	H2020-EU.3.3.2. - Low-cost, low-carbon energy supply
Call identifier	H2020-LC-SC3-2020-RES-RIA
Grant Agreement No	101007142

Deliverable Information	
Deliverable number	1.2
Work package number	1
Deliverable title	Higher Order Hydroelastic Module
Lead beneficiary	TU Berlin
Author	Joseph Saverin
Due date	31.12.2021
Actual submission date	23.12.2021
Type of deliverable	Report
Dissemination level	Public

Version management

Document history and validation			
Version	**Name**	**Date**	**Comment**
V 0.1	TU BERLIN	01/12/2021	First draft
V 0.2	Alessandro Bianchini	14/12/2021	General comments on structure
V 0.2	Daniel van den Berg	14/12/2021	Grammatical and structural comments
V1.1	Guillaume Ducrozet	22/12/2021	Comments on theory sections.
V2.0	Joseph Saverin	23/12/2021	Final Version complete.

Background: about the FLOATECH project

The FLOATECH project is a Research and Innovation Action funded by the European Union's H2020 programme aiming to increase the technical maturity and the cost competitiveness of floating offshore wind (FOW) energy. This is particularly important because, due to the limitations of available installation sites onshore, offshore wind is becoming crucial to ensure the further growth of the wind energy sector.

The project is implemented by a European consortium of 5 public research institutions with relevant skills in the field of offshore floating wind energy and 3 industrial partners, two of which have been involved in the most recent developments of floating wind systems.

The approach of FLOATECH can be broken down into three actions:

- The development, implementation and validation of a user-friendly and efficient design engineering tool (named QBlade-Ocean) performing simulations of floating offshore wind turbines with an unseen combination of aerodynamic and hydrodynamic fidelity. The advanced modelling theories will lead to a reduction of the uncertainties in the design process and an increase of turbine efficiency.
- The development of two innovative control techniques (i.e. Active Wave-based feed-forward Control and the Active Wake Mixing) for Floating Wind Turbines and floaters, combining wave prediction and anticipation of induced platform motions. This is expected to improve the performance of each machine and to minimise wake effects in floating wind farms, leading to a net increase in the annual energy production of the farm.
- The economic analysis of these concepts to demonstrate qualitatively and quantitatively the impact of the developed technologies on the Levelized Cost of Energy (LCOE) of FOW technology.

In addition to the technological and economic impacts, the project is expected to have several impacts at societal, environmental and political levels, such as: public acceptance, due to no noise and visibility issues of FOWT; very low impact on biodiversity and wildlife habitat because no piles are needed be to installed into the seabed; the use of less material and space thanks to an environmentally friendly design; the promotion of the installation of FOW in transitional water depths (30-50 meters), as the costs for FOW at those locations will become more competitive compared to the fixed bottom foundations.

Table of contents

List of acronyms and abbreviations

Acronym / Abbreviation	Meaning / Full text
BEM	Blade element-momentum
FEM	Finite Element Method
FOW	Floating Offshore Wind
FOWT	Floating Offshore Wind Turbine
DOF	Degree of Freedom
GUI	Graphical User Interface
IRF	Impulse Response Function
LCOE	Levelised Cost of Energy
LPMD	Linear Potential Flow with Morison Drag
ME	Full Morison Equation
MCFC	MacCamy-Fuchs Correction
OF	OpenFAST
QB	QBlade Ocean
TLP	Tension Leg Platform

List of applied units

SI Units have been used everywhere.

Dimension	Unit
Time	Seconds [s]
Length	Meters [m]
Frequency	Hertz [Hz][1/s]
Force	Newton [N]
Moment	Newton meters [Nm]

EXECUTIVE SUMMARY

This document is a deliverable of the FLOATECH project, funded under the European Union's Horizon 2020 research and innovation programme under grant agreement No 101007142.

Global dynamic analysis of a single offshore (potentially floating) wind turbine is in itself a challenge as it involves strong interactions between the elastic turbine, its control system, its support and mooring system. This requires multiphysics modeling including aerodynamics, hydrodynamics, and structural dynamics. Over the last decade, numerous numerical simulation tools have been developed, mostly coupling offshore design tools including various hydrodynamic solvers to aero-elastic solvers used to design wind turbines.

In general, these simulators have an excellent accuracy and CPU time ratio which allows them to be used regularly in design offices for the analysis of the dynamic behavior of floating wind turbines. These simulators are sufficient to assess the global response of the system under combined wind and wave conditions but have certain limitations. In particular, they do not allow the structural dimensioning of the floating support since they often model a flexible wind turbine (tower and rotor) supported by a rigid platform. This form of "rigid-flexible" coupling ignores the flexible modes of the platforms. This design step is then performed in a decoupled way using a structural solver modeling the platform by means of a finite element formulation and considering only static loadings or linear wave loadings. While this approach can be sufficient for medium power rotors, the development of 10+MW rotors will require foundations of large dimensions for which hydroelastic effects will become significant.

To overcome this problem, recent works propose coupling approaches between hydrodynamic solvers and structural solvers [1, 2, 3, 4]. The hydrodynamic loads are then no longer represented in the form of a single force vector applied at a single point, but rather are applied in a distributed manner over the whole structure. Depending on the approach, the hydrodynamic loads are calculated either using a Morison formulation or a linear potential flow model. The structural deflections are modeled either directly through a finite element model or on the rigid and flexible structural modes of the platforms. The results of these works show that taking into account the flexibility of the structure can have a significant influence on the distribution of internal loads, on the structural resonance periods and consequently on the dimensioning.

QBlade Ocean (hereafter QB) follows the same trend aiming to be a tool used for the design of 10+MW floating wind turbines and so being able to calculate the structural response of floating platforms. This document presents an overview of the different numerical models that have been implemented into the hydrodynamic module of QB as well the coupling that has been made with the structural solver. The results of a step-by-step verification and validation process are successively presented. The results show that QB is able to simulate the wave-induced motions of various types of floating platforms under regular or irregular wave conditions by means of different modelling approaches. It shows that QB has results comparable to OpenFAST solver. Finally, preliminary results on the hydroelastic response of a floating wind turbine platform are presented.

1. INTRODUCTION

1.1 CONTEXT WITHIN FLOATECH

This report summarises all the work done in Task 1.2 of Work Package 1 related to the hydroelastic modelling of floating wind turbines. The goal of this report is to give a brief overview of the modelling methods in the literature, to introduce the theoretical background of the numerical solver implemented within QB as well as all the verification and validation work.

1.2 REPORT STRUCTURE

To put the FLOATECH hydroelastic modelling strategy into context, a brief state-of-the-art of the hydrodynamic models and the structural models is given in Section 2. Next, Section 3 details the theoretical background of the models used in QB and explains how the coupling between the hydrodynamic module and the structural solver is implemented. The verification and validation results are presented in Section 4.

2. HYDROELASTIC MODELLING STATE-OF-THE-ART

2.1 HYDRODYNAMIC MODELLING

2.1.1 Wave models

The main source of loading on floating platforms in the ocean are wind waves. Their description in the literature most commonly rely on the potential flow formalism, assuming a perfect fluid.

Additional hypotheses are made in order to come up with a simple description of the wave propagation and of the underlying kinematics, necessary to evaluate the loadings on the structure of interest (see Sections 2.1.2 and 2.1.3). In this context, the steepness of the wave (ratio of wave height H over wavelength λ) and dispersion parameter (ratio of water depth d over λ) play a key role.

The classical weakly non-linear dispersive wave theory (Stokes theory) assumes a small steepness as well as a sufficient water depth (i.e. dispersion parameter not too small) for the description of regular (harmonic) waves. It leads to the possible use of what is referred as the linear wave theory, which is the most simple and widespread way of describing analytically wave kinematics in ocean engineering. A detailed description is provided in Sec. 3.2.1. In the case of regular waves, the inclusion of nonlinearities is straightforward up to Stokes 5^{th} order, which is considered in different software packages as an accurate description of nonlinear dispersive wave kinematics.

For the description of real sea states (irregular waves), the linear approach consisting of a simple superposition of regular (harmonic) wave solutions is the current state-of-the-art. The inclusion of non-linearities at second-order is possible analytically but may be time-consuming when considering a large number of frequency components [5]. For higher-order nonlinearities, the use of numerical solutions is mandatory. A wide range of nonlinear numerical wave solvers have been developed in the recent decades and an example is provided in Sec. 3.2.1.

2.1.2 Morison's equation

Morison's equation allows the calculation of the transverse hydrodynamic forces applied on slender structures where the diameter is small compared to the wavelength. In this formulation [6], it is assumed that the wave-induced load is composed of two components: a drag force, and an inertial force. It has a nonlinear viscous drag term as well as an added mass term, making it applicable for both steady current-type loads as well as unsteady forces from waves or body motions. Drag and added mass terms are both obtained empirically through experiments or CFD calculations. Traditionally, Morison's equation is combined with strip theory in order to take into account the effects of rotational motions and non-uniform water kinematics. In strip theory the body is discretised into a finite number of sections and calculates the forces on each section independently. The main disadvantage of this approach is the prohibitive computational time resulting from the large number of degrees of freedom to be considered.

Morison's equation is convenient due to its simplicity of implementation. Originally, the method was proposed for the calculation of wave forces on piles in the oil & gas industry. As a consequence, this formulation is only applicable for calculating the hydrodynamic loads on slender structures when the effects of diffraction and radiation damping are negligible, and flow separation may occur. For larger diameter structures such as SPAR platforms [7], wave diffraction effects are sometimes accounted for by the use of the McCamy & Fuchs theory [8], which modifies the inertial term. One of the drawbacks of this method lies in its inability to handle coupling between the different degrees of freedom with regards to added mass and to neglecting the hydrodynamic heave forces. It can also be combined with a potential flow method (see Section 2.1.2.2) for modelling slender structures such as struts and pontoons which are commonly used for semi-submersible or TLP floating platforms. For the analysis of platform flexibility, Morison-based approaches [9] are commonly coupled with a structural solver based on a Finite Element Model (see Section 2.2.2).

2.1.3 Boundary elements method (BEM)

Boundary elements methods, also called panel methods, are based on potential flow theory [10]. The flow field is assumed to be inviscid and irrotational, the hydrodynamic problem is solved to second-order in incident wave amplitude.

The first-order solution corresponds to the linear solution where the oscillation amplitudes of the fluid and the body are assumed small relative to the cross-sectional dimension of the body. By assuming small amplitude motions, the position of the body is linearised around its equilibrium position. The hydrodynamic problem is thus solved on the mean free surface elevation. By assuming small wave amplitude, the free surface is linearised around the mean sea level. The hydrodynamic problem is thus solved on the mean wetted surface. The fluid-structure problem is decomposed into a scattering problem where the structure is held fixed and a sequence of radiation problems where the structure in turn is forced to oscillate in the absence of any incident wave. The total hydrodynamic force is then decomposed into three terms: buoyancy stiffness forces, radiation forces, and scattering forces (also called excitation forces).

The second-order solution corresponds to the terms (velocities, pressures, amplitudes) that are either linear or proportional to the square of the wave amplitude. Many different numerical procedures are available for the computation of these terms. In comparison to the first-order solution, the second-order solution provides mean (drift), low-frequency, and high-frequency forces. When the floating platform is considered fixed, most of the design tools that are currently used for the simulation of floating offshore wind turbines enable the calculation of linear and 2nd-order wave-induced loads [11]. They are commonly combined with Morison elements for the modelling of struts or heave plates. They are also usually combined with strip methods to take into account drag forces. The second-order solution is used especially for the low-frequency response of semi-submersible platforms or the high-frequency response of TLP platforms [12].

For the analysis of platform flexibility, BEM solvers can also be used. Three main modelling approaches have been proposed. The first approach splits the floating structure into several bodies, each of them being considered as an independent body. Within this multibody approach, the hydrodynamic interactions between each body are taken into account. It also outputs distributed loadings along the structure facilitating coupling with a structural solver. The second approach splits the floating structure into several sections [1]. This approach takes the benefit of a single body BEM calculation but outputs the hydrodynamic coefficients for different preselected sections (see Figure 1). This approach enables distributed loading across the platform that can be straightforwardly coupled to a structural solver while keeping a much faster computational time than the multibody strategy previously introduced. It nevertheless has the disadvantage of not providing coupled radiation terms between the considered sections.

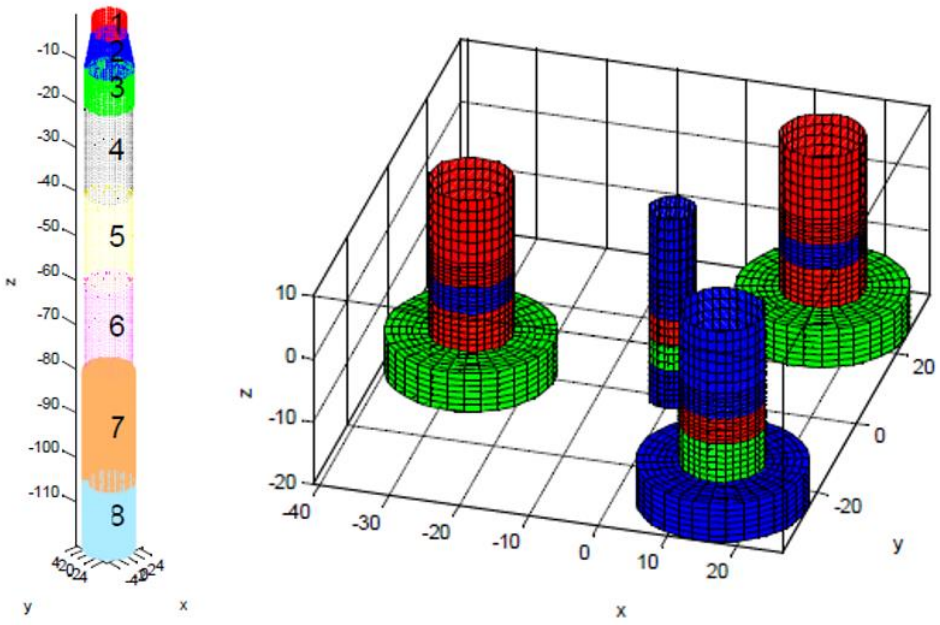

Figure 1: Example of a SPAR platform (left) and semi-submersible platform (right) discretised into sections [Alexandre, 2018].

The third approach [2] is based on a modal decomposition (see Section 2.2.1) of the structural deformation. Here the hydrodynamic boundary problem is not only solved for the six rigid structural modes of the platform but as well for the flexible structural modes. This approach has the advantage of dealing with all the hydrodynamic interactions from the structure deformations without greatly increasing the computational time.

2.2 STRUCTURAL MODELLING

2.2.1 Finite element models (FEM)

Finite elements methods consist in approximating the displacement of a structure by interpolation of the displacement between nodes placed on the structure. The interpolation is chosen such that one can divide structures into relatively small elements where each element includes a number of nodes, which depends on the element type (see Figure 2). The structure is then discretised into a mesh of finite elements interconnected at nodes. Every node has 3 translational and 3 rotational degrees of freedom. The elements can be 1-dimensional to model 1D slender structures (bar and beam elements), 2-dimensional (shell elements with isotropic or anisotropic behaviour to model composite layups), or even 3-dimensional with solid elements. Current floating offshore wind turbine software are generally limited to 1D elements, but 2D shell elements can also be used. Sectional properties associated with 1D and 2D elements are affected by these elements. In particular, beam section properties must include axial, bidirectional bending, and torsion inertia and stiffness. Non-linear stiffness properties may also be modelled.

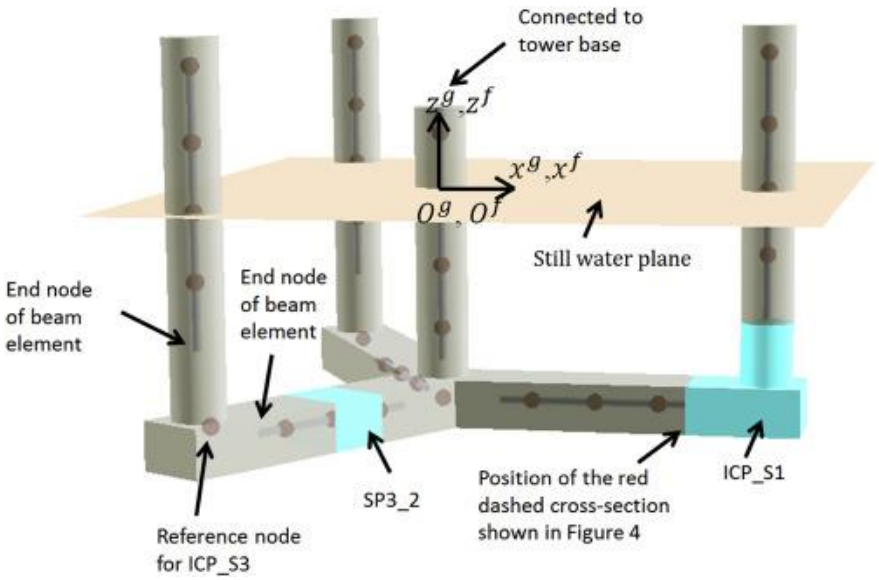

Figure 2: Example of finite element model of the hull of a semi-submersible platform [Luan et al., 2017].

The main advantage of finite element modelling is its ability of modelling complex structures with a high level of detail with a moderate number of degrees of freedom. Another important advantage is its capability of taking into account geometric and material non-linearities, large displacements, rotations and deflections. The main drawback of finite element methods is their high computational cost, since a

large number of degrees of freedom are to be considered. Depending of the system dynamic, simulations may be relatively slow in comparison to alternative methods.

2.2.2 Modal representation

Modal representation consists of approximating the displacement of a structure as a combination of its vibration modes (see Figure 3). In a dynamic analysis, this allows simplifying the computation of motion. Thus, by construction, the variation of the amplitude of each mode with time can be determined separately, with uncoupled 'modal' equations. The results from each of the modal equations are then superimposed to give the full response. In this approach, the fundamental mode shapes and frequencies of the structure need to be first computed by means of a modal analysis carried out with finite element software or given experimentally. The eigenmodes are then superimposed and coupled together for the computation of the dynamic response of the whole structure. The main advantage of such a method is a low number of degrees of freedom giving very efficient and fast computational times in comparison to approaches based on FEM. It is however limited to structures experiencing small deflections.

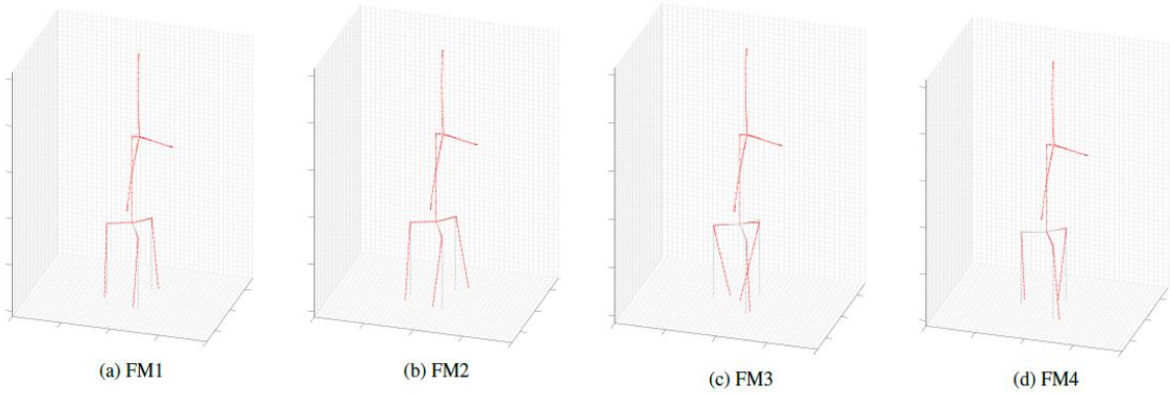

Figure 3: Example of flexible mode shapes of a semi-submersible platform [Borg, 2017].

2.3 REFERENCES

[1] Alexandre, A. et al., 2018. *Methodology for calculating floating offshore wind foundation internal loads using bladed and a finite element analysis software*. Proc. of the 37th International Conference on Ocean, Offshore and Arctic Engineering.

[2] Borg, M. et al., 2016. *Floating substructure flexibility of large-volume 10MW offshore wind turbine platforms in dynamic calculations*. Journal of Physics: Conference Series Volume 753, Issue 8.

[3] Borg, M. et al., 2017. *Elastic deformations of floaters for offshore wind turbines: dynamic modelling and sectional load calculations*. Proc. of the 36th International Conference on Ocean, Offshore and Arctic Engineering.

[4] Luan, C. et al., 2017. *Development and verification of a time-domain approach for determining forces and moments in structural components of floaters with an application to floating wind turbines*. Marine Structures Vol. 51, 87-109.

[5] Dalzell, J. F., 1999. *A note on finite depth second-order wave–wave interactions*. Applied Ocean Research, 21(3), 105-111.

[6] Morison, J. et al., 1950. *The forces exerted by surface waves on monopiles*. J. Petrol. Tech., Vol. 189, pp 149-154.

[7] Bachynski, E., 2014. *Design and Dynamic Analysis of Tension Leg Platform Wind Turbines*. Doctoral theses at NTNU, 2014:86.

[8] Mac Camy, R. C., Fuchs, R. A., 1954. *Wave forces on piles: a diffraction theory*. Technical Memorandum NO.69.

[9] Jonkman, J. et al., 2020. *Implementation of Substructure Flexibility and Member-Level Load Capabilities for Floating Offshore Wind Turbines in OpenFAST*. Proc. Of EERA DeepWind.

[10] Newman, J., 1980. *Marine hydrodynamics.* 3rd ed., the MIT Press, 1980.

[11] Robertson, A. N. et al., 2017. *OC5 Project Phase II: Validation of Global Loads of the DeepCwind Floating Semisubmersible Wind Turbine*. Energy Procedia 137 (2017) 38–57.

[12] Roald, L. et al., 2014. *The Effect of Second-Order Hydrodynamics on a Floating Offshore Wind Turbine*. Technical Report NREL/TP-5000-61452.

3. HYDROELASTIC MODELLING WITHIN QBLADE OCEAN

In order to enable a comprehensive overview of the implementation and modelling approaches within QB, a summary is provided initially in Section 3.1. The structural model which underlies the time integration framework of QB is described in Section 3.2. The transition to modelling the wind turbine in offshore environments requires a thorough understanding of wave kinematics and sea states. These are described in Section 3.3. In Sections 3.4 and 3.5 theoretical aspects of the implemented hydrostatic and hydrodynamics models are described with emphasis being placed on important physical variables. A comprehensive verification of QB with a range of offshore architectures is carried out in Section 3.6.

3.1 GLOBAL DESCRIPTION OF QBLADE OCEAN TOOL

QB is an essential aspect of the Floatech project. The software presented in this section builds upon the existing program QBlade. QBlade [1] is a state of the art multi-physics code, covering the complete range of aspects required for the aero-servo-hydro-elastic simulation of horizontal and vertical axis wind turbines. QBlade is under development at the Technical University of Berlin since 2010, and is realised as a modular implementation of highly efficient multi-fidelity aerodynamic, structural dynamic and hydrodynamic solvers in a modern, object oriented C++ framework. QBlade is equipped with a fully featured graphical user-interface that aids during simulation setup, visualization and results post-processing. Within WP1 of the Floatech project QB is extended with functionality to design and simulate bottom-fixed or floating offshore turbine substructures and their hydrodynamic behavior.

QB leverages the current computer architecture by thoroughly utilizing CPU (via OpenMP) and GPU (via OpenCL) parallelization techniques for a high numerical performance. This allows to run simulations with advanced physical models of thousands degrees of freedom with high performance. QB is a platform independent software, and can be deployed on workstations or clusters running Windows, Unix or MacOS based operating systems. QB is equipped with an intuitive graphical user interface that aids the user

during the whole wind turbine design process. All turbine and simulation details are readily available to be accessed and modified in a logical well-structured and tested interface.

Simulation results are presented in dynamic graphs that give insight into every simulation detail. Simulations and turbine designs are fully rendered in real time to aid with the comprehension and evaluation of our complex multi-physics models. QB allows the serialization of the complete model data, setup and results into project files to enable simple sharing and collaboration of complex simulation and turbine design projects. The Community Edition (CE) of QB is freely available to everyone under the open-source GNU GPLv2 license. Upon the completion of WP1, the software will include the necessary features to model offshore wind turbines.

QB uses a highly optimised and thoroughly validated lifting line free vortex wake method for its aerodynamic calculations. Instead of approximating the wake aerodynamics with the steady-state blade element-momentum method (BEM), the rotor wake is explicitly modeled through Lagrangian vortex elements. This results in a more accurate and detailed spatial and temporal representation of the rotor induction when compared to BEM approaches and fully resolves the velocity distribution behind the rotor [2]. This allows assessment of wind turbine wake interaction, accurately accounts for the aerodynamics of oscillating floating wind turbine structures and explicitly resolves unsteady vertical axis wind turbine wake dynamics [3]. As an alternative with lower computational demand the aerodynamics of horizontal-axis wind turbines can be simulated using an unsteady polar-BEM implementation [4].

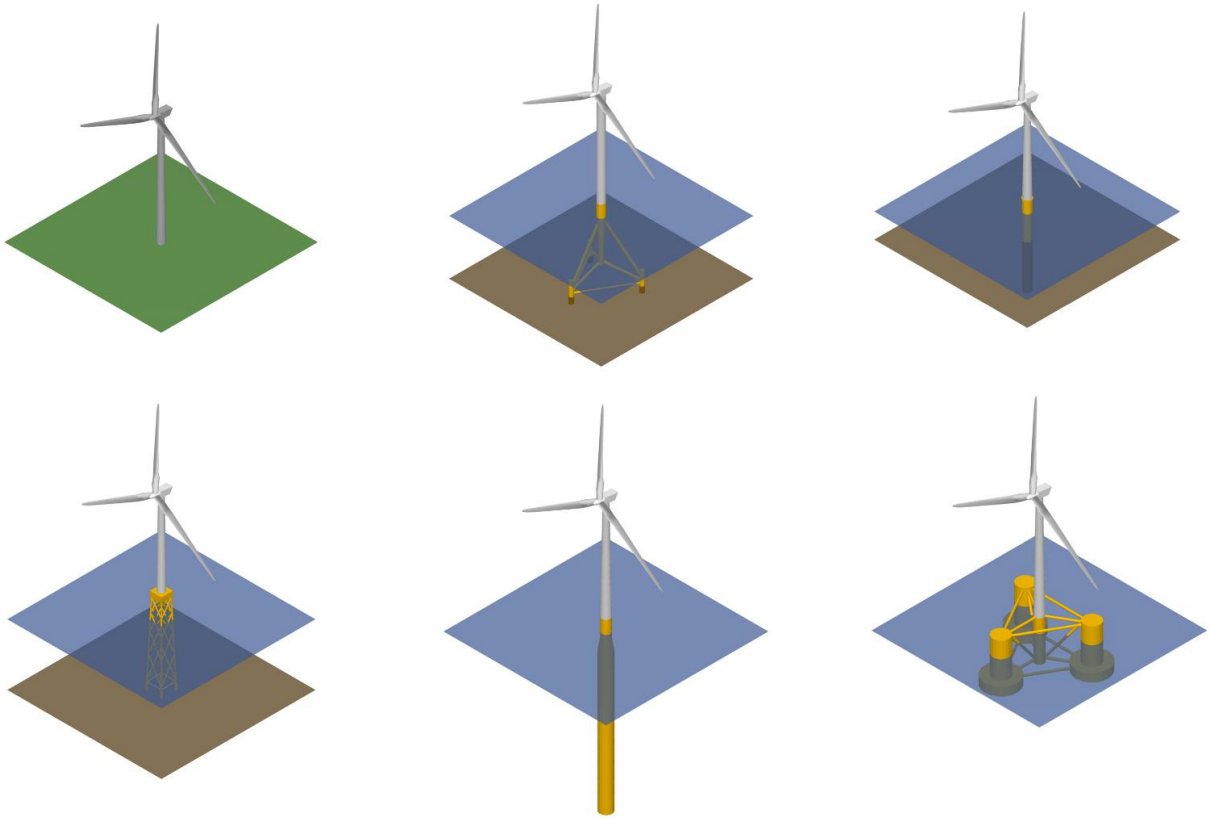

Figure 4: Visualisation of different wind turbine substructure types which can be modelled in QB.

The structural dynamics in QB are modelled in a true multi-body formulation. The sub components of the multi-body model are made up of rigid- or flexible nonlinear Euler beam elements in a corotational formulation. For floating offshore simulations, QB integrates cable elements in the absolute nodal coordinate formulation (ANCF) which meet the requirements to effectively model the nonlinear dynamics of complex mooring systems.

Both bottom-fixed and floating offshore wind turbine systems can be modeled in QB. The hydrodynamic loads on the wind turbine's substructure are calculated either via the potential flow theory, the Morison equation based strip theory or a user defined combination of the two. The integrated potential flow approach also includes the higher order slow drift forces obtained from quadratic transfer functions. QB integrates with potential flow data from common software such as the WAMIT, NEMOH or similar toolboxes. Figure 4 shows some exemplary turbine models which can be simulated in QB. In the following subsections, the extended functionality of QB required to perform hydroelastic offshore wind turbine simulations is presented.

3.1.1 References

[1] Marten, D. (2020). QBlade: a modern tool for the aeroelastic simulation of wind turbines. Doctoral Thesis. TU Berlin.

[2] Marten, D., Paschereit, C. O., Huang, X., Meinke, M. H., Schroeder, W., Mueller, J., Oberleithner, K. (2020). Predicting Wind Turbine Wake Breakdown Using a Free Vortex Wake Code. AIAA Journal, 58(11).

[3] Balduzzi, F., Marten, D., Bianchini, A., Drofelnik, J., Ferrari, L., Campobasso, M. S., Pechlivanoglou, G., Nayeri, C. N., Ferrara, G., Paschereit, C. O. (2017). Three-Dimensional Aerodynamic Analysis of a Darrieus Wind Turbine Blade Using Computational Fluid Dynamics and Lifting Line Theory. Journal of En-gineering for Gas Turbines and Power, 140(2), 022602.

[4] Madsen, H. A., Larsen, T. J., Pirrung, G. R., Li, A., Zahle, F. (2020) Implementation of the blade element momentum model on a polar grid and its aeroelastic load impact. Wind Energy Science. 5(1). 10.5194/wes-5-1-2020

3.2 STRUCTURAL MODEL

The structural model in QB is based on the FEA module of the open source multi-physics engine Project Chrono [1]. Project Chrono is based on a platform independent design [2], which is developed in the C++ language as an object-oriented library, consisting of various components, such as Chrono::Vehicle: a module for vehicle modeling and simulation, Chrono::MKL: an interface for sparse direct solvers or Chrono::FSI: a module for fluid-solid interaction problems. Chrono is used to model onshore blade and tower structures and its use in QB is extended for the modeling of offshore bottom-fixed or floating structures.

For the integration into QB the Chrono::Engine module is employed. Chrono::Engine is the core module of Project::Chrono, it contains functionality for setting up and solving physical systems containing

Newtonian dynamics and finite elements. The SparseLU solver of the EIGEN C++ template library [3] is used as a solver for the finite element problem. A dynamic link library, containing the Chrono module (version 6.0.0), has been compiled from Project Chrono's GIT repository. The relevant header files of Project Chrono and the EIGEN library are included, and the Chrono DLL is linked to the QB source code. This enables the definition of the physical system and the finite elements and grants access to the solver to perform time domain simulation of structural dynamics inside QB.

An offshore sub-structure in QB can either be defined by rigid elements, by Euler-Bernoulli beam elements in a co-rotational formulation [4], or as a mix of rigid and flexible elements. In the co-rotational formulation (see Figure 5), a floating coordinate system is attached to each deformable beam element. The overall motion of a beam element is then the addition of the rigid body motion undergone by the floating coordinate system and a strain deformation, expressed in the floating frame of reference.

For time domain simulations in QB the iterative HHT (Hilber-Hughes-Taylor formulation [5]) integrator is employed. QB employs a flexible loose-coupling approach between the aerodynamic, hydrodynamic and structural dynamics simulation. For a modal analysis the global tangent stiffness, damping and mass matrix of the full system is used to setup a generalised eigenvalue problem which is solved using the DGGEV function of the LAPACK [6] library. The exported tangent (linearised) matrices include terms for geometric stiffness.

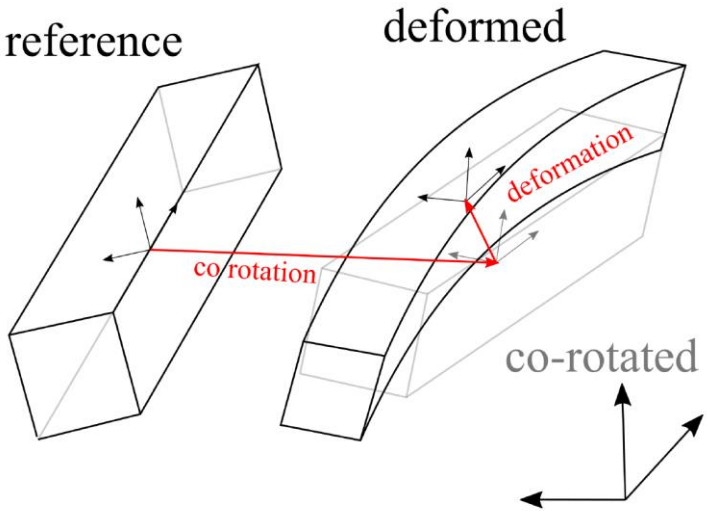

Figure 5: Visualisation of a co-rotational beam-element

Mooring lines are explicitly modeled as Absolute Nodal Coordinate Formulation (ANCF) cable elements that are connected to the substructure via relative positional constraints and to the seabed via fixed positional constraints. ANCF elements are treated similarly to Euler beam elements but do not transmit any torsional moments. Hydrodynamic forces for mooring lines are included via the Morison (strip-theory) equation (see Section 3.5.3). Cable elements can also be defined between flexible, or rigid, beam elements of the sub-structure.

The fixed or floating substructure is defined through a human readable ASCII based input-file format, based on keywords and data tables. Through the input file format it is possible to define arbitrary substructures with complex mooring systems. Substructures are constructed from a set of flexible or rigid beam and cable elements (members) (see Figure 6) which are defined between a set of nodes (or joints). For each element's hydrodynamic coefficients (axial, normal) may be assigned. Virtual sensors can be distributed along each member of a substructure to output the internal force and torque along the members and the reaction force and torque at member connections. Within a single bottom fixed or floating substructure definition multiple linear potential flow bodies may be defined (see Section 3.5) and constrained to members or rigid bodies of the substructure.

A detailed description of the substructure file format and the definitions of tables and keywords will be published in the QB online user's guide as an additional deliverable of WP1.

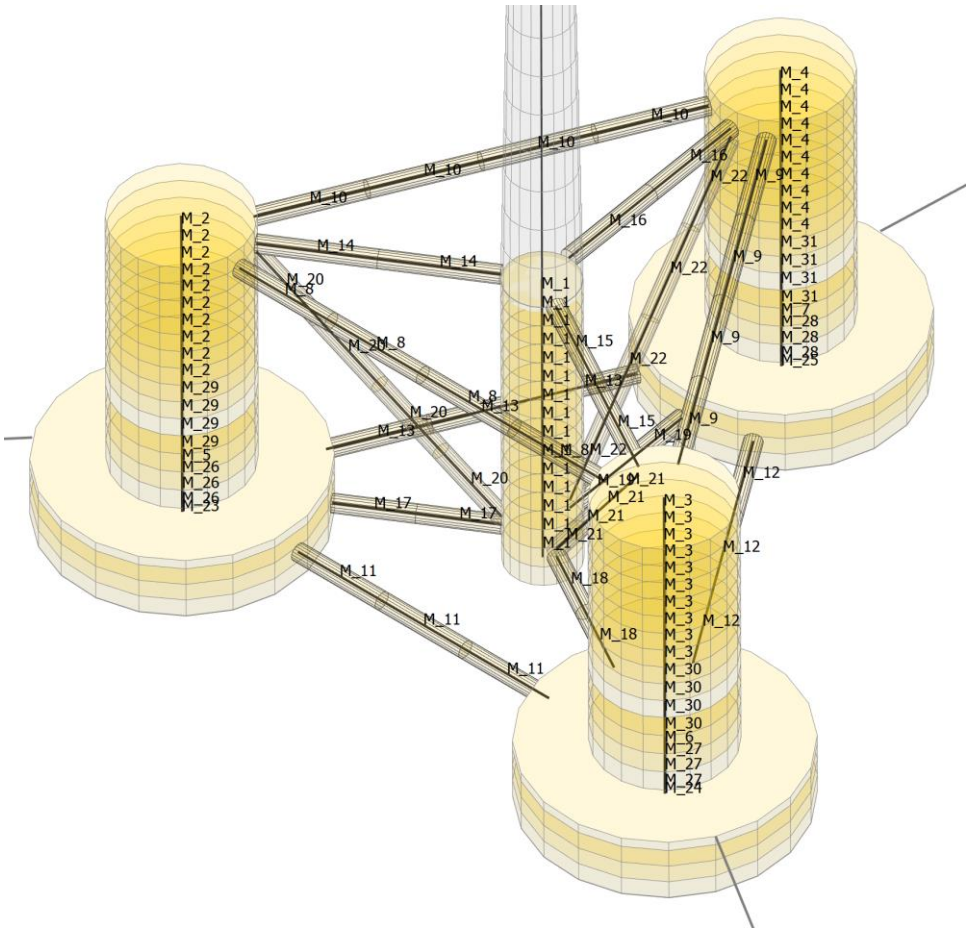

Figure 6: Visualisation of the members of a semisubmersible substructure.

3.2.1 References

[1] Tasora, A., Serban, R., Mazhar, H., Pazouki, A., Melanz, D., Fleischmann, J., Negrut, D., Chrono: An Open Source Multiphysics Dynamics Engine. High Performance Computing in Science and Engineering, 19–49. doi: 10.1007/978-3-319-40361-8_2, 2016.

[2] Projectchrono.org. Project Chrono - An Open-Source Physics Engine, 2019. URL https://projectchrono.org/about/

[3] Tuxfamily. EIGEN - a C++ template library for linear algebra: matrices, vectors, numerical solvers and related algorithms. URL http://eigen.tuxfamily.org.

[4] Negrut, D., Recuero, A., Co-rotational Formulation in Chrono, 2016. Whitepaper, pages 1–10, https://www.projectchrono.org/assets/white_papers/FEA/WhitePaper_Co-rotational.pdf.

[5] Tasora, A. Time Integration in CHRONO::Engine, 2018. Project::Chrono Technical Documentation, Universita di Parma, Parma, Italy.
http://www.projectchrono.org/assets/white_papers/ChronoCore/integrator.pdf

[6] Netlib.org. LAPACK—Linear Algebra Package. URL http://www.netlib.org/lapack/.

3.3 WAVE AND CURRENT MODELLING

In order to model important hydrodynamic effects within QB, the kinematics of the water particles have to be accurately taken into account. A range of wave and sea-current modelling options are available in QB. The theory underlying these approaches are described in the sections below along with important variables for the analysis.

3.3.1 Linear Wave Theory

Linear wave theory (also referred to as airy waves in the literature) may be applied when the sea water is assumed to be incompressible, inviscid and the fluid motion is irrotational and with very small wave steepness. In addition to this is it assumed that the wave steepness is very small. Subsequently, a velocity potential can be used to describe the velocity vector *(u,v,w)* of a water particle at an arbitrary position *(x,y,z)* at any time *t* [1]. Following these assumptions, the linear wave model in QB is implemented through the following set of equations. The velocity potential for finite depth may be expressed as

$$\Phi(\mathrm{x},\mathrm{y},\mathrm{z},\mathrm{t}) = -\frac{gA}{\omega}\frac{cosh\big(k(z+h)\big)}{cosh(kh)}cos(\omega t - kx) \qquad (1)$$

Where the wave number *k* can be expressed through the approximation of the dispersion relationship by,

$$k = \frac{\omega^2}{g}\left(1 - e^{-\left(\omega\sqrt{\frac{h}{g}}\right)^{\frac{5}{2}}}\right)^{-\frac{2}{5}} \qquad (2)$$

In the equation above, g is the gravitational acceleration, *(x,y,z) are* Cartesian coordinates, *A* is the wave amplitude, ω the angular frequency and h the water depth [2]. For infinite water depth the velocity potential may be expressed through:

$$\Phi(\mathrm{x},\mathrm{y},\mathrm{z},\mathrm{t}) = -\frac{gA}{\omega}e^{kz}cos(\omega t - kx) \qquad (3)$$

The wave elevation of a regular wave train at any position of the free surface at a given time *t* is given by

$$\zeta(x, y, t) = Asin(kX - \omega t) \quad (4)$$

Where *k* represents the wave number and *X* the ordinate in the direction of the wave heading angle Θ*:*

$$X = x\, cos(\Theta) + y\, sin(\Theta)\,. \quad (5)$$

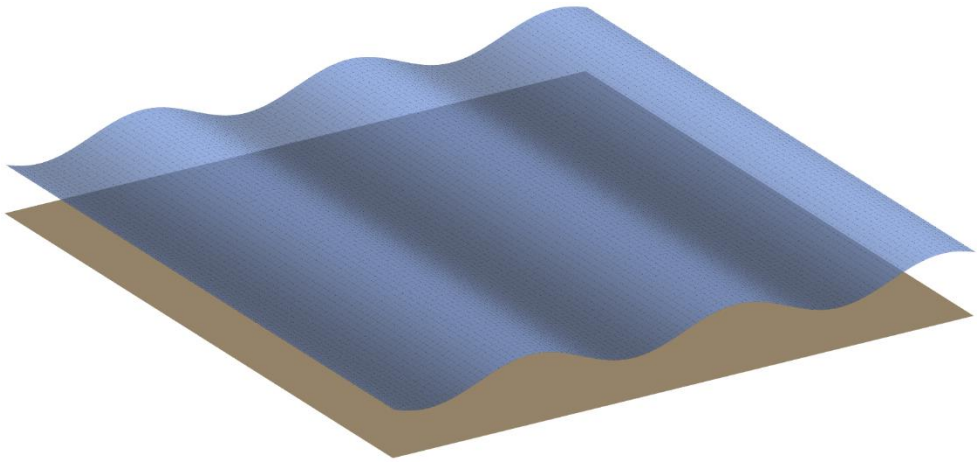

Figure 7: Exemplary regular wave created in QB

3.3.2 Irregular Linear Waves – Unidirectional

Irregular wave fields in QB belong to a short-term description of the sea, meaning that the significant wave height and the mean wave period are assumed to be constant over the considered time [1].
The irregular wave field is created through a linear superposition of *N* different linear waves trains. Each one of these wave trains is described by an amplitude A_j, an angular frequency ω_j and a phase ϵ_j $(0 - 2\pi)$. Hence, the wave elevation of an irregular wave field propagating along one direction (x-axis in this case) can be expressed through the following equation.

$$\zeta(x, y, t) = \sum_{j}^{N_j} A_j\, sin\left(k_j x - \omega_j t + \epsilon_j\right) \quad (6)$$

A_j is to be determined by discretizing a wave spectrum $S(\omega)$ into discrete bins corresponding to a frequency range $\Delta\omega$ [1].

$$\frac{1}{2} A_j^2 = S\left(\omega_j\right) \Delta\omega \quad (7)$$

Two of the most commonly used wave spectra are the Pierson-Moskowitz (PM), also known as ISSC-spectrum, and the JONSWAP (JS) spectrum. The former was originally proposed for fully developed sea

and the latter extends the PM-spectrum to include developing sea states [3]. The spectra are described by the following equations.

$$S_{PM} = \frac{5}{16}\left(\frac{f}{f_p}\right)^{-5} H_s^2 \; T_p \; e^{-\frac{5}{4}\left(\frac{f}{f_p}\right)^{-4}} \tag{8}$$

Where T_p is the peak period, f_p the peak frequency ($\frac{1}{T_p}$) and H_s the significant wave height.

$$S_{JS} = A_\gamma S_{PM}(\omega)\gamma^{e^{\left(-0.5\left(\frac{f-f_p}{\sigma f_p}\right)^2\right)}}. \tag{9}$$

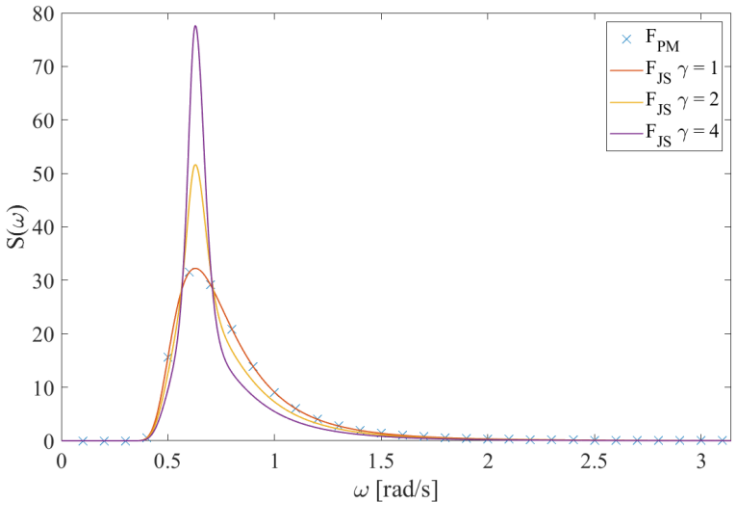

Figure 8: Pierson-Moskowitz and JONSWAP spectra with different peak shape parameters

As visible, the JONSWAP spectrum is a modification of the PM-spectrum by A_γ a normalizing factor, γ the peak shape parameter and σ the spectra width parameter [4].

3.3.3 Irregular Linear Waves - Multidirectional

A uni-directional wave spectrum $S(\omega)$ may be augmented through a directional function $D(\Theta)$ in order to create a multi-directional wave field,

$$S(\omega, \Theta) = S(\omega)D(\Theta)\,, \tag{10}$$

where Θ is the angle between the main wave direction and the direction of a singular wave train [1]. QB makes use of the directional spectrum defined in [5],

$$D(\Theta) = C(s)cos^s\left(\Theta - \Theta_p\right), \tag{11}$$

where $C(s)$ is a normalizing constant

$$C(s) = \frac{\Gamma\left(\frac{s}{2}+1\right)}{\sqrt{(\pi)}\Gamma\left(\frac{s}{2}+\frac{1}{2}\right)}. \tag{12}$$

Here, s is the spreading exponent and Θ_p is the principal wave direction. When the directional spectrum is added, Equation 6 then needs to be advanced by another summation term over the directions of the wave trains to calculate the wave elevation within a wave field.

$$\zeta(x,y,t) = \sum_{i}^{N_i}\sum_{j}^{N_j} A_{ij}\, sin\left(k_i X_j - \omega_i t + \epsilon_{ij}\right) \tag{13}$$

With X_j being defined as $X_j = xcos\left(\Theta_j\right) + ysin\left(\Theta_j\right)$. Subsequently. Equation 7 then becomes:

$$\frac{1}{2}A_{ij}^2 = S\left(\omega_i, \Theta_j\right)\,\Delta\omega\Delta\Theta \tag{14}$$

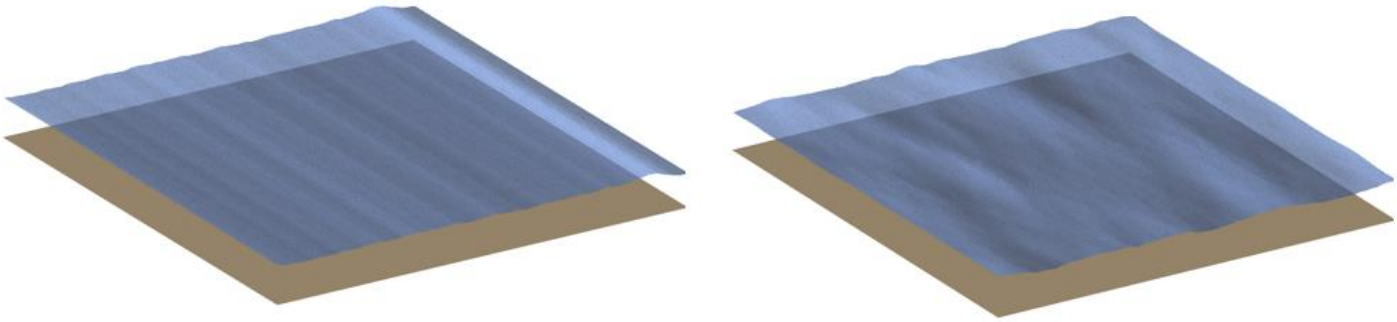

Figure 9: Irregular wave fields generated in QB. Uni-directional (left), multi-directional(right)

3.3.4 Wave Kinematics – Regular Wave

The velocity and acceleration profile over the water depth may be derived from the velocity potentials provided previously (Eq. 1 and 3). For simplicity, the distinction between uni- and multi-directional wave fields is neglected in this section. In the case of a uni-directional wave field the first summation term becomes redundant. In the case of infinite depth (for most waves of interest this represents a depth greater than 100m), the velocity profiles are given by:

$$\mathrm{V_x}(x,y,z,t) = \sum_{i}^{N_i}\sum_{j}^{N_j} A_{ij}\omega_\mathrm{i} cos\left(\Theta_\mathrm{j}\right)E_c(z)sin\left(k_i X_j - \omega_\mathrm{i} t + \varepsilon_{ij}\right) \tag{15}$$

$$V_y(x,y,z,t) = \sum_{i}^{N_i}\sum_{j}^{N_j} A_{ij}\omega_\mathrm{i} sin\left(\Theta_\mathrm{j}\right)E_c(z)sin\left(k_i X_j - \omega_\mathrm{i} t + \varepsilon_{ij}\right) \tag{16}$$

$$V_z(x,y,z,t) = \sum_{i}^{N_i}\sum_{j}^{N_j} -A_{ij}\omega_\mathrm{i} E_s(z)cos\left(k_i X_j - \omega_\mathrm{i} t + \varepsilon_{ij}\right) \tag{17}$$

hence, the acceleration may be derived:

$$a_x(x,y,z,t) = \sum_i^{N_i} \sum_j^{N_j} -A_{ij}\omega_i^2 cos(\Theta_j) E_c(z) cos(k_i X_j - \omega_i t + \varepsilon_{ij}) \quad (18)$$

$$a_y(x,y,z,t) = \sum_i^{N_i} \sum_j^{N_j} -A_{ij}\omega_i^2 sin(\Theta_j) E_c(z) cos(k_i X_j - \omega_i t + \varepsilon_{ij}) \quad (19)$$

$$a_z(x,y,z,t) = \sum_i^{N_i} \sum_j^{N_j} -A_{ij}\omega_i^2 E_s(z) sin(k_i X_j - \omega_i t + \varepsilon_{ij}) \quad (20)$$

Where $E_c(z) = \frac{cosh(k_i(z+h))}{sinh(k_i h)}$ and $E_s(z) = \frac{sinh(k_i(z+h))}{sinh(k_i h)}$ are depth scaling factors. In cases where the influence of depth is negligible, the depth scaling factor becomes $E(z) = e^{(k_i z)}$.

3.3.5 Constant Sea Currents

Within QB three different types of time constant currents may be defined. An overview of the available types of currents is given below.

- Near Surface Currents (constant shear profile): Definition of velocity, direction and depth
- Sub Surface Currents (power law profile): Definition of Velocity, direction and shear exponent
- Near Shore Currents (constant): Definition of Velocity and direction

Any combination of these types of currents and/or waves may be included within a QB simulation. In all cases the velocities at each evaluation point are evaluated as a superposition of all contributions from waves and currents.

A complete hydroelastic representation of the turbine also requires accounting for fluid-structure interaction. This topic is covered in the next two sections.

3.3.6 Kinematic Wave Stretching

Linear wave theory only provides information about the water kinematics at and below mean sea level (MSL). If the velocity or acceleration within points above MSL is of interest (i.e. in a wave crest), extrapolation or stretching methods become necessary [3].

In the literature, several wave stretching methods have been introduced [3, 6, 7]. Their general approach is to model the depth scaling factors E (see Equations (15)-(20) for points above MSL ($z > 0$) by stretching or extrapolating their values to the values at the modified depth. In the following, the three methods that have been implemented into QB are introduced briefly. For further information the reader is referred to [3, 6, 7].

1. Vertical stretching: This method assumes that all points above MSL equal the kinematic conditions at MSL ($E(z)$ = 0). E below MSL is left unchanged

2. Extrapolation stretching: This method extrapolates $E(z)$ above MSL linearly by using its gradient along the z-axis. Again, $E(z)$ below MSL is left unchanged.

3. Wheeler stretching: This method modifies $E(z)$ so it always is stretched (or contracted) to the instantaneous wave elevation ($z = H$). This is done by replacing z with a scaling factor z' which modifies z linearly so that the following statement is always valid $h < z' < 0$, where h Is the water depth.

QB also provides the option to deactivate wave stretching. In this case, the velocity above MSL will always be equal to zero.

3.3.7 References

[1] Faltinsen, O. M., Sea Loads on Ships and Offshore Structures, Cambridge University Press, 1990

[2] Guo, J., Simple and explicit solution of wave dispersion equation, Coastal Engineering, Volume 2, Issue 2, pp. 74-77, 2002

[3] DNV-RP-C205, Environmental Conditions and Environmental Loads, Recommended Practice, Det Norske Veritas AS.

[4] Branlard, E., Generation of time series from a spectrum, Technical Report, Risø DTU, National Laboratory for Sustainable Energy, 2010

[5] OrcaFlex, www.orcina.com, Directional Spread Spectrum,

https://www.orcina.com/webhelp/OrcaFlex/Content/html/Wavetheory.htm#WaveSpreadingTheory

[6] OrcaFlex, www.orcina.com, Waves: Kinematic Stretching,
https://www.orcina.com/webhelp/OrcaFlex/Content/html/Waves,Kinematicstretching.htm

[7] FRyDoM, v3.5, Kinematic stretching,
http://theory.frydom.org/src/environment/waves/linear_wave_theory/wave_stretching.html

3.4 HYDROSTATIC MODELS

There are three possibilities to treat buoyancy in QB. These are independent of the choice of hydrodynamic modelling and can be mixed depending on the type of analysis desired. These are described in the sections below.

Constant hydrostatic force: It is common to treat the buoyancy force and being the sum of a constant hydrostatic force (that of the submerged floater in equilibrium position) plus a linear restoring force (the hydrostatic stiffness matrix), which represents hydrostatic restoring forces [1]. This is applied at the user-defined reference position.

Hydrostatic stiffness matrix: In order to apply restoring forces in the case that the floater deflects away from the equilibrium position a hydrostatic stiffness matrix can be specified. This matrix models a linear

relationship between deflection and restoring forces and is hence a simplification of the true nonlinear buoyancy forces acting. For cases of moderate wave states and small deflections however this approximation can be perfectly sufficient. These matrices generally are amongst the output of a potential flow solver as described in the previous section.

Explicit Buoyancy: This option uses a localised approach to calculate the buoyancy forces. The local substructure element is discretised axially and azimuthally into angular segments. The buoyancy force applied is based on the submerged volume. This option is more representative in cases where the wavelength of the incoming wave field is smaller than the planform of the floater, hence exposing different floater regions to crests/troughs of waves.

3.4.1 References

[1] Jonkman, J. Definition of the Floating System for Phase IV of the OC3 Project. National Renewable Energy Laboratory. Technical Report NREL-TP-500-47535, May 2010.

3.5 HYDRODYNAMICS MODELS

Accounting for hydrodynamic forces resulting from motion of the floater and incoming waves is critical for accurate simulation of offshore wind turbines. Two approaches to the calculation of hydrodynamic loads on the floater are available in QB.

- Linear potential flow method with Morrison drag (LPMD)
- Full Morrison equation method. (ME)

These are summarised in Table 1.

Method:	**LPMD**	**ME**
Structural treatment	Point load at transition piece	Distributed loads
Inertial treatment	Point mass at floater COG	Distributed masses
Added mass forces	[6x6] Added mass matrix from potential flow solver.	Strip theory: cylindrical sections C_a coefficient
Drag forces	Strip theory: Distributed cylindrical sections C_d coefficient	
Radiation damping	[6x6] Radiation damping IRF	-
Wave forces	[6x6] Excitation force IRF	Strip theory: Distributed cylindrical sections C_p coefficient

Table 1: Hydrodynamic model options in QB.

Features of both can be mixed, depending upon user input and desired modelling approach. These are described individually in the following sections.

3.5.1 Linear Potential Flow with Morrison Drag:

The first method makes use of a potential flow model to treat the hydrodynamic forces acting on the substructure. This is calculated based on the Cummins equation [1]:

$$\left(M_{ij} + A_{ij}^{\infty}\right)\ddot{x}_j(t) + \int_{-\infty}^{t} K_{ij}(t-\tau)\dot{x}_j(\tau)\, d\tau + C_{ij}x_j(t) = F_j^w(t) \qquad (21)$$

In this equation:

M_{ij} represents the inertia of the floater,

A_{ij}^{∞} is the added mass matrix (see below),

K_{ij} is the radiation damping matrix (see below),

C_{ij} is the hydrostatic stiffness matrix,

F_j^w are the forces due to waves,

Each of these terms shall be described in the following subsections.

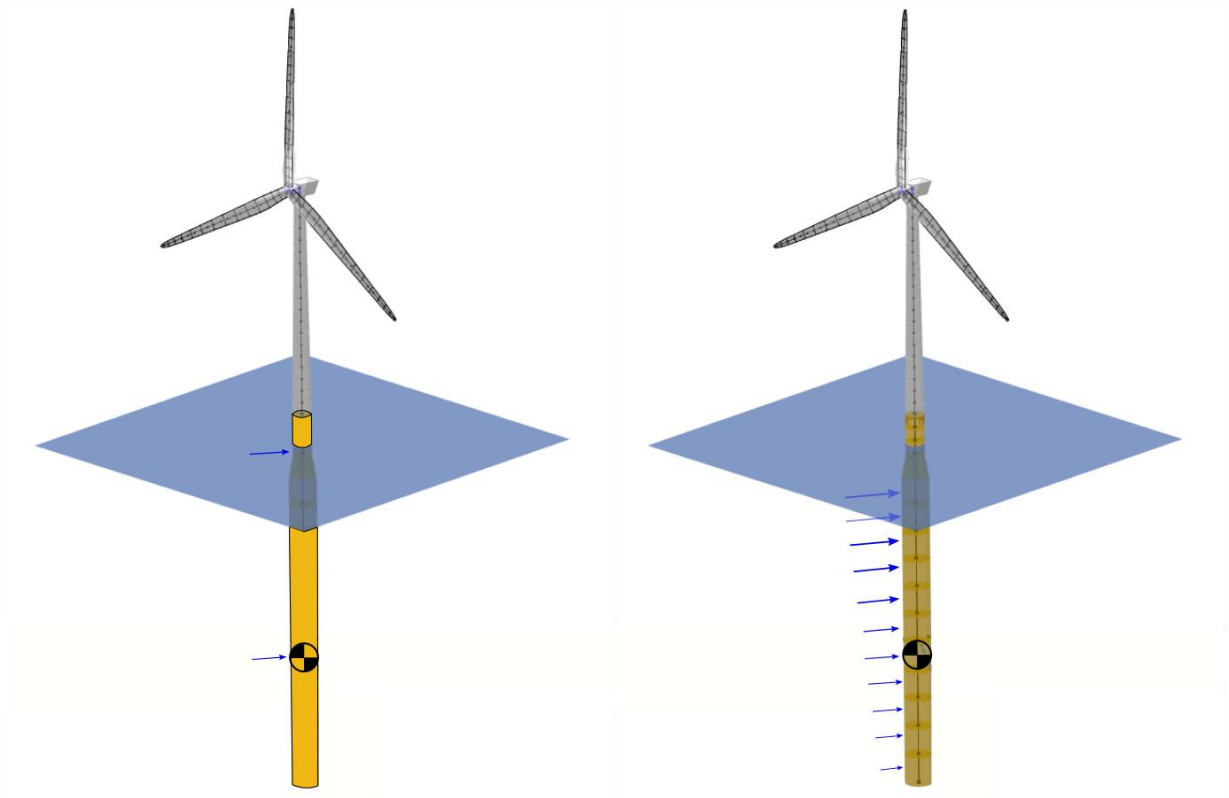

Figure 10. Left: LPMD model. Loads applied at the substructure COG and reference point. Right: ME model: Distributed loading applied at structural members.

Structural treatment: Within the LPMD treatment the substructure is treated as a rigid body. Specification of floater structural member coefficients are therefore unnecessary. This is illustrated in Figure 10.

Inertial treatment: The floater is treated as a point mass with inertial properties specified by the [6x6] inertial matrix M_{ij}. The inertial loads are applied at the centre of gravity of the floater. The inertial loads are calculated as $M_{ij}\ddot{x}_j$ where $\ddot{x}_j$ is the acceleration of the centre of gravity.

Added mass forces: The added mass matrix A_{ij}^{∞} can be specified from the outputs of a potential flow solver (such as NEMOH). The force is calculated as $A_{ij}^{\infty}\ddot{x}_j$ and is applied at the reference point specified by the user.

Drag forces: The main forms of hydrodynamic drag affecting a submerged body, the pressure drag and skin friction drag, are not accounted for within potential flow theory. These however generate significant loads which act on the substructure and for any realistic conditions should not be neglected. For this reason the drag coefficient is taken into account by considering the geometry to be composed of cylindrical sections, each having a normal and axial drag coefficient $C_{d,n}$ and $C_{d,a}$. The loading is applied in the same fashion as for the ME drag calculations described below.

Radiation damping: The motion of the substructure gives rise to waves, which dissipate energy from the motion. This manifests in the form of radiation damping on the substructure. These coefficients can be calculated in the frequency domain with a potential flow solver. This can be imported in NEMOH [2] or WAMIT [3] formats. In order to calculate the time-domain forces, an impulse response function (IRF) K_{ij} is calculated based on the specified frequency domain values. This can be calculated as [4]:

$$K_{ij}(t) = \frac{2}{\pi}\int_0^{\infty} \omega R_{ij}(\omega)\sin\omega t\, d\omega = \frac{2}{\pi}\int_0^{\infty} B_{ij}(\omega)\cos\omega t\, d\omega\,, \qquad (22)$$

where R_{ij} and B_{ij} are the added mass and damping coefficients tabulated in the input file.

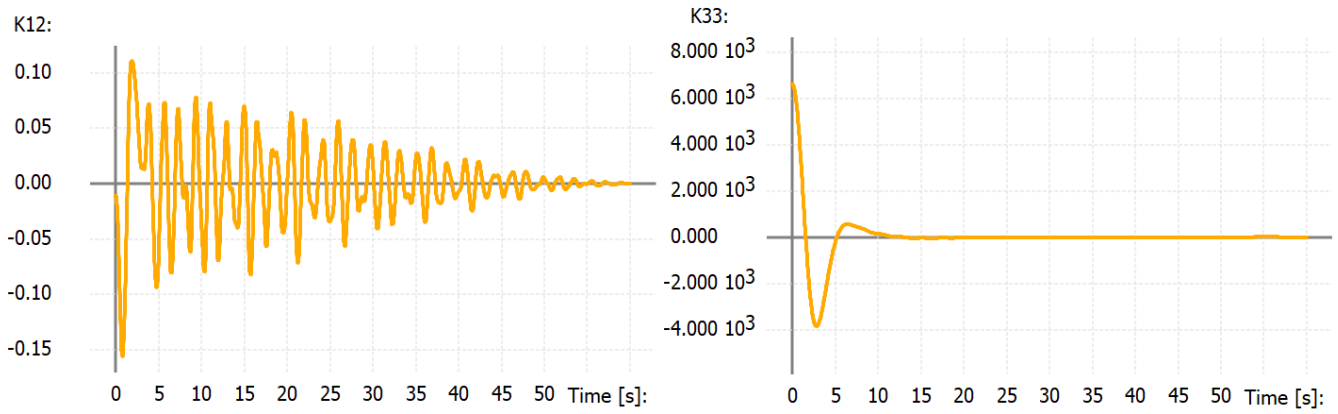

Figure 11: Radiation Damping IRF for a spar-buoy platform calculated within QB.

QB uses the second formulation due to its better numerical behavior. This integration is carried out numerically using the trapezoidal rule with a user-specified step. The calculated IRF can be viewed within the Turbine creation module by selecting Graph Mode: Radiation IRF Graph. An example of these is shown

in Figure 11. The IRFs are calculated during turbine specification and are used during time-marching simulations to determine instantaneous loading due to an impulse motion of the floater. The total forcing is calculated with the time convolution integral [4]:

$$\int_{t-T}^{t} K_{ij}(t-\tau)\dot{x}_j(\tau)\, d\tau \approx \sum_{i=1}^{i=T/\Delta_t} \Delta_t K_{ij}(i\Delta_t)\dot{x}_j(t-T+i\Delta_t)\,, \tag{23}$$

This is integrated numerically within QB using trapezoidal integration with the simulation time step size. As can be seen in Figure 11, the IRF becomes negligibly small after a given period of time. The integral above hence need not be carried out for all previous motions of the substructure, and a user-specified cut-off time can be used to truncate the convolution.

Wave Forces: By applying potential flow theory, the excitation force caused by an incoming wave can be calculated with the use of a time convolution in a similar manner to the radiation damping. This requires the calculation of the appropriate IRF for the excitation forces X_j [4]:

$$E_{ij}(t) = \frac{1}{2\pi}\int_{-\infty}^{\infty} X_j(\omega)e^{i\omega t}\, d\omega\,. \tag{24}$$

This is imported from a file as with the radiation damping. The numerical integration of this is carried out with the trapezoidal rule with a user-specified step size. This can again be viewed in the Turbine creation module by selection Graph Mode: Diffraction IRF Graph. An example of this is shown in Figure 12.

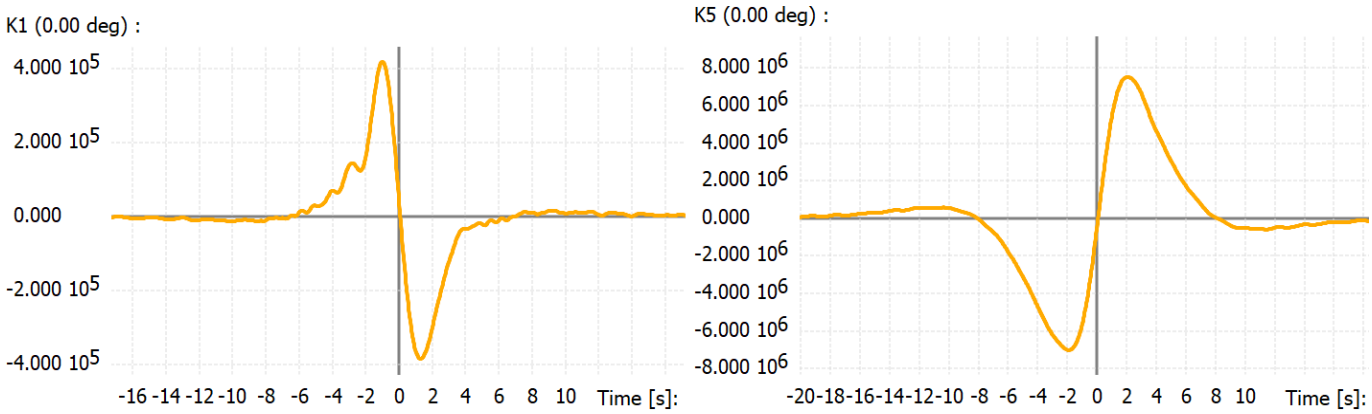

Figure 12: Excitation force IRF for a spar-buoy platform calculated within QB.

Analogously to the radiation damping forces, the integration of these are truncated in practical application. Unlike the radiation forces, the wave excitation forces acting on a body depend upon in the incoming angle of the wave train. For this reason, excitation forces are binned into user-specified angular segments, and these are superposed based on the heading of each wave train.

Modelling considerations: It is important to stress that underlying the use of this model is the assumption that the substructure has undergone small deflections and rotations from the equilibrium position. This

assumption becomes invalid for large motions or for cases where the instantaneous wave height is significant.

QB also allows modelling of the substructure with several potential flow bodies. This feature, in combination with the full Morison equation described below, enables the accurate hydroelastic modelling of complex substructure geometries. Large, stiff substructure parts can be modelled with a LPMD approach while slender, flexible parts can be modelled with a ME approach.

3.5.2 Second order hydrodynamics loads

Floating wind turbine structures are designed so their resonant frequencies lie outside the excitation spectrum of the first order wave excitation loads. Outside of linear theory, second order wave loads may nevertheless be the cause of resonance issues of floating structures and must therefore be accounted for in QB.

Second order loads scale proportionally to the square of the wave amplitude and excite at frequencies that are defined by the sum- and difference frequency of a wave pair. Loads caused by the frequency difference of two wave trains (in the following referred to as difference-frequency loads) excite at lower frequencies than are present in the wave spectrum. The opposite is true for loads caused by the frequency sum of a pair of wave trains (sum-frequency loads) [5]. Difference-frequency loads are mostly relevant for semi-submersible platforms and sum frequency loads for tension-leg platforms (problem often referred to as ringing) [6].

Similarly to the first-order excitation and radiation loads, second order loads are calculated in the frequency domain by potential flow codes like NEMOH [2] or WAMIT [3]. As an output, those codes provide the sum- and difference-loads in so called Quadratic Transfer Functions (QTF's) [6]. QB is fully capable of interpreting the QTF's generated by WAMIT and will be coupled to NEMOH as soon as this capability is implemented into the code.

In order to include the second order loads in QB, they first have to be transferred to the time domain. As this transfer makes use of a computationally expensive double summation, different approximations were investigated in the past [7, 8, 9]. In the following, the time domain conversion of the full QTF and the approximations relevant for the QB implementation are described.

Time Domain Conversion

The second-order excitation loads are computed similarly to the first order excitation-loads (Section 3.5.1) where the contribution of all wave trains with a given frequency and amplitude is added up and transferred to the time-domain via an inverse Fourier transform. In this case, a summation of the contribution from a wave pair is summed up and transferred into the time domain by applying double inverse Fourier transform [5, 6, 10].

$$F_{ex2}^{+} = \mathrm{Re}\left(\sum_{i}^{N_i}\sum_{j}^{N_j} A_i A_j Q_{ij}^{+}(\omega_i, \omega_j)\ e^{i[(\omega_i+\omega_j)t+(\epsilon_i+\epsilon_j)]}\right) \quad (25)$$

$$F_{ex2}^{-} = Re\left(\sum_{i}^{N_i}\sum_{j}^{N_j} A_i A_j\ Q_{ij}^{-}(\omega_i, \omega_j) e^{i[(\omega_i-\omega_j)t+(\epsilon_i-\epsilon_j)]}\right) \quad (26)$$

In Equations 25 and 26 A_* represents the wave amplitude, ω_* the frequency, ϵ_* the phase angles, t the time and Q_{ij} the sum- and difference-frequency QTF respectively. In the case of the difference-frequency loads. $^*Q_{ij}$ represents the complex conjugate.

Interpolation

Since the QTFs are computed within a pre-processing step outside of QB, an interpolation of the QTF onto the relevant frequencies that are present in the generated wave field is usually necessary. This is done within QB by applying a 2D interpolation algorithm that takes the original QTF and all frequencies from the wave field as an input. If the wave field contains a wave train with a frequency that lies outside the frequency range of the precomputed QTF, it is neglected from the second-order load calculation. An illustration of this interpolation is shown in Figure 13.

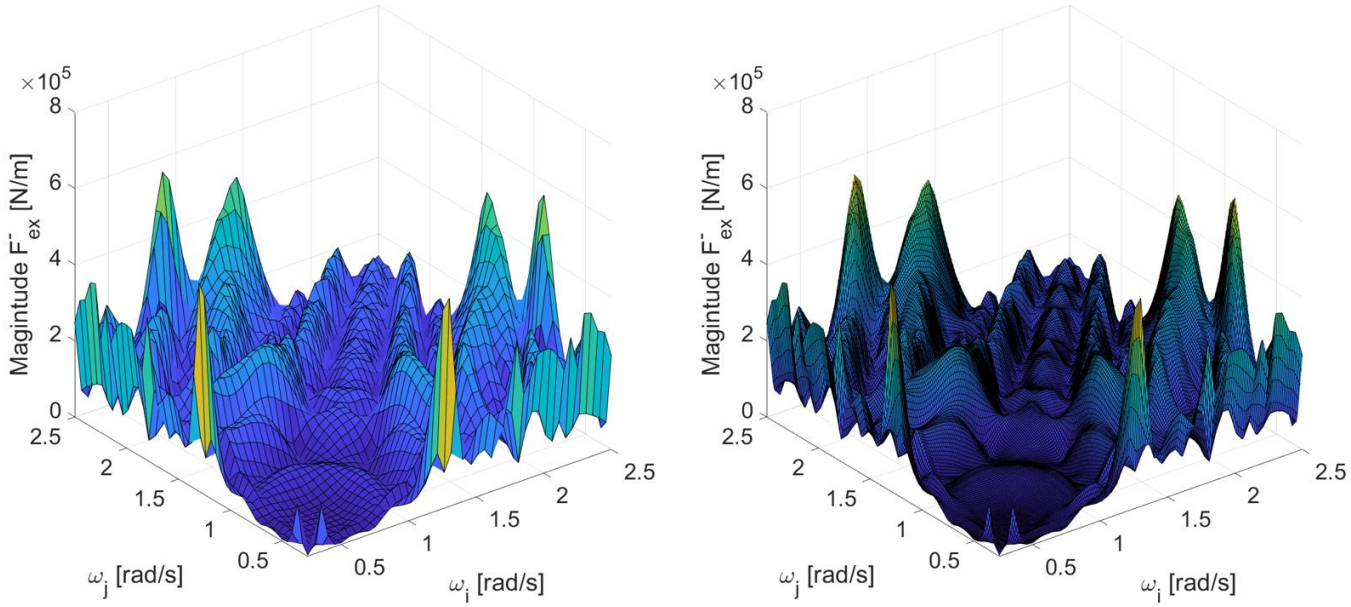

Figure 13: Difference-frequency QTF in surge corresponding to the OC4 platform. QTF as computed in potential flow code (left) and interpolated in QB onto a wave field composed of 250 wave trains (right).

Approximations

As detailed above, the computation of sum- and difference-frequency loads is relatively costly from a computational point of view. This is due to the double summation term in Equations 25 and 26 which creates an N^2problem due to its quadratic scaling with an increasing number of wave trains.

To mitigate this problem, the difference frequency loads may be approximated through the Newman's Approximation, developed by Newman himself in 1974 [7]. According to Newman, the off-diagonal terms

of the difference-frequency QTF may be approximated through the mean second order force (main diagonal of the QTF). This approach is advantageous in two ways: firstly, only the main diagonal terms of the QTF need to be known and secondly, the difference-frequency loads (also referred to as slowly varying second order forces) may be computed using only a single summation term [7].

$$F^{+}_{Newman} = Re\left(\sum_i^{N_i} A_i \sqrt{Q^{-}_{ij}(\omega_i,\omega_i)}\, e^{i(\omega_i t+\epsilon_i)}\Big|_{Q^{-}_{ij}(\omega_i,\omega_i)>0}\right) - Re\left(\sum_i^{N_i} A_i \sqrt{-Q^{-}_{ij}(\omega_i,\omega_i)}\, e^{i(\omega_i t+\epsilon_i)}\Big|_{Q^{-}_{ij}(\omega_i,\omega_i)<0}\right) \quad (27)$$

In this formulation, unphysically high frequencies (see Figure 14) are brought into the solution which need to be filtered out accordingly.

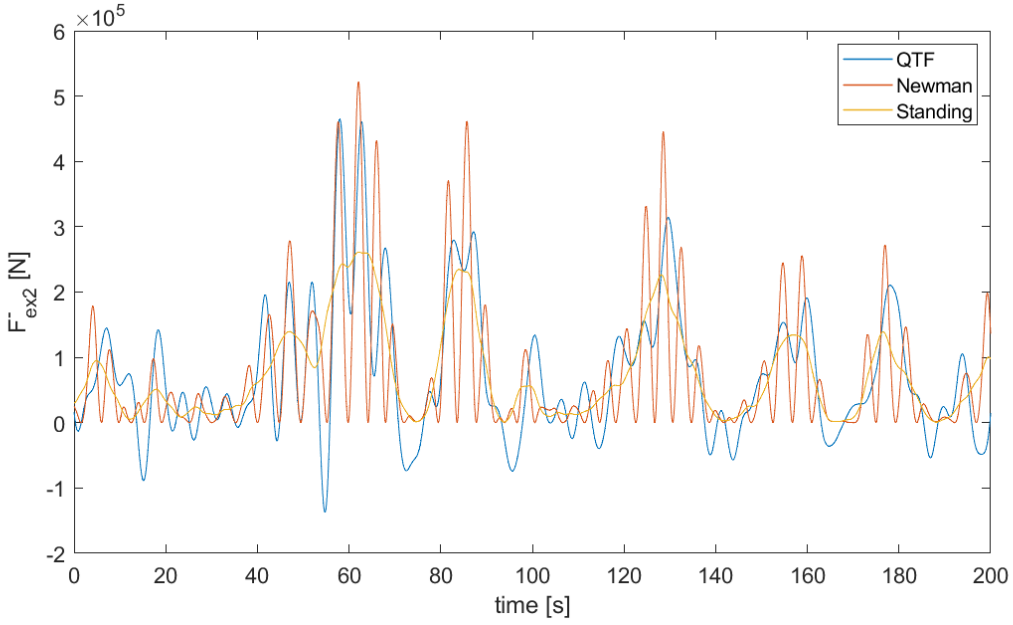

Figure 14: Time series comparing full QTF, the Newman and the Standing methods for the slowly varying second order forces in heave direction.

As this either makes an adaptive low-pass filter or an additional input by the user necessary. An improved formulation by Standing et. al. [11] which makes the need of filtering redundant, is implemented into QB. Standing's approximation has been implemented according to the formulation provided in [10].

$$F^{+}_{St} = Re\left(\left[\sum_i^{N_i} |A_i| sgn\left(Q^{-}_{ij}(\omega_i,\omega_i)\right)\sqrt{Q^{-}_{ij}(\omega_i,\omega_i)}\, e^{i(\omega_i t+\epsilon_i)}\right] x \left[\sum_i^{N_i} |A_i| \sqrt{Q^{-}_{ij}(\omega_i,\omega_i)}\, e^{-i(\omega_i t+\epsilon_i)}\right]\right) \quad (28)$$

3.5.3 Full Morison Equation Model (ME)

The second approach treats the substructure as a set of hydrodynamically independent bodies. This has the advantage that distributed loads can be applied to the substructure and the floater can be treated as being flexible, allowing for the treatment of hydroelastics. Strip theory is applied to each element in order to calculate hydrodynamic loads. This is illustrated in Figure 10. This method follows the approach laid out by Morison [12]. The loads are applied in both normal and axial direction, with the force vector automatically applied in the correct frame based on geometry orientation.

The normal loads on each element are given by [4]:

$$F_M^n = \rho\pi\left(\frac{D}{2}+R_{MG}\right)^2 L\left(\left(C_a^n+C_p^n\right)\dot{u^n}-C_a^n\ddot{X^n}\right)+\frac{1}{2}\rho(D+R_{MG})LC_d^n\left(u^n-\dot{X^n}\right)\left|u^n-\dot{X^n}\right| \tag{29}$$

The axial loads are given by:

$$F_M^{ax} = \rho\frac{2\pi}{3}\left(\frac{D}{2}+R_{MG}\right)^3 C_a^{ax}\left(\dot{u^{ax}}-\ddot{X^{ax}}\right)+C_p^{ax}p_{dyn}^{ax}\pi\left(\frac{D}{2}+R_{MG}\right)^2 + \frac{1}{2}\rho\pi(D+R_{MG})^2C_d^{ax}\left(u^{ax}-\dot{X^{ax}}\right)\left|u^{ax}-\dot{X^{ax}}\right|. \tag{30}$$

In these equations:

F_M^* represents the Morison force,

ρ represents the water density,

D and L are the diameter and length of the cylinder elements, respectively,

R_{MG} is the marine growth thickness,

C_a^* is the added mass coefficient,

C_d^* is the drag coefficient,

C_p^* is the dynamic pressure coefficient,

C_p^* is the dynamic pressure coefficient,

u^* is the flow velocity in the direction of interest,

$\dot{X}^*$ is the translational velocity of the geometric centre of the cylinder

The individual loading contributions are described in the following.

Structural treatment: The structural elements are defined within the substructure file. This is achieved by defining a set of structural nodes. Structural members are then defined between these nodes with appropriate structural coefficients. These structural members can be further discretised axially to improve fidelity. The Morison equations above are used to apply a normal and axial load at the centre and ends of

each structural element, respectively. By applying distributed gravity, hydrostatic and hydrodynamic loads to these points, the motion is integrated with the structural solver of Chrono.

Inertial treatment: Based on the structural discretization applied as described above, each submerged structural element has interpolated mass and stiffness properties. These are integrated for each element and are specified as beam element properties. Inertial forces are hence handled within Chrono.

Hydrodynamic coefficients: In addition to the structural nodes and members array, the hydrodynamic coefficients which appear in the Morison equations are also specified for submerged members. Axial hydrodynamic coefficients C_*^{ax} are assigned at mating sections. These play a large role where diameter changes occur. Equivalently, normal hydrodynamic coefficients C_*^n are assigned for cylindrical sections. This allows maximum user freedom by allowing the specification of an arbitrary number of coefficients for different sections. Care should be taken to ensure that the hydrodynamic coefficients correspond to the cross-sectional geometry.

Added mass forces: Axial added mass coefficients are specified for each submerged member. These influence axial forces which occur in the direction of the axis of a cylindrical section where column diameter changes occur, such as the bottom face or tapering sections of a spar buoy. Normal added mass coefficients are also specified and influence added mass forces acting normal to a cylindrical section due to motion of the body or changing relative velocity field.

Drag forces: Axial and normal drag coefficients are also specified in order for calculation of viscous drag forces.

Radiation damping: This is not accounted for in the use of the ME model. It is seen from the equation above that this is proportional to the velocity of the substructure, and hence under suitable circumstances may be considered to be negligible. Alternatively, the user can apply this portion of the LPMD model.

Wave forces: The varying pressure distribution over the surface of the floater is accounted for by calculating Froude-Krylov forces [4]. For low frequency wave fields this is well approximated with the C_p^{ax} and C_p^n coefficients.

Mooring line forces: A crucial part of the correct simulation of floating offshore wind turbines is the dynamic reaction of the mooring system. This is shown for a Spar-Buoy platform in Figure 16. The mooring system can be easily modelled in QB by specifying mooring line elements. This requires specification of the attachment point on the fairlead and the ground position (with x,y,z coordinates) and mass and tensile parameters. The mooring line segments are treated as cable segments in Chrono (see Section 3.2). The mooring lines furthermore are treated as hydrodynamic bodies (ME approach). As such, added mass and drag forces coefficients are required. A second option is available to avoid the generation of discretised mooring line elements and for testing purposes. The user can treat the mooring lines reactions as a linearised restoring force.

MacCamy-Fuchs Correction: For cylindrical elements that have a diameter to wavelength ratio larger than 0.2, the diffraction forces become relevant and the pure Morison equation is no longer accurate [4]. The diffraction effects can be accounted for with the ME formulation by introducing the MacCamy-Fuchs Correction (MCFC). The original MCFC is formulated in terms of the normal force per unit length on the cylinder. It can be recast so that the inertia part of the Morison equation is affected [13]. Following an approach presented in [14], QB changes the local water particle acceleration's magnitude and phase that affect the Morison element. The original modifications include the calculation of Bessel functions. To speed up calculations, an approximation based on easier functions proposed in [14] is used for the modification of the particle acceleration's magnitude and phase. The equivalent particle acceleration amplitude is given by:

$$\dot{u}_{eq} = \dot{u} \cdot \min\left(\frac{1.05 \tanh\left(2\pi \frac{d}{\lambda}\right)}{\left(\mathrm{abs}\left(\pi \frac{D}{\lambda} - 0.2\right)^{2.2} + 1\right)^{0.85}}, 1 \right). \tag{31}$$

In this equation, $\dot{u}$ is the water particle acceleration amplitude, d is the water depth, D is the diameter of the element and λ is the wavelength.

The phase shift of the acceleration is given by:

$$\alpha^{\mathrm{phase}} = \frac{\pi}{180}\left(-\frac{450}{8}\left(\pi \frac{D}{\lambda} - 2\right) - \frac{75}{\left(\pi \frac{D}{\lambda} + 0.5\right)^2} \right). \tag{32}$$

Since it affects the incoming water particle acceleration and phase, this implementation of the MCFC can be easily extended to irregular wave spectra. In this case, the correction is done on each wave train that makes up the wave spectrum and avoids using frequency dependent added mass coefficients in the ME formulation.

Modelling considerations: In QB, each cylindrical element can be divided into sub-elements to each of which the Morison forces are evaluated and applied at each time step. Setting the hydrodynamic coefficients to 0 effectively disables their contribution in the calculation of the Morison forces. This way, it possible to include for example the hydrodynamic drag only. To determine if a sub-element is partially or fully submerged, the wave elevation is required. Wave kinematics are also required in order to calculate element relative velocity and acceleration in the equations above. There are three possibilities in QB to do this. These options are presented in Figure 15.

The first option shown in Figure 15 a) is the wave kinematics and elevation in the local instantaneous position of the cylinder. In this example, the cylinder has been divided into four sub-elements. The lower two are fully submerged and one sub-element is partially submerged. The second option in Figure 15 b)

is using the wave elevation and kinematics at the initial position of the sub-element. This option allows a coherent theoretical assumption of small oscillations around a steady position when Morison forces are used in conjunction with a linear potential flow model. The third option is using the wave elevation and kinematics at a low-passed position of the sub-element (Figure 15 (c)). This allows for an assumption of small oscillations around a steady state for an element that as drifted from its initial position due to e.g. an aerodynamic thrust or sea current forces.

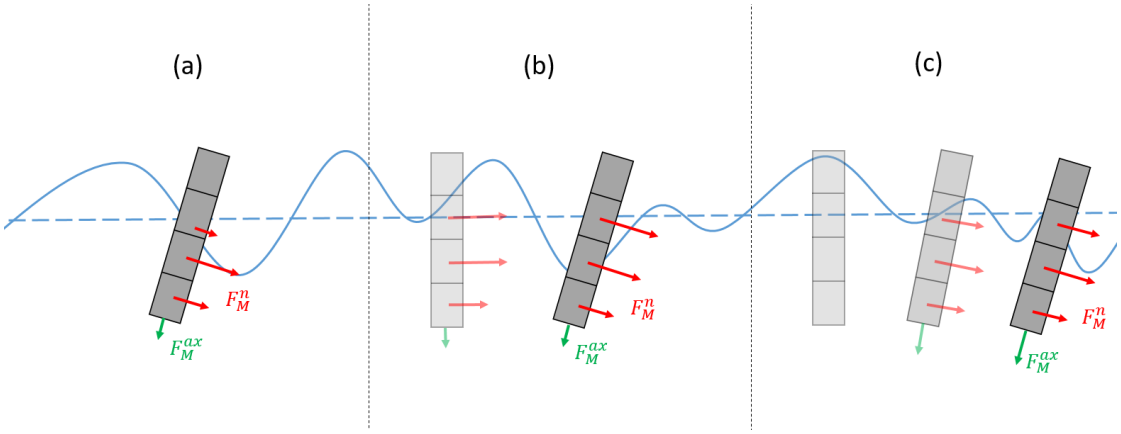

Figure 15: Options in QB for wave elevation and kinematics. (a) local instantaneous values; (b) values at the initial undisplaced position; (c) values at a low-passed position of the element.

3.5.4 References

[1] W.E. Cummins. The impulse response function and ship motions. *Schiffstechnik*, pages 101–109, 1961.

[2] A. Babarit, G. Delhommeau: Theoretical and numerical aspects of the open source BEM solver NEMOH. In Proc. of the 11th European Wave and Tidal Energy Conference (EWTEC2015), Nantes, France.

[3] Wamit,Inc. The state of the art in wave interaction analysis. Available at: https://www.wamit.com. Accessed 19.11.2021.

[4] O. M. Faltinsen. *Sea Loads on Ships and Offshore Structures*. Cambridge University Press, 1993.

[5] Duarte, T. and Sarmento, JNA., Jonkman, J. Effects of Second-Order Hydrodynamic Forces on Floating Offshore Wind Turbines, 32nd ASME Wind Energy Symposium, 10.2514/6.2014-0361.

[6] Engebretsen, E., Pan, Z., Fonseca, N., Second-Order Difference Frequency Loads on FPSOS by full QTF and relevant Approximations

[7] Newman, J.N., Second-order, slowly varying forces on vessels in irregular waves, In: Proceedings of International Symposium on Dynamics of Marine Vehicles and Structures inWaves, London, UK 1974

[8] Standing, R., Brendling, W., Wilson, D., Recent developments in the analysis of wave drift forces, low frequency damping and response, In: Proceedings of the Offshore Technology Conference, Houston, USA 1987.

[9] Pinkster, J. A., Low Frequency Second Order Wave Exciting Forces on Floating Structures, 1980.

[10] Lemmer, F., Yu, W., Luhmann, B., Schlipf, D., Cheng, P. W., Multibody modelling for concept-level floating offshore wind turbine design, Multibody System Dynamics 49, 2020.

[11] Standing, R.G., Brendling, W.J., Wilson, D., Recent Developments in the Analysis of Wave Drift Forces, Low-Frequency Damping and Response, Paper presented at the Offshore Technology Conference, Houston, Texas, April 1987 .

[12] Morison, J. R.; O'Brien, M. P.; Johnson, J. W.; Schaaf, S. A. (1950), "The force exerted by surface waves on piles", *Petroleum Transactions*, American Institute of Mining Engineers, **189**: 149–154.

[13] IEC Standard 61400-3-1, Wind energy generation systems – Part 3-1: Design requirements for fixed offshore wind turbines, 2019.

[14] USFOS Theory, Description of use and Verification Manual, available at https://www.usfos.no/manuals/usfos/theory/documents/Usfos_Hydrodynamics.pdf, last access 21.11.2021.

3.6 VERIFICATION AND VALIDATION

In order to achieve a fully validated hydroelastic tool, the individual hydrodynamic modules within QB were first validated individually. Once this was achieved, the different modules were combined to performed fully hydroelastic tests. The validation of the different hydrodynamic models within QB was performed using two different floating offshore wind turbines in a series of defined test cases with increasing complexity.

The first model, named OC3 model in this document, is the floating 5 MW wind turbine mounted on a spar buoy from the OC3 Report [1]. The second model, named OC4 model here, is the floating 5 MW wind turbine mounted on a semisubmersible substructure from the OC4 Report [2]. For the latter turbine, two different hydrodynamic modelling approaches were used. The first approach follows the LPMD model presented in Section 3.5.1 and includes quadratic drag forces via the Morison equation. The second approach uses the full Morison equation to account for the drag and added mass effects. This approach is termed ME, which stands for Morison Equation. The hydrodynamic definitions and coefficients of the different OC4 modelling approaches were taken from [2]. As for the OC3 model, only the LPMD approach was used. The hydrodynamic definitions and coefficients were taken from [1].

The results were validated against the Open-Source aerohydroelastic code OpenFAST [3] (version 2.5.0). The same turbine models and test cases were setup and used in QB and OF. Not all of the hydroelastic modelling capabilities of QB are present in OF. When validating certain hydrodynamic models, the hydroelastic capabilities of QB Ocean were adapted to reflect those of OF to have a better comparison. These modifications are mentioned in the appropriate tests below.

The test cases can be split broadly into three groups: no wave tests, regular wave tests and irregular wave tests. In the following subsections, the validation cases for each turbine model are presented in detail.

The subsections are ordered in such a way as to account for increasing modelling complexity. This comes on the one hand from the increased complexity of the test cases and on the other hand from the increased model complexity. In the final subsection, the full hydroelastic capabilities of QB are shown for the case of the flexible OC4 model.

3.6.1 OC3 LPMD Model

The OC3 LPMD model was validated in no wave tests, regular wave cases and irregular wave cases. This model was considered in order to have a simple geometry to test the different hydrodynamic models. Figure 16 shows the OC3 LMPD model within the QB GUI. The substructure was considered rigid in this model to evaluate only the hydrodynamic modules. For this model, the mooring system was modeled explicitly and the localised buoyancy model was used.

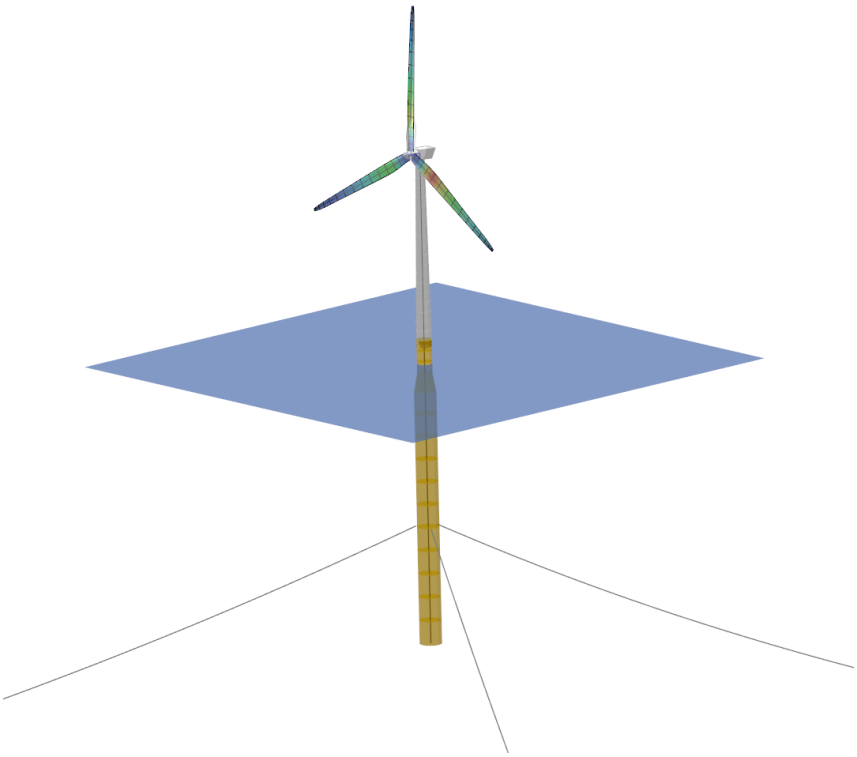

Figure 16: The OC3 model in QB featuring a spar buoy substructure.

No Wave Tests

The no wave tests are split into two parts, the first and main part consists in free decay tests in still water. The second part considers the turbine reaction to no wave and constant current conditions. The results from the decay tests will first be described and later results for the constant current tests.

The free decay tests simulate the turbine model in free decay from an initial position in still water condition. No aerodynamic loads were considered in the decay tests. All the 6 degrees of freedom (DOFs) are considered for in the decay tests. The evaluation of the results is done 1) visually, by inspecting the time series of all isochronic DOFs and 2) quantitatively, by analyzing the eigenfrequency and damping of the disturbed DOF. The latter analysis was done according to the procedure presented in [4].

Figure 17 – Figure 19 show the time series for the decay tests of the surge, heave and pitch DOFs. From these figures it can be seen that the predictions from QB and OF have excellent agreement. This is not only the case for the initially disturbed DOF but for the other DOFs as well. In the surge and pitch decay tests, there is a small offset between the heave time series. This offset comes from the different way the buoyancy is calculated between OF and QB. In OF, the buoyancy is accounted for by linearised stiffness matrices. In QB, the buoyancy forces is taken are calculated explicitly by taking into account the locally displaced water volume.

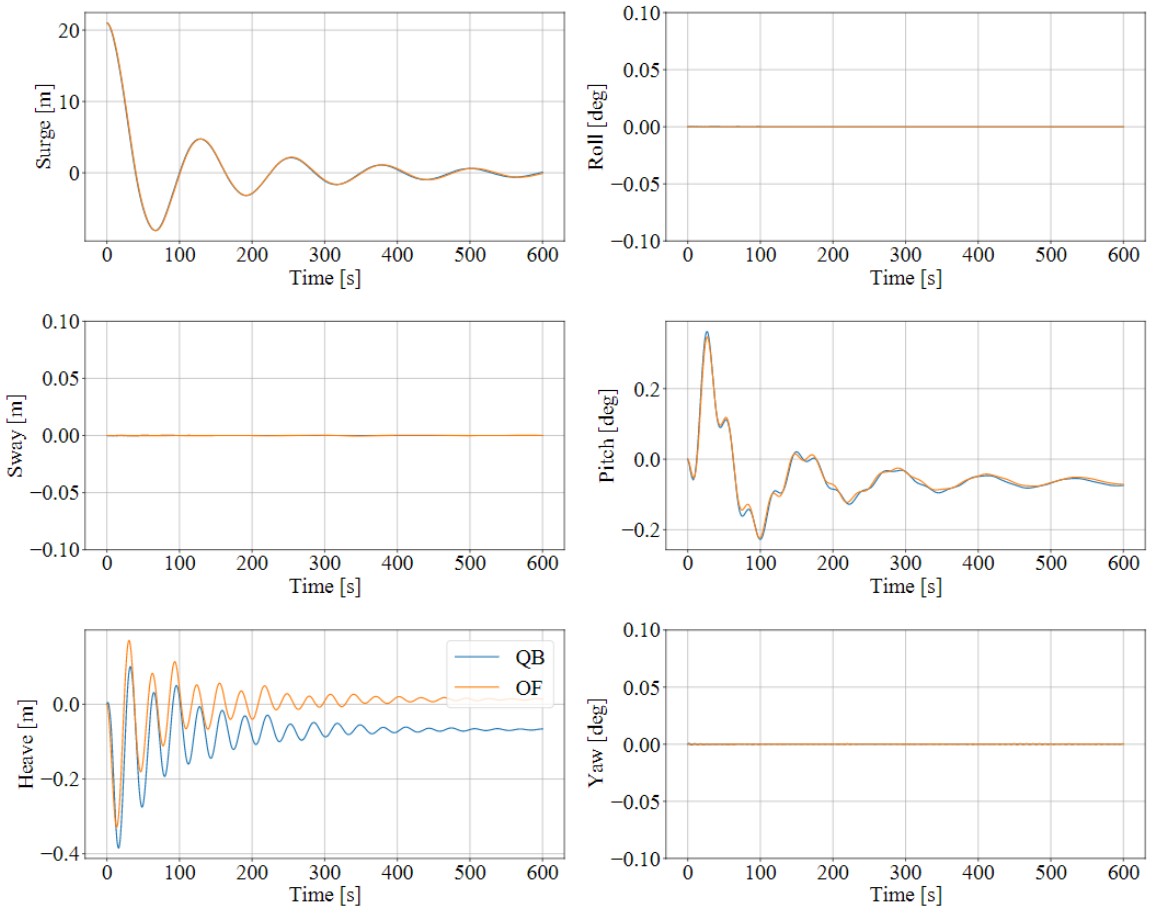

Figure 17: Time series of the surge decay test for the OC3 LPMD model.

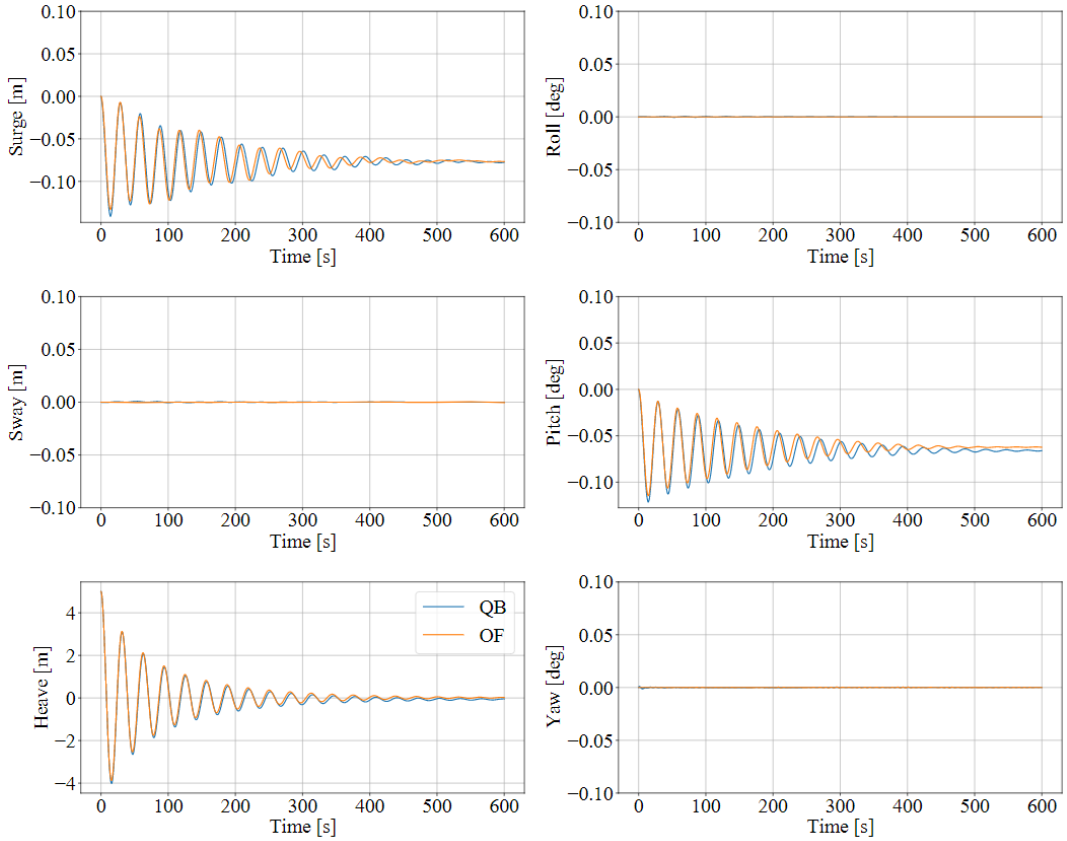

Figure 18: Time series of the heave decay test for the OC3 LPMD model.

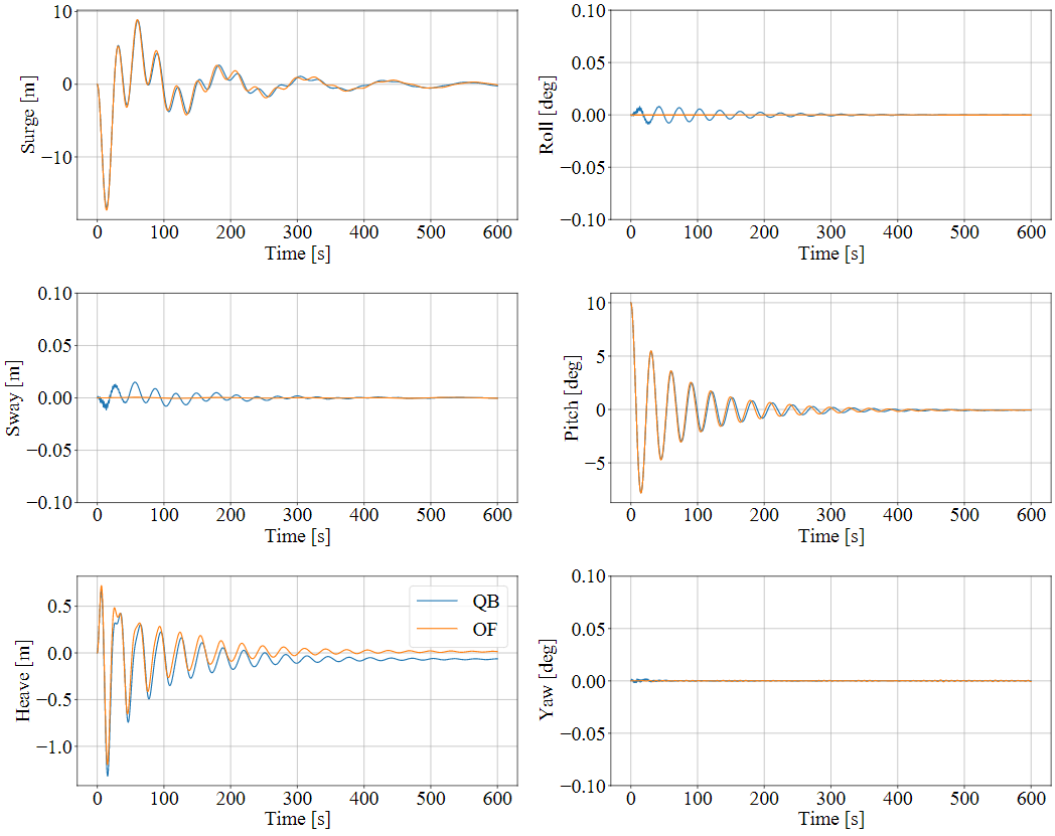

Figure 19: Time series of the pitch decay test for the OC3 LPMD model.

The decay tests for the other three DOFs (sway, roll, yaw) were also simulated. The time series are not included in the report since the findings are very similar.

Figure 20 – Figure 22 show the corresponding tensions at the fairlead and anchor locations of the mooring systems for the surge, heave and pitch decay tests. It can be seen good agreement between both codes. Again, for the heave decay tests, there is a small offset in the tensions between the QB and OF simulations. It can be explained by the small offset in the heave neutral position between both codes and the different approaches used in both codes to model the mooring system.

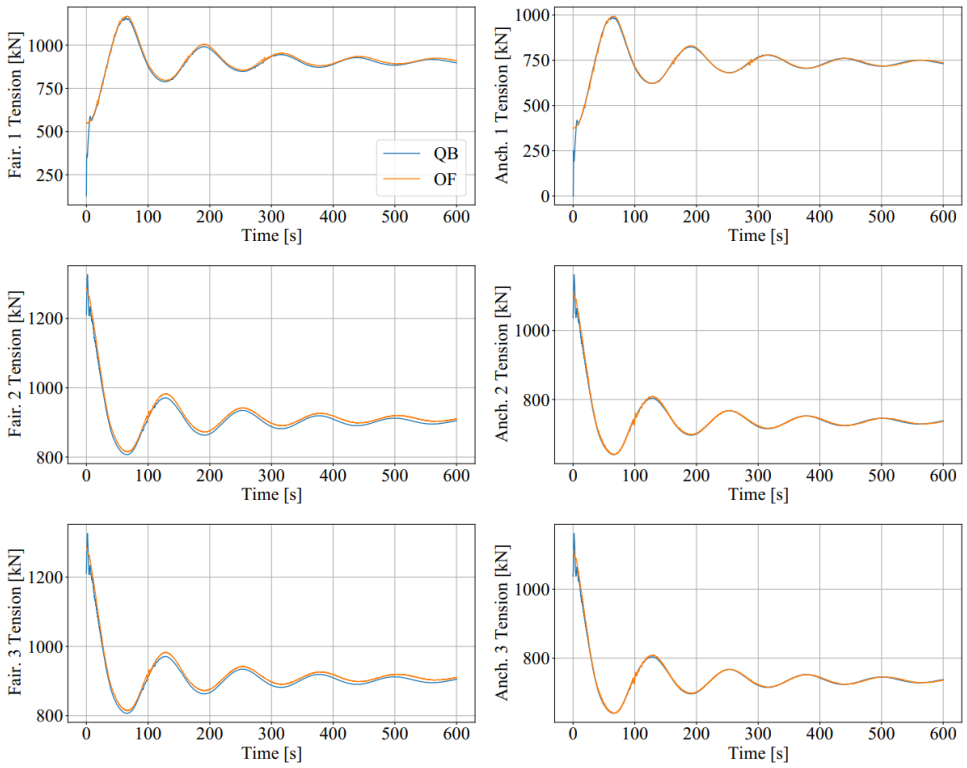

Figure 20: Mooring line tensions for the surge decay test for the OC3 LPMD model.

Free decay tests were also carried out for the other DOFs, however due to symmetries they elucidate no new results. They too are characterised by excellent agreement with OF. They have therefore been omitted here for brevity, however are included in Appendix A1.1.

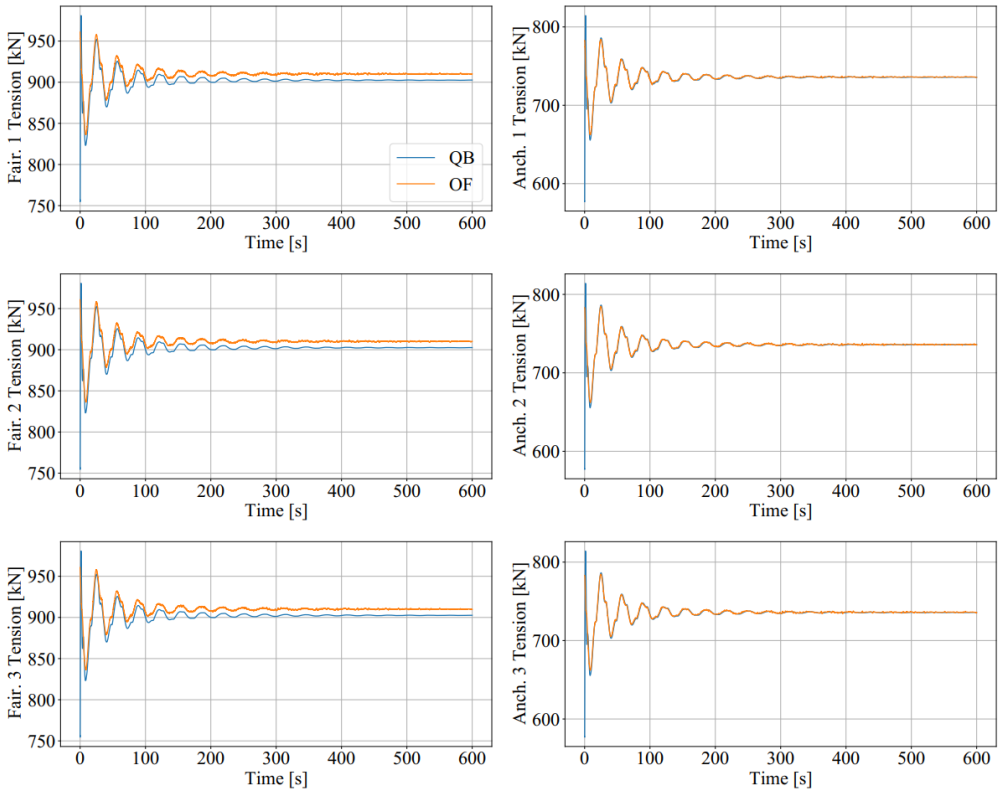

Figure 21: Mooring line tensions for the heave decay test for the OC3 LPMD model.

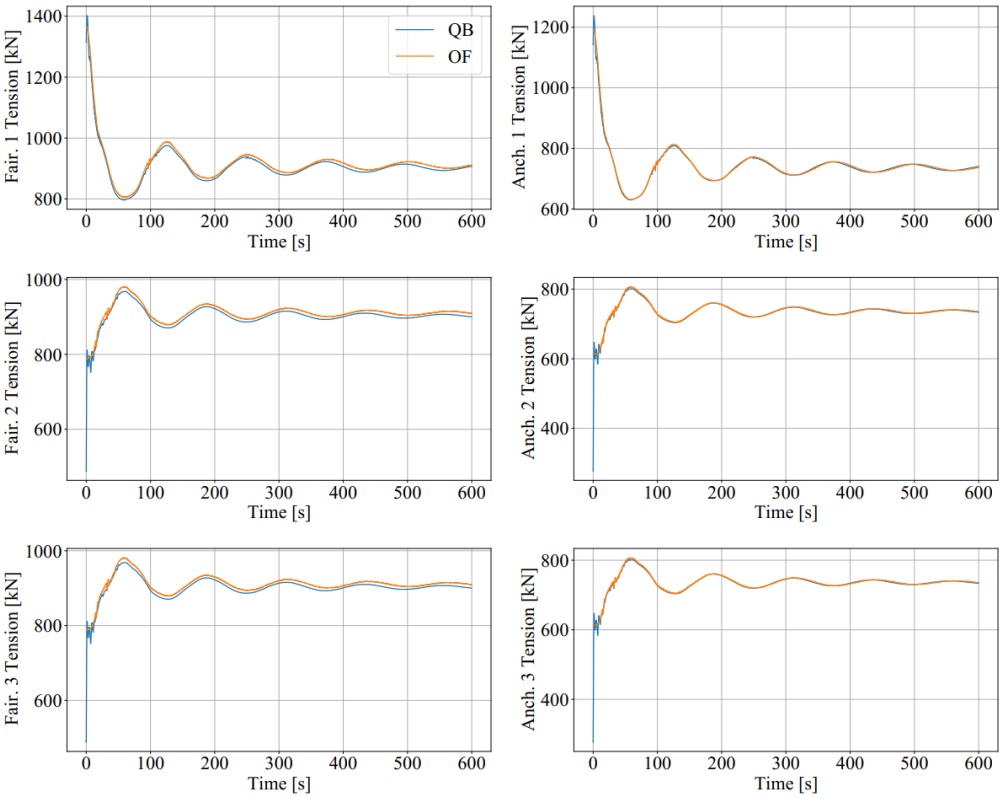

Figure 22: Mooring line tensions for the pitch decay test for the OC3 LPMD model.

The decay tests were also analyzed quantitatively by comparing the eigenfrequencies and damping characteristics of the floater for the initially displaced DOFs. Figure 23 shows the results for the six performed decay tests. It can be seen in this figure that the normalised eigenfrequencies agree very well between both codes. There are significant differences in the damping characteristics, especially for the surge, sway, heave and yaw DOF.

The differences are assumed to come from the different mooring system models. OF uses MoorDyn, which uses a lumped-mass formulation for modelling axial elasticity [5]. QB uses a cable structural formulation (Section 3.2) coupled with the Morison equation (Section 3.5.3) to account for the hydrodynamic forces on the mooring system. In order to test if the mooring system formulation causes the different damping behavior, the mooring system models were replaced by linear stiffness matrices in both codes. Since there is a significant linear damping term in the hydrodynamic matrices in the surge, sway, heave and yaw DOFs, a linear damping relation was assumed for the evaluation of the time series.

Figure 24 shows the eigenfrequencies and linear damping characteristics for the models with linearised mooring systems. It can be seen now that the values for all DOFs except the yaw DOF align. For this turbine model the yaw DOF does not couple with the other DOFs and is almost exclusively determined by the stiffness, damping and inertia matrices, since the quadratic damping term of the Morison equation is not applied to cylinder rotations. So the decay behavior can be calculated analytically. Using the stiffness, inertia and damping values and adding the rotational inertia of the turbine, an analytic eigenfrequency of 0.118 Hz was determined. This value is only 3% off from the values gotten in the QB and OF calculations. The analytical damping ratio is 4.4%. This value differs from the one obtained in QB simulations by 0.5% and from the one by OF simulations by 17%. It is therefore assumed that the value obtained by QB simulations is the correct one.

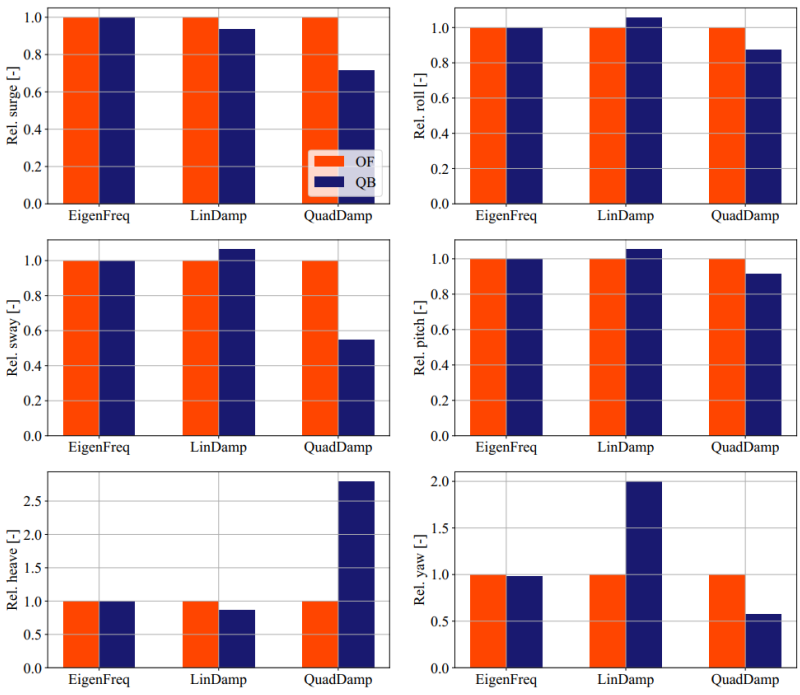

Figure 23: Relative eigenfrequencies and damping behaviour of the OC3 model for the considered decay tests.

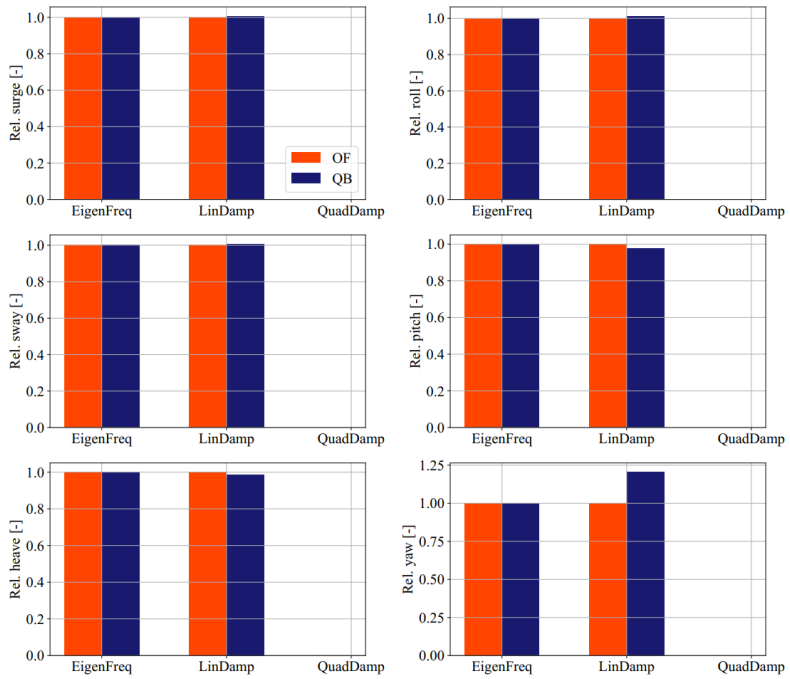

Figure 24: Relative eigenfrequencies and damping behaviour of the OC3 model for the considered decay tests using a linearised mooring system.

The second part of the no wave tests comprised constant current tests. For these tests, two current profiles were selected according to [6]: a power-law profile – representing a tidal current velocity – and a linear profile – representing a wind-generated current. The current direction is aligned with the positive surge direction. The turbine was initially in its original undisplaced position and the simulations included the transient response to the current profiles. No aerodynamic loads were applied in this case.

Figure 25 shows the time series of the wind-generated current test with a surface current magnitude of 3 m/s and decrease rate of 0.2 1/s. The direction of the current aligns with the positive surge direction of the turbine. It can be observed in this figure that the turbine behaves almost identically for the affected DOFs (surge and pitch) when simulated with QB and OF. The different behavior in the heave DOF can be attributed to the different ways the buoyancy is modelled in QB and OF. The right column plots of Figure 25 show the water particle velocities at three different locations along the turbine substructure: at 0 m, at -10 m and at -20 m. As QB outputs flow quantities at the geometric center of submerged members, the position of the sensor translates and rotates with the floater. The relative water velocity therefore corresponds to the translated and rotated position and orientation. This differs from the OF relative water velocity outputs, which are at fixed global positions. In order to demonstrate that the results are in fact in agreement, an additional QB run was carried out where the floater was fixed in space, allowing extraction of the current velocities in a way comparable to OF. Taking this into account, Figure 25 demonstrates that decay of the sea current velocity as a function of depth agrees well between both models.

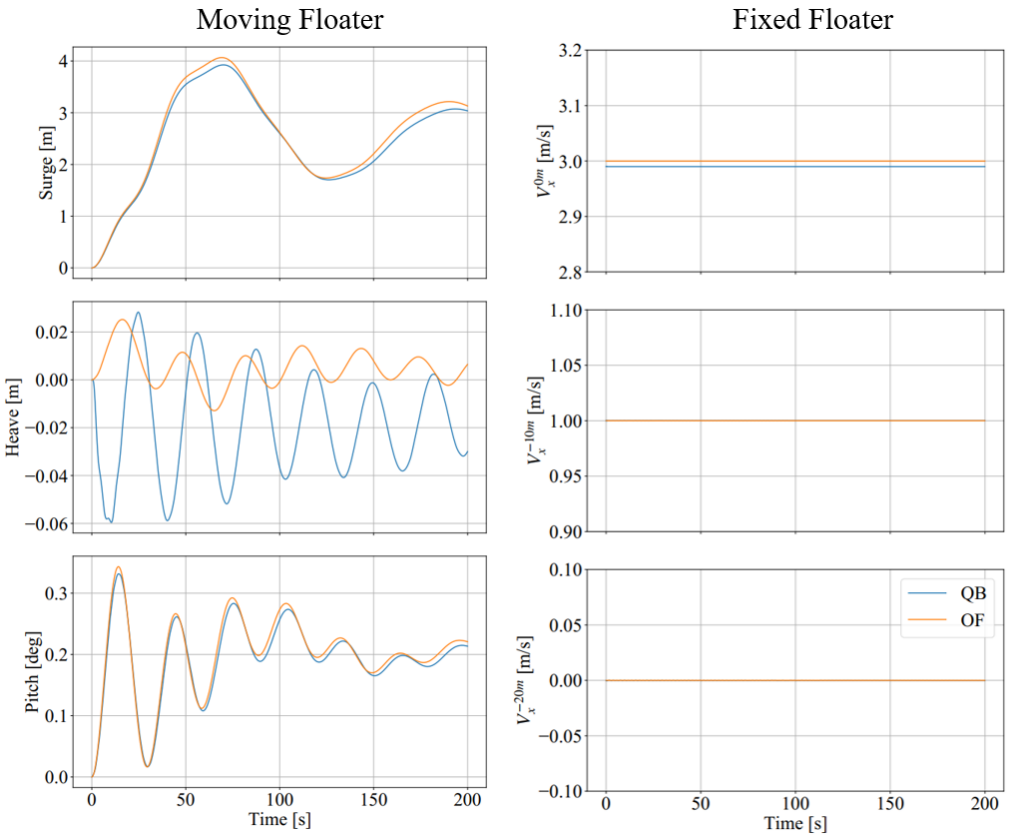

Figure 25: Displacements and water velocities for the OC3 model in a wind-generated current test case.

Regular Wave Tests

The regular wave cases aim to validate the implementation of the first-order wave excitations forces in QB. This done in load cases where a single wave train with varying amplitude, period and direction is used to model the sea state. Due to the good agreement between both tools, for brevity the direction of the incoming wave is only analyzed for one case. In order single out the effect of the excitation force implementation, the respective models in both simulation tools are set up to be as identical as possible. Therefore, the mooring system and the buoyancy are modeled with a linearised stiffness matrix. Both tools make use of the same excitation force IRF computed in WAMIT. No wave stretching model was used in QB so that the modelling considerations between QB and OF were as close as possible. OF does currently not allow wave stretching models to be implemented in HydroDyn [7].

Load case	Wave amplitude [m]	Wave period [s]	Wave direction [deg]
2.1	3	10	0 / 45 / 90 / 135
2.2	4	10	---
2.3	3	12	---
2.4	4	12	---

Table 2: Load cases to validate the implementation of the first-order wave excitation forces in QB

Similar to the free decay tests, no aerodynamic loads were considered. The validation is done by analyzing the time series and frequency spectra of the excited OC3 model.

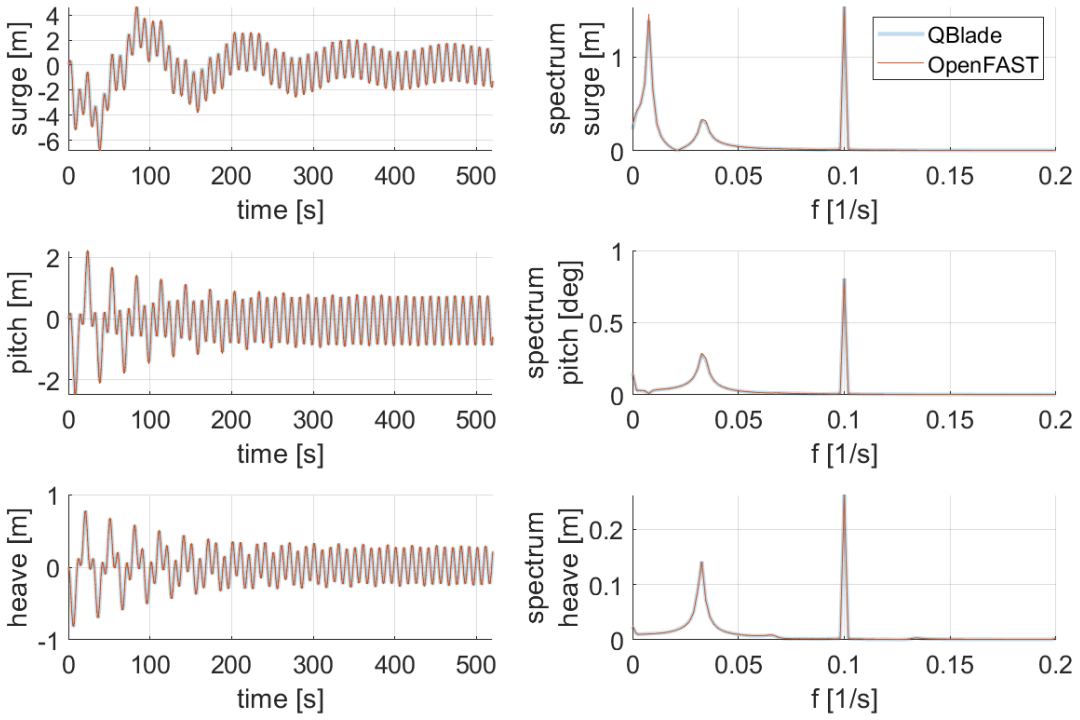

Figure 26: Time series (left column) and corresponding spectra (right) of relevant DOFs for load case 1 (0°)

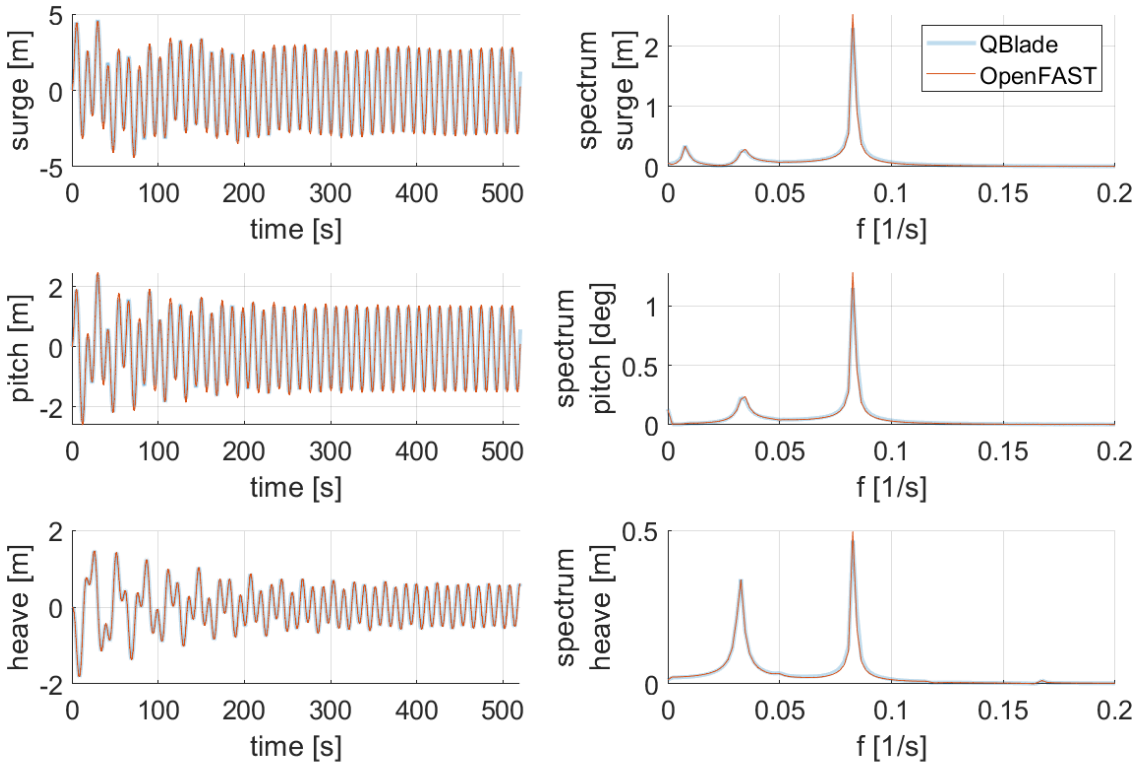

Figure 27: Time series (left column) and corresponding spectra (right) of relevant DOFs for load case 4.

Figure 26 and Figure 27 show the time series and corresponding spectra of the three DOFs (surge, heave, pitch) excited by an incoming wave from 0° direction (surge, heave, pitch) for load cases 2.1 and 2.4. An initial transient is present and completely damped out after approximately 300s. This explains the additional peaks at lower frequencies than the wave frequency in the spectral plot. Afterwards, a steady excitation by the linear wave is present in all DOFs. It can be noted that the translations and rotations of the floater are predicted in an identical manner between both tools. Hence, a correct implementation of the first-order wave excitation loads may be concluded. It can be further noted that changing the wave height and period does not induce any differences between both tools.

The next feature requiring validation is the influence of waves that approach the floater with a nonzero heading angle. The excitation input file provides IRFs with a degree spacing of 10 degrees (-180°:10°:180°). Thus, a wave that heads in from an intermediate angle requires interpolation of the IRF. In order to validate this, Figure 28 shows the time series of all DOFs[1] for load case 2.1 with a wave angle of 45 degrees. As one would expect, surge and sway as well as pitch and roll are excited equally. Once again both tools show very good agreement in the floater response. Very slight differences in the yaw DOF might be attributed to differences in the interpolation algorithms.

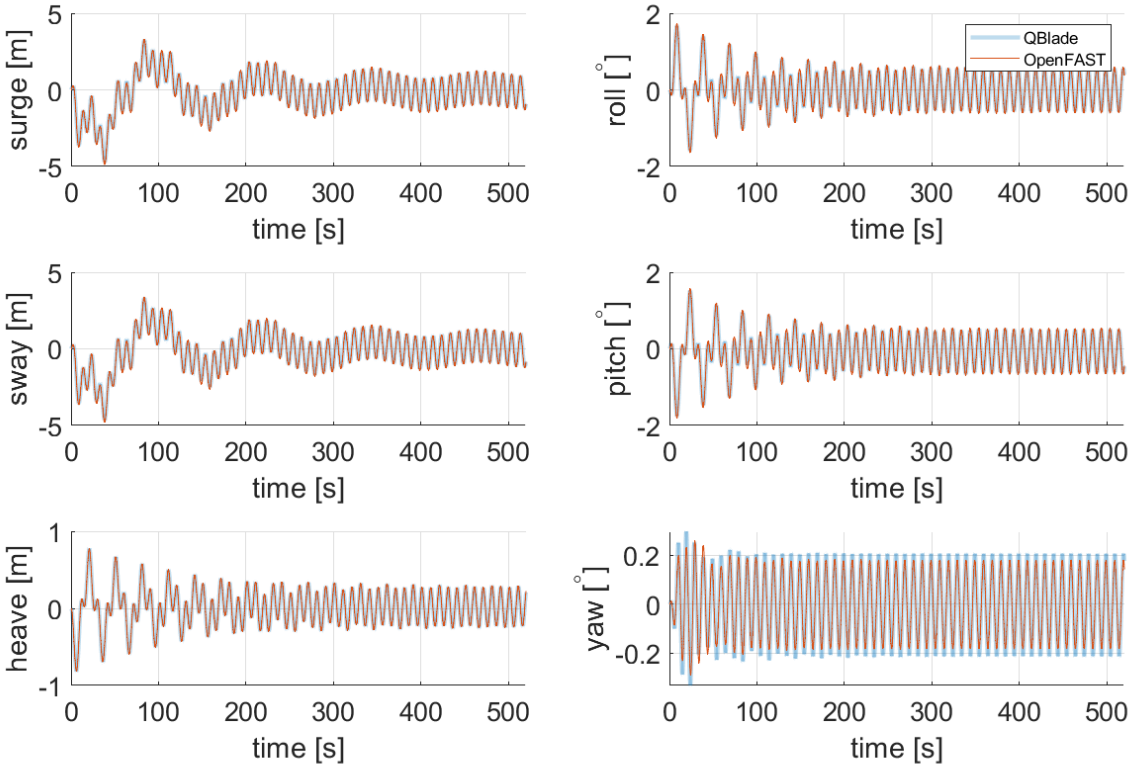

Figure 28: Time series of all DOFs for load case 1 (45°).

[1] Since all DOFs are excited now

Irregular Wave Tests

The validation of the first-order excitation loads in irregular waves was performed in a similar fashion to the regular wave cases. Accordingly, the mooring system and buoyancy are modelled via linearised matrices. The IRFs were precomputed in WAMIT and are identical to the ones used in OF. At this point it is worth mentioning that the algorithmic approach doesn't change within the hydrodynamic model of QB for an irregular wave field compared to a wave field consisting of a single wave train. The reason is, that the excitation loads are computed for every single wave train and superposed linearly (see Section 3.3.2).

Two separated cases are analyzed. Firstly, an irregular wave field computed on base of a JONSWAP spectrum with uni-directional waves is looked at. Secondly, a directional spread of the wave trains is added in order to further validate the direction-dependent calculation of the wave loads. To increase the statistical validity of the results, six runs were carried out for each simulated case. The significant wave height amounts to $H_s = 6\text{m}$ and the peak time period to $T_p = 10\text{s}$. A peak enhancement factor of γ = 3.3 was chosen. The floater response in all 6 DOFs will serve as the validation parameter. Finally, statistical parameters of the floater response and the tower base loads will be presented.

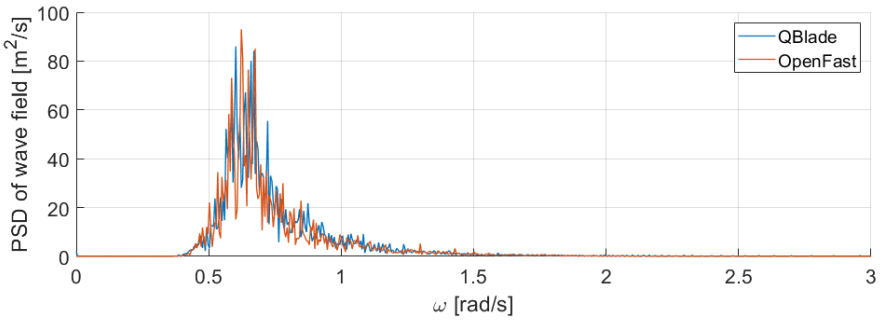

Figure 29: Averaged JONSWAP spectrum with $H_s = 6m$, $T_p = 10s$ and $\gamma = 3.3$.

Figure 29 shows the averaged wave fields that serve as an input to the calculation of the wave forces. In Figure 30 the floater response for an irregular wave field with uni-directional waves is presented. The three excited DOFs (surge, heave, pitch) show good accordance between QB and OF. The results are averaged over the last 250s of the aforementioned six runs, each with 800s total duration. The peak at the floater eigenfrequency arises due to not completely damped out initial transients. Figure 31 shows the PSDs of the floater response for multi-directional waves in all 6 DOFs. To reduce the influence of the initial transient, the total simulation length was set to 1200s. The PSDs are averaged over the last 300s of six different simulations. It becomes obvious that the hydrodynamic response of the OC3 floater is predicted very similarly between both tools.

Figure 32 shows the time average, the standard deviation as well as minima and maxima of the floater response in the 6 DOFs of both tools. Small deviations between the codes are visible but in general a similar behavior is visible once again. An exact matching between these statistical parameters may not be expected as they depend on the occurrence of severe wave groups. A longer simulation time would presumably increase the agreement between the compared codes.

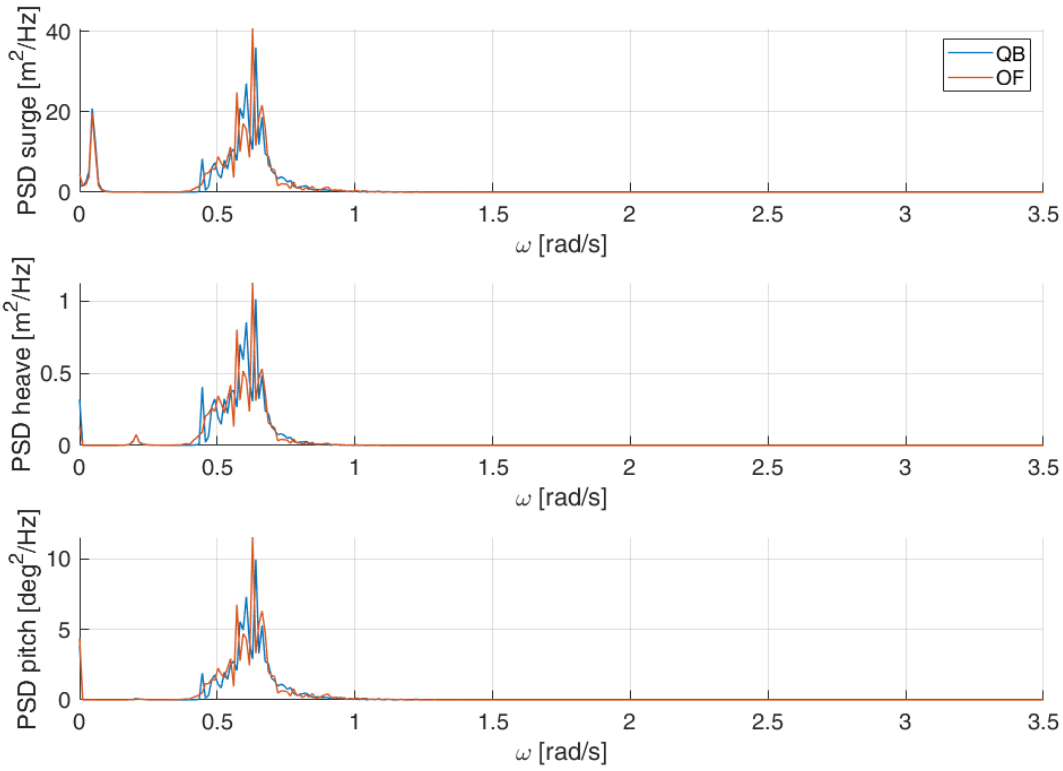

Figure 30: Averaged PSDs of the floater translations and rotations in uni-directional, irregular waves.

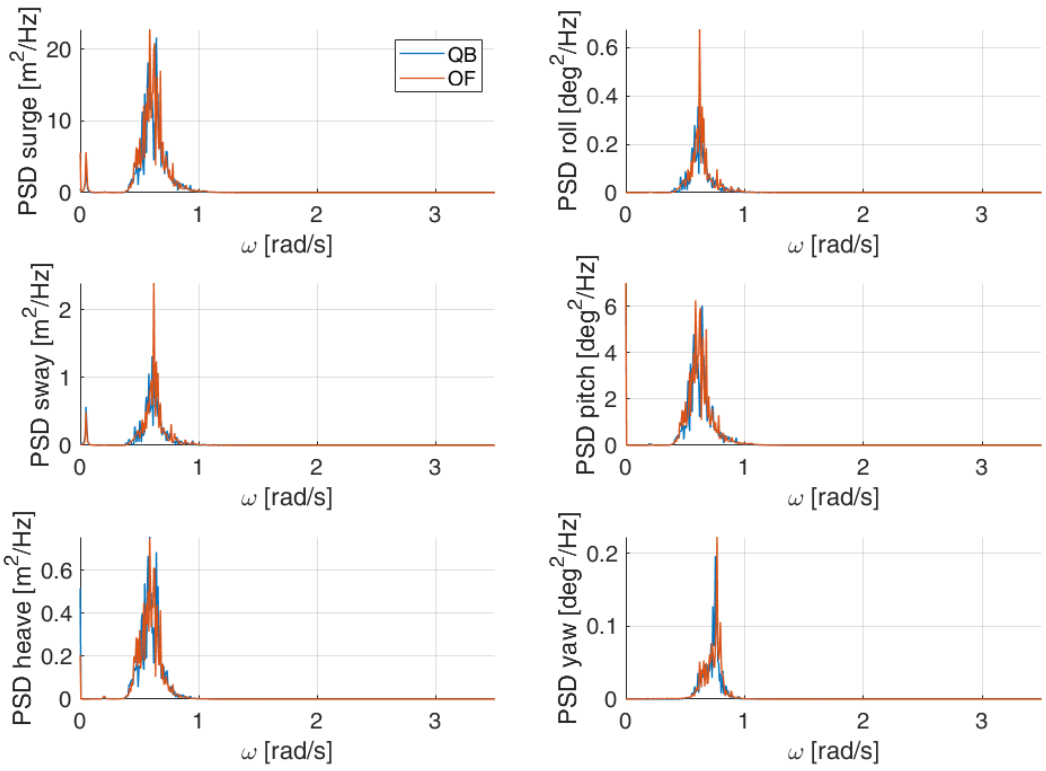

Figure 31: Averaged PSDs of the floater translations and rotations in multi-directional, irregular waves.

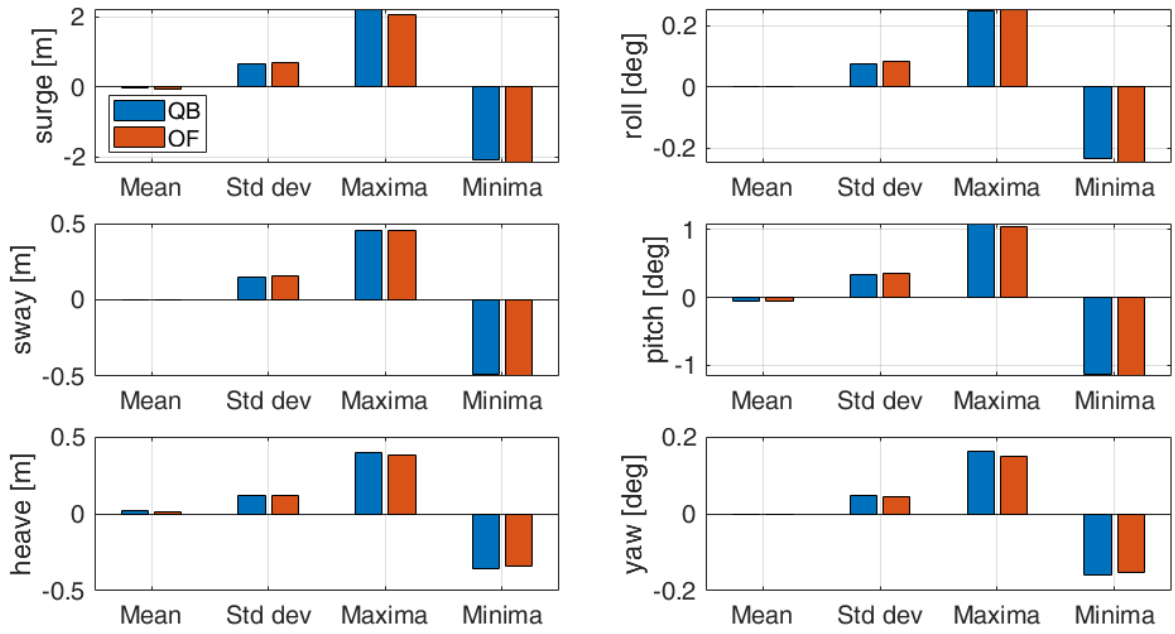

Figure 32: Statistical comparison of extreme values in all 6 DOFs for multi-direction irregular waves

Irregular wave Tests including current

For the irregular wave test cases, a combination of wave and currents was also considered. For this case, a JONSWAP spectrum with a significant wave height of H_s = 6 m, a peak time period of T_p = 10 s and a value of γ = 3.3 was chosen. This wave spectrum was combined with a constant tide-induced current with a power law of 1/7th and a surface current value of 0.5 m/s. The wave and current directions aligned with the positive surge direction. Six repetitions were considered to account for the statistical variance of irregular waves. In this test case, the same wave elevation input was used for OF and QB simulations. Again, no aerodynamic loads were applied on the turbine.

It can be seen in Figure 33 the averaged PSDs of the six repetitions for all DOFs for both simulations. The figure shows that the substructure dynamics for the relevant DOFs under irregular sea states and constant currents is virtually identical if simulated with OF or QB.

Figure 34 shows the averaged PSD of the corresponding tensions at the fairlead and anchor positions for the irregular wave plus current cases. It can be seen in this figure that there is a larger variation of the fairlead and anchor tensions for the downwind mooring lines (lines 2 and 3). This difference can be attributed to mooring system modelling differences between QB and OF. These could lead to differences in the prediction of the fatigue and extreme loads in the mooring system and require further validation. In Work Package 2, the mooring modelling approach used in QB will be validated against experimental data.

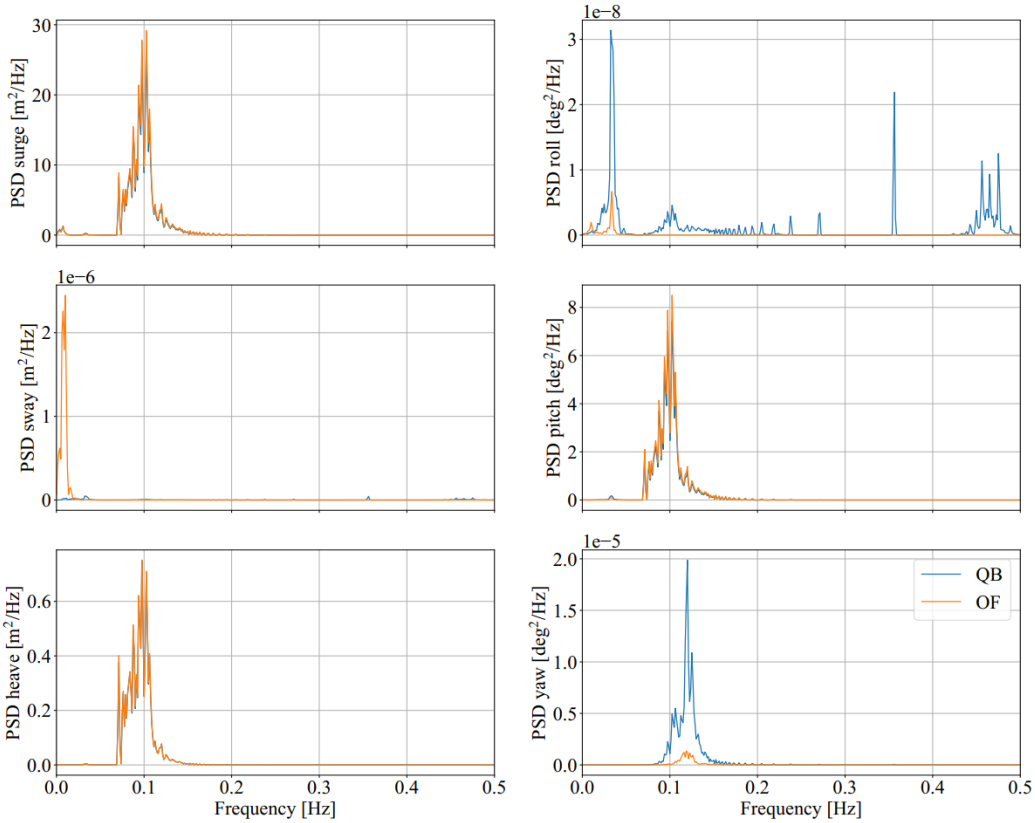

Figure 33: Averaged PSDs of all DOFs for irregular wave and current simulations

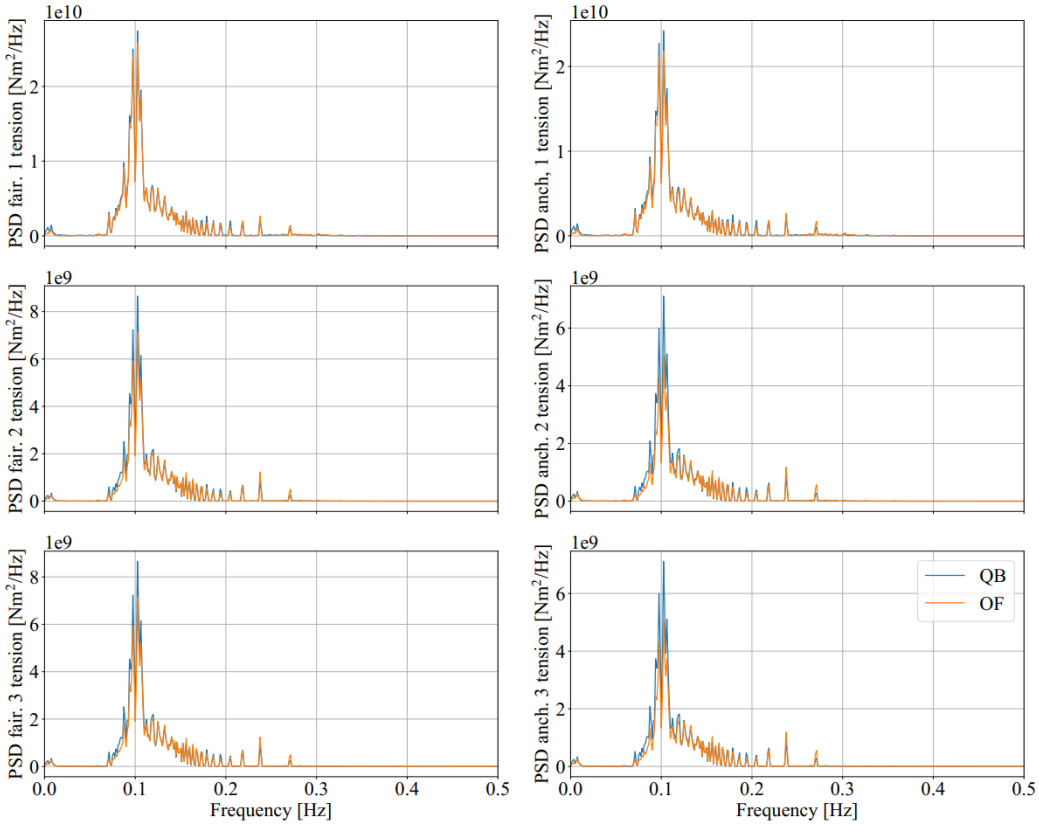

Figure 34: Averaged PSD of the fairlead and anchor tension for the irregular wave tests with constant current

3.6.2 OC4 LPMD Model

The geometry of the OC4 model within the QB GUI is shown in Figure 35. This figure shows clearly the more complicated geometry of the floater. Hence, the hydrodynamic behavior of this model is expected to be more complicated. The substructure was again considered rigid in this model to evaluate only the hydrodynamic modules in this more challenging geometry. Unless otherwise stated, the mooring system was modeled explicitly and the localised buoyancy model was used for this model.

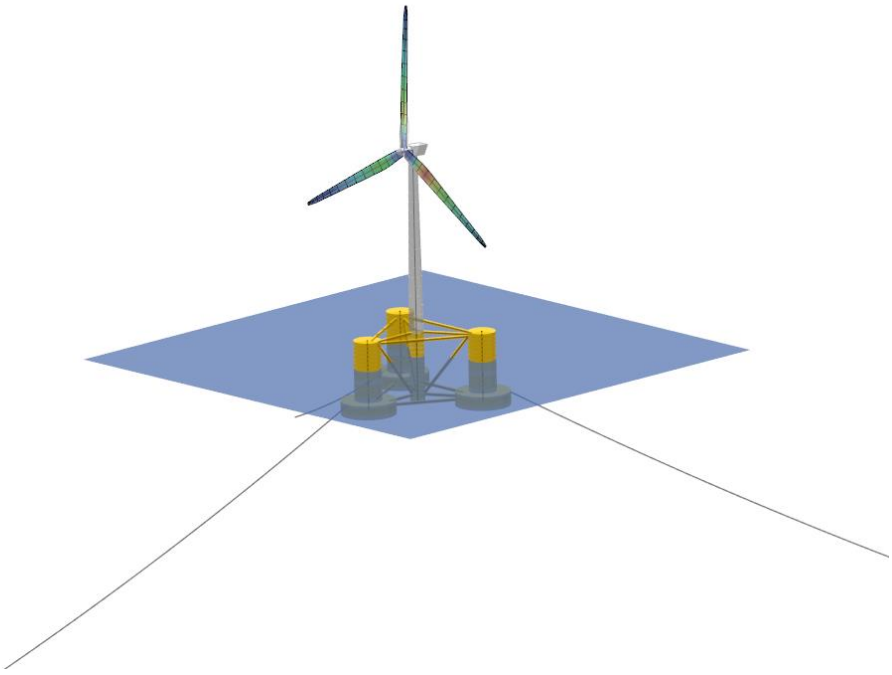

Figure 35: The OC4 model in QB featuring a semisubmersible substructure.

Free Decay Tests

For this model, decay tests were again performed in still water for four DOFs and compared to the same simulations performed with OF. Again, the main difference between both codes in these tests were the mooring system modelling and the way the buoyancy was calculated.

Figure 36 – Figure 38 show the free decay tests for the surge, pitch and yaw DOF. It can be seen again that the results for QB and OF are very similar. Especially for the disturbed DOFs and the DOF that are directly coupled to them, the differences between both codes are small. A small difference in the mean of the heave position can again be noted. This comes from the different buoyancy models used in QB and OF.

Figure 39 shows the corresponding tensions at the fairlead and anchor locations of the mooring systems for the surge decay tests. Again, it can be seen good agreement between both codes. There is an offset in the tensions between the OF and QB simulations. This can be explained by the small offset in the heave neutral position between both codes and also from the different modelling approaches used for the mooring system. The tensions for the other DOFs were also analyzed but not included here for brevity reasons. The findings of these other decay tests are equivalent those shown in Figure 39.

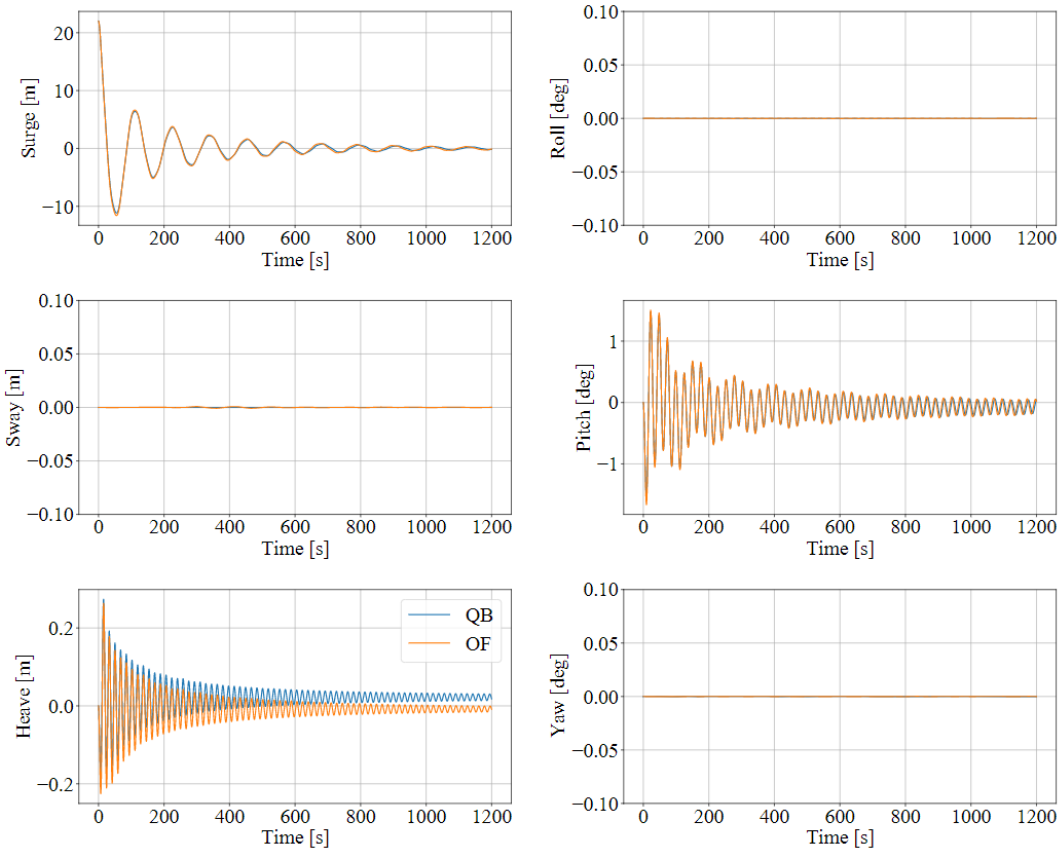

Figure 36: Time series of the surge decay test for the OC4 LPMD model.

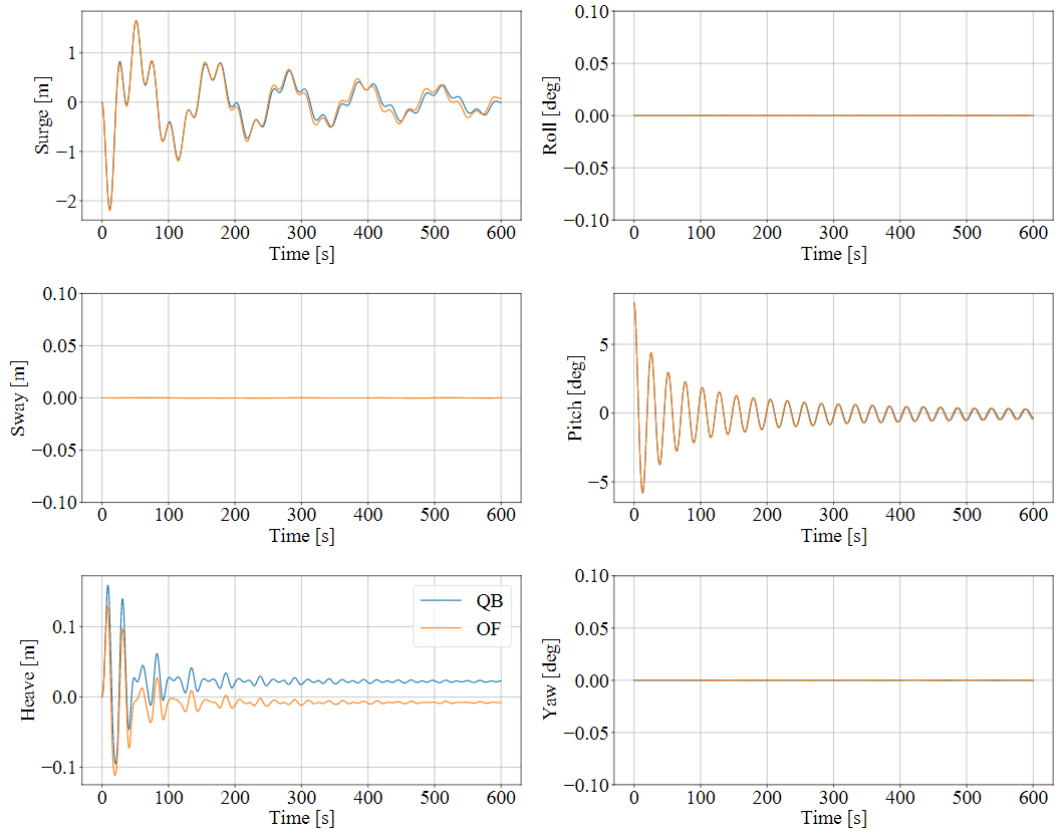

Figure 37: Time series of the pitch decay test for the OC4 LPMD model.

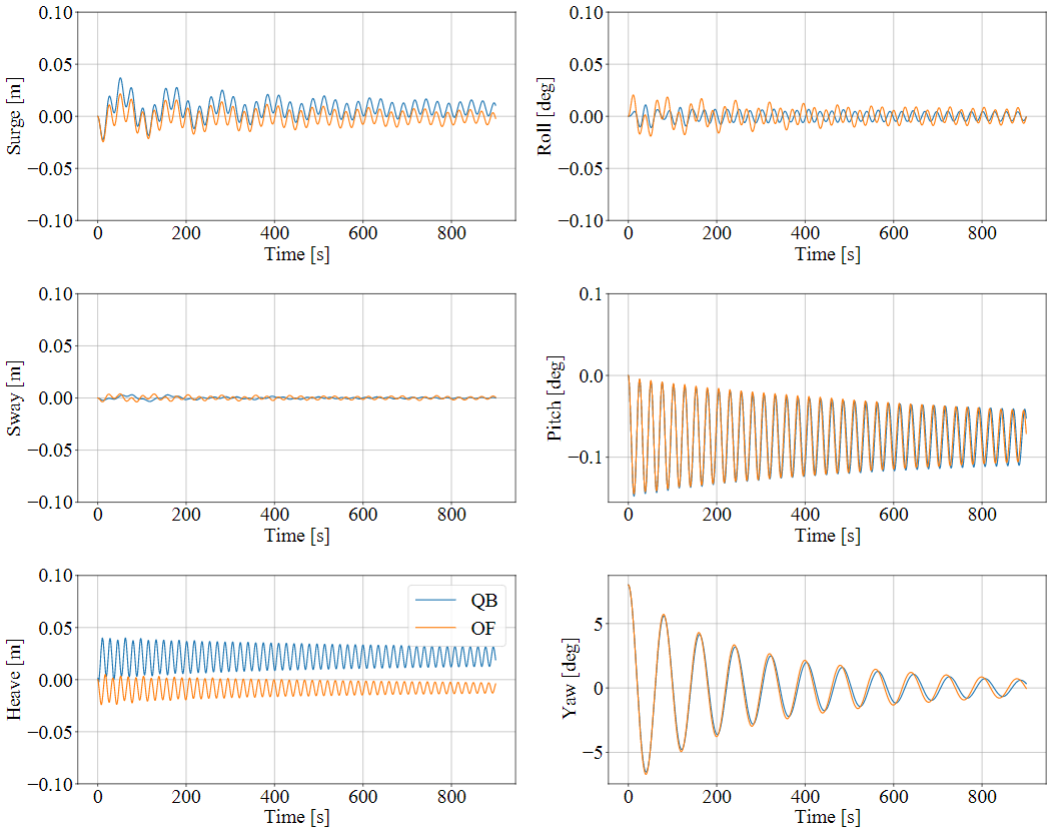

Figure 38: Time series of the yaw decay test for the OC4 LPMD model.

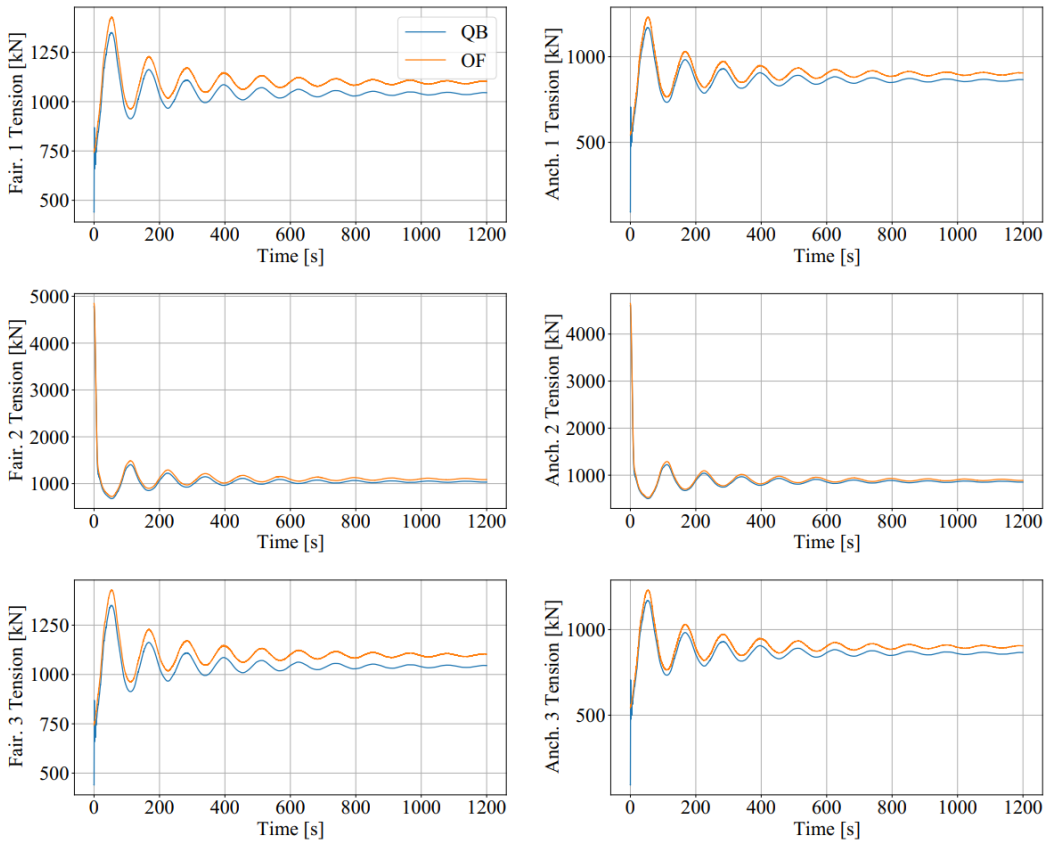

Figure 39: Time series of the mooring system tension in the surge decay test for the OC4 LPMD model.

The numerical values for the frequencies and damping coefficients of the decay tests were also analyzed for these cases. The results are shown in Figure 40. In this figure, it can be seen that the relative values of eigenfrequencies between both codes are close to 1. This agreement can also be seen visually in the figures above. The same can be said for the quadratic damping term. As for the linear damping term, it can be seen that there are some differences between the relative values of both codes. As with the OC3 model, the differences can be traced back to the different mooring system modeling used in both codes.

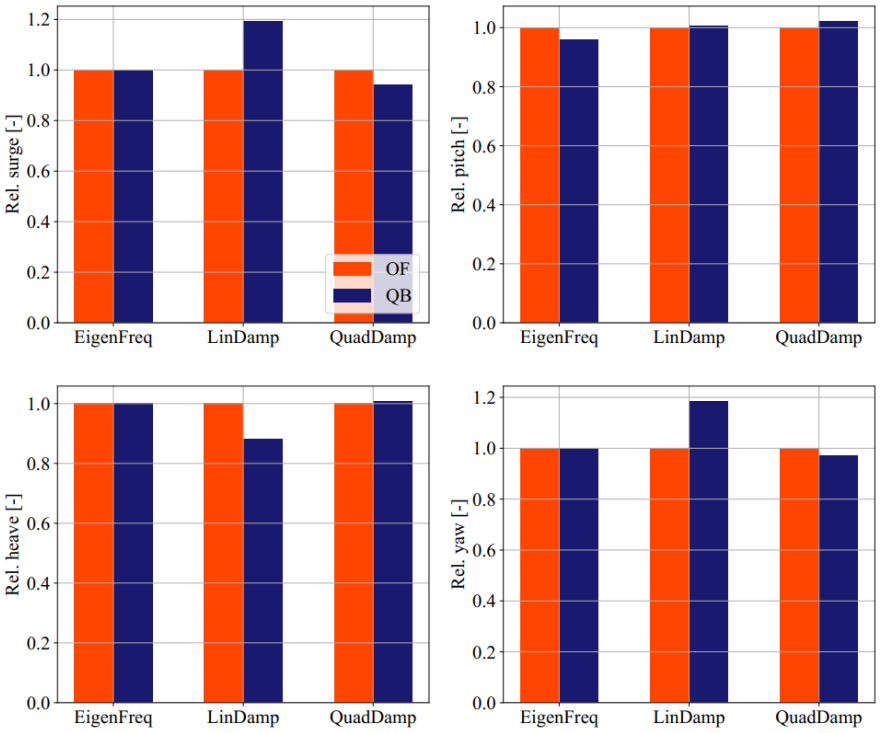

Figure 40: Relative eigenfrequencies and damping coefficients for the OC4 LPMD decay tests

Free decay tests were also carried out for the heave DOF and demonstrates excellent agreement with OF. This has been omitted here for brevity and is included in Appendix A1.2.

Regular Wave Tests

The regular wave tests were performed with linear Airy waves for two selected cases. One case had a wave range of H = 6 m and a period of T = 10 s. The second case had a wave range of H = 8 m and a period of T = 12 s. For these cases, a simulation time of 1000 s was chosen and the first 300 s were discarded. This is because focus was on the response of the turbine once the initial transients were settled. No aerodynamic loads were considered and the wave direction was chose to coincide with the direction of the positive surge DOF. As for the wave tests for the OC3 model, no wave stretching model was applied in QB so that the modelling considerations between QB and OF were as close as possible. OF does currently not allow wave stretching models to be implemented in HydroDyn [7].

It should be noted here that for the more complex geometry of the OC4 model, the buoyancy model will affect the response of the substructure to the incoming waves. This comes from the fact that the bodies

that provide buoyancy for the OC4 model are spatially distributed. As the wave passes the substructure, the local buoyancy forces induce additional forces and moments that affect the principal DOFs of the substructure. These forces and moments are not accounted for if only a linear constant force and restoring force matrix is used to account for the buoyancy.

To verify the hydrodynamic models for the radiation forces, the wave excitation forces and the diffraction forces as well as the quadratic drag forces from the Morison equation, a modified OC4 LPMD model was build that includes a linear buoyancy model in a similar fashion as OF. This model was termed “QB Lin” in this section. Additionally, the complete OC4 LPMD model with the distributed buoyancy forces was also modelled. This model was used to analyze the effect of the buoyancy model on the substructure response and on the tensions of the mooring system.

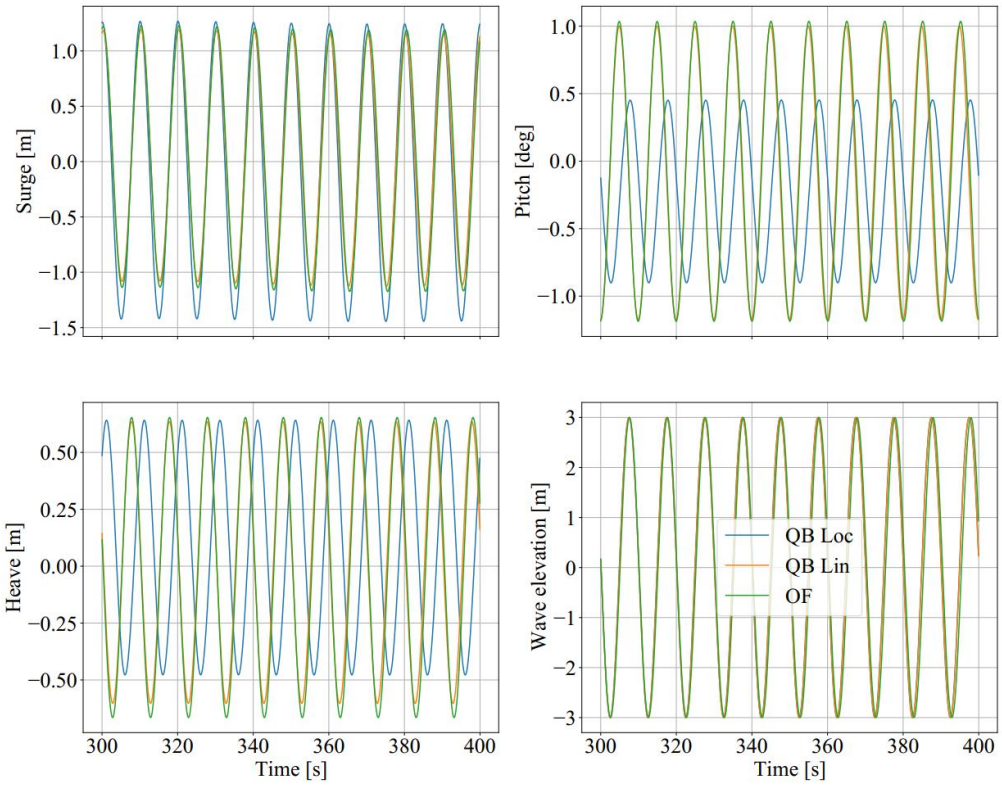

Figure 41: Relevant DOFs and wave elevation for regular sea state with H = 6 m and T = 10 s. QB Loc = QB local buoyancy model, QB Lin = QB linear buoyancy model.

Figure 41 shows the response of the surge, heave and pitch DOF as well as the wave elevation for the test case with H = 6 m and T = 10 s. It can be seen in this figure that the response of the linear buoyancy model in QB (QB Lin) is practically identical to the response in OF. This validates the hydrodynamic modules for radiation, diffraction and wave excitation forces as well as the quadratic drag forces in the more complicated geometry of the OC4.

If the local buoyancy model is used in QB (QB Loc), it can be seen in Figure 41 that all the relevant DOFs are affected. It can be seen that the surge DOF oscillates with a larger amplitude and reaches more negative values compared to the linear buoyancy model. In addition, the amplitude and phase of the pitch

and heave DOFs change if the local buoyancy model is used. In particular, the amplitude of both DOFs is smaller and the phase shifts with a positive magnitude. This behavior was not seen in the regular wave calculations of the OC3 model because all the buoyancy forces were concentrated on the spar axis and were not spatially distributed.

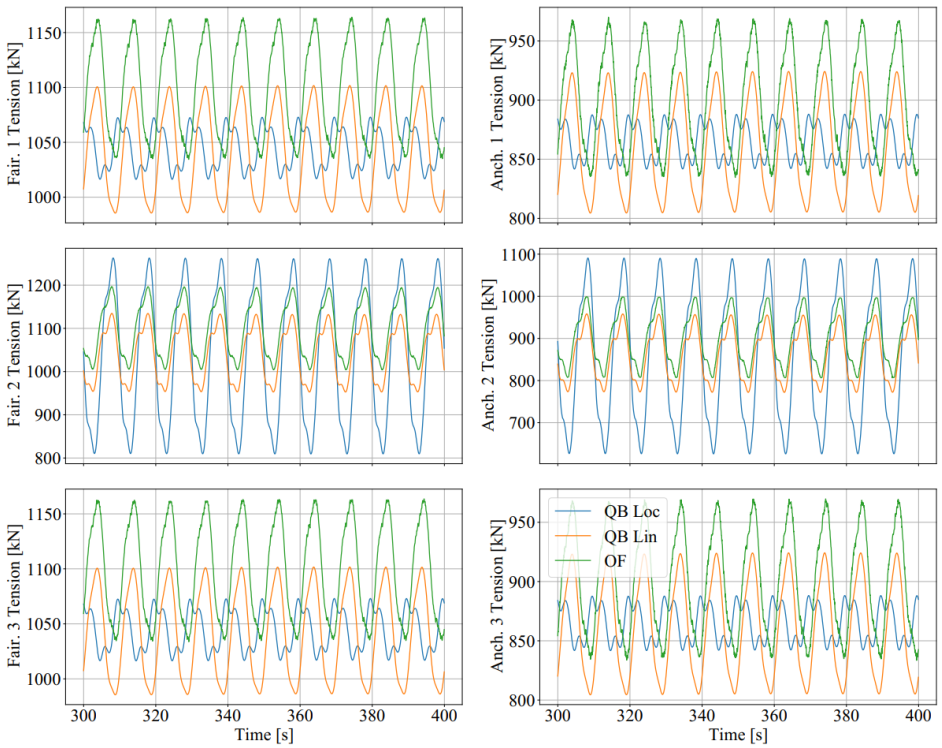

Figure 42: Mooring line tensions for regular sea state with H = 6 m and T = 10 s. OF = OpenFAST, QB Loc = QBlade Ocean local buoyancy model, QB Lin = QBlade Ocean linear buoyancy model

This different behavior due to the local buoyancy model also has an effect on the tensions of the mooring system. In Figure 42 it can be seen the mooring line tensions of the regular sea state shown in Figure 41. Figure 42 shows that the mooring tensions of the OF calculations have a slightly higher average value than the tensions in the QB Lin calculations. If one observes the fairlead tensions, the OF calculations have about a 5% higher mean for all three mooring lines compared to the QB calculations. This offset was also identified in the decay tests and is attributed to the different mooring system modelling in both codes. Important here is that the phase and magnitude of the tensions is comparable in with the linear buoyancy model.

This behavior changes if the local buoyancy model is included. Here, the amplitude of the tension from mooring line 2 increases significantly compared to the QB Lin simulations. For the mooring lines 1 and 3, the effective amplitude of the tension oscillations gets reduced due to an additional oscillation that is shifted in phase. These differences can be attributed to the different response pattern in heave and pitch of the OC4 model when the local buoyancy is used. Figure 43 and Figure 44 show the relevant DOFs and mooring line tensions for the regular sea state with H = 8 m and T = 12 s. It can again be seen that the response of QB Lin is comparable to OF in both the substructure dynamics and the tensions of the mooring lines.

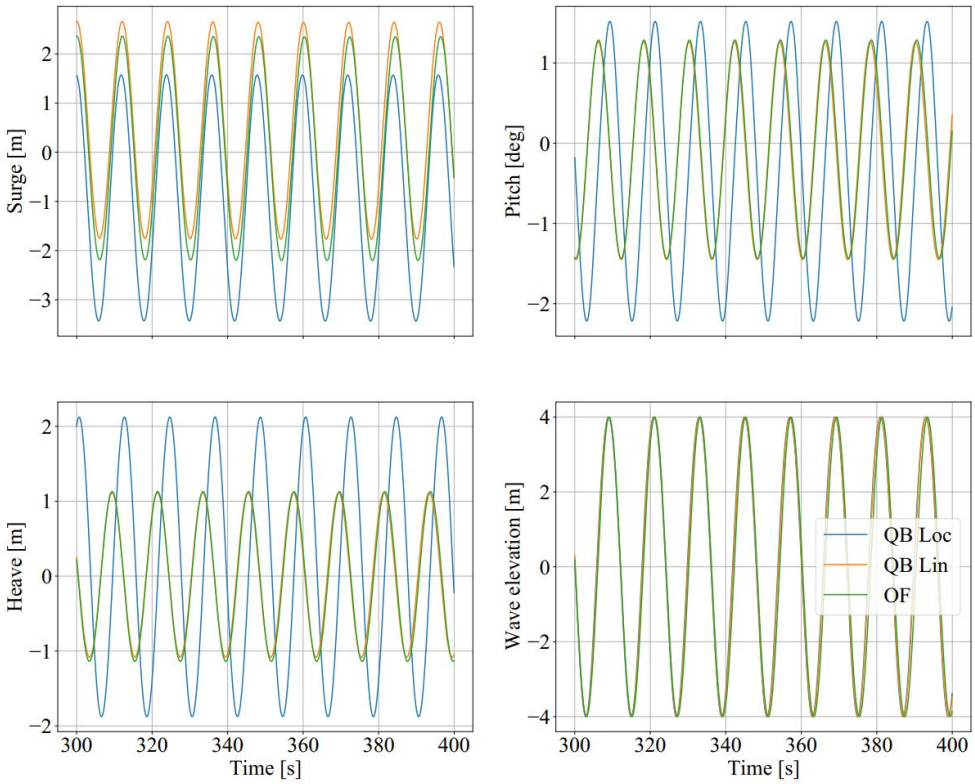

Figure 43: Relevant DOFs and wave elevation for regular sea state with H = 8 m and T = 12 s.

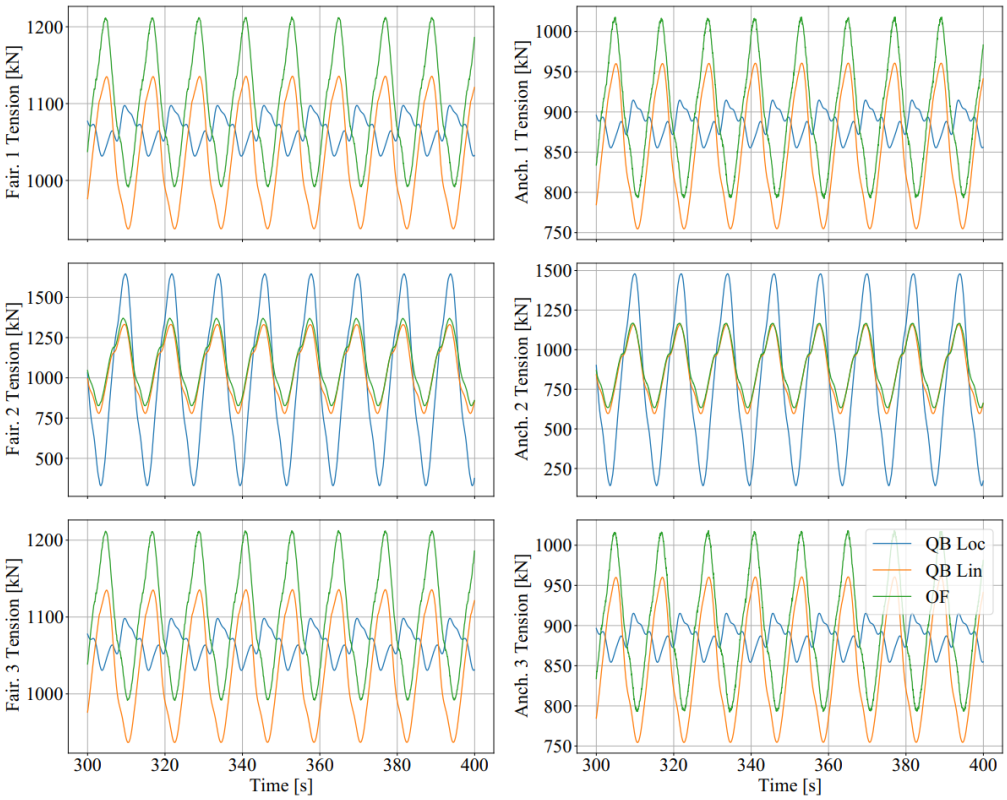

Figure 44: Mooring line tensions for regular sea state with H = 8 m and T = 12 s.

The response of the substructure changes even more drastically if the local buoyancy model is used for this test case. In Figure 43 it can be seen that the mean surge displacement of the QB Loc simulations is now negative compared to the positive mean surge displacement of the QB Lin simulations. Furthermore, the heave and pitch DOF have a larger amplitude compared to the QB Lin simulations and there is again a positive phase shift.

The effects on the mooring line tensions can be seen in Figure 44. In this figure, it can be clearly seen that the tension of the mooring line 2 is significantly affected for this test case. The amplitude of the oscillation is more than doubled in the QB Loc simulations compared to the QB Lin simulations.

Irregular Wave Tests

The OC4 LPMD model was also validated for irregular wave sea states. Six random sea states with a JONSWAP spectrum with H_s = 6 m, T_p = 10 s and γ=3.3 were used. The simulation length was 1200s and the first 400s were not considered in the analysis to discard initial transient effects. Again, no aerodynamic loads were considered in these cases and the wave propagation direction was chosen to be aligned with the positive surge direction. Additionally, no wave stretching model and no second order wave forces were included in the simulations. The response of the turbine model was done in a statistical manner by comparing the averaged PSDs of the DOFs.

It could be seen in the regular wave validation tests, the buoyancy model has an important effect on the substructure response and the mooring line tensions. For these calculations, the linear buoyancy model was used in QB. Although the local buoyancy calculation is deemed more accurate, the linear model was chosen to allow for a better comparison between OF and QB. In addition, the mooring system was also simulated using linear matrices in both codes. It was chosen to do this so that only the radiation forces, the wave excitation and diffraction forces as well as the quadratic drag forces from the Morison equation were the sole sources of loading. The mooring system is considered validated based on the validation tests done beforehand.

Figure 45 shows the averaged PSDs of all six DOFs for the irregular sea states. In this figure, the results from three different simulation setups are shown. The original OC4 LPMD model in QB and OF is labeled accordingly in this figure. Additionally, the results QB MSL are also presented in this figure. In the latter simulation setup, the quadratic forces of the Morison equation are calculated considering that the Morison element are wetted up to the mean sea level. This effectively neglects the local wave elevation when calculating the wetted surface of the substructure that will be considered for the Morison drag calculations. This approach is the one implemented in OF. In contrast, QB considers the local wave elevation (incl. wave stretching) to determine the wetted surface of the elements and apply the Morison forces. See Section 3.2.2 for more details. The setup QB MSL was thus chosen to have a simulation setup that matches the OF modelling.

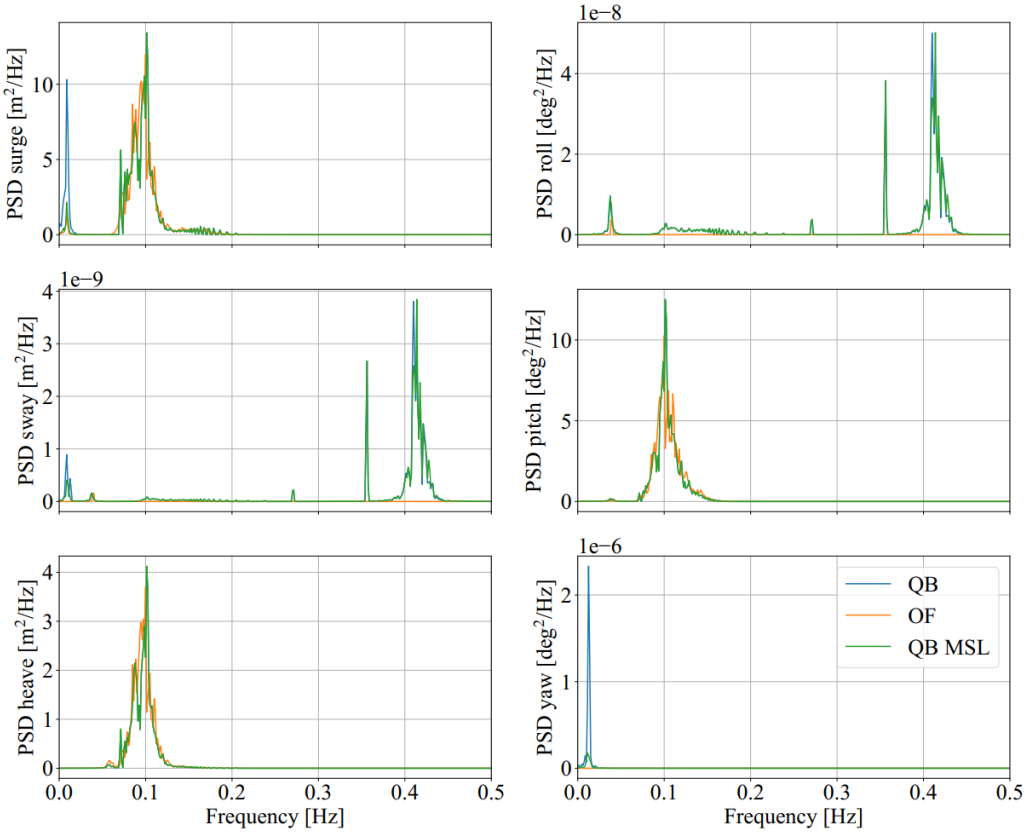

Figure 45: Averaged PSDs of all DOFs of the OC4 LPMD model for the irregular sea state with Hs = 6 m, Tp =10 s and γ= 3.3.

It can be seen in Figure 45 that the averaged PSD of all DOFs are very similar between the OF and QB simulations. There is a distinct difference at the low frequency regime of the surge DOF. The peak corresponding to the surge eigenfrequency is significantly larger in the QB simulations compared to the OF simulations. Notably, if the QB simulations are changed to consider the wetted surface up to the mean sea level (QB MSL), the difference in the peak at the surge eigenfrequency vanishes.

This phenomenon can be explained as follows. By considering the Morison drag calculations up to the local wave elevation only, there will be a net positive drag force in the surge direction. This is because as the wave particles retract during the trough of the wave, less surface will be wetted and less drag force will act on the substructure compared to the case where the substructure sees a wave crest. In the latter case, the wetted surface will encompass up to the mean sea level (no wave stretching). The irregular sea state will include time periods where the wave heights are large and time periods where the wave heights are small. The former scenario leads to high average mean surge forces while the latter scenario to low mean surge forces. The restoring forces from the linear mooring system will therefore let the OC4 model oscillate at its surge eigenfrequency when the average surge force is temporarily small. This non-linear phenomenon cannot happen if the wetted surface is considered constant at all times.

Second-Order Wave Excitation Forces

Second-order hydrodynamic loads play an increasingly important role for semi-submersible offshore structures such as the OC4 model. Duarte and Jonkman even state in [8] that the floater response is dominated or at least impacted at the same order of magnitude by the second order hydrodynamic loads as by their first order relatives. Bearing this in mind, a first evaluation of the implementation of the second-order wave load module, described in Section 3.5.2 seems reasonable on the OC4 platform. In the following, the force spectra of the second order wave loads acting in all 6 DOFs on the OC4 model in irregular waves are presented. The previously used JONSWAP spectrum with H_s = 6 m, T_p = 10 s and γ=3.3 once again was utilised to create the uni-directional (from 0 deg) wave field. The utilised QTFs were computed in WAMIT and are identical between QB and OF. First, the results where the second order-loads were computed through the full QTF approach and second, where by the Standing formulation of Newman's approximation are presented.

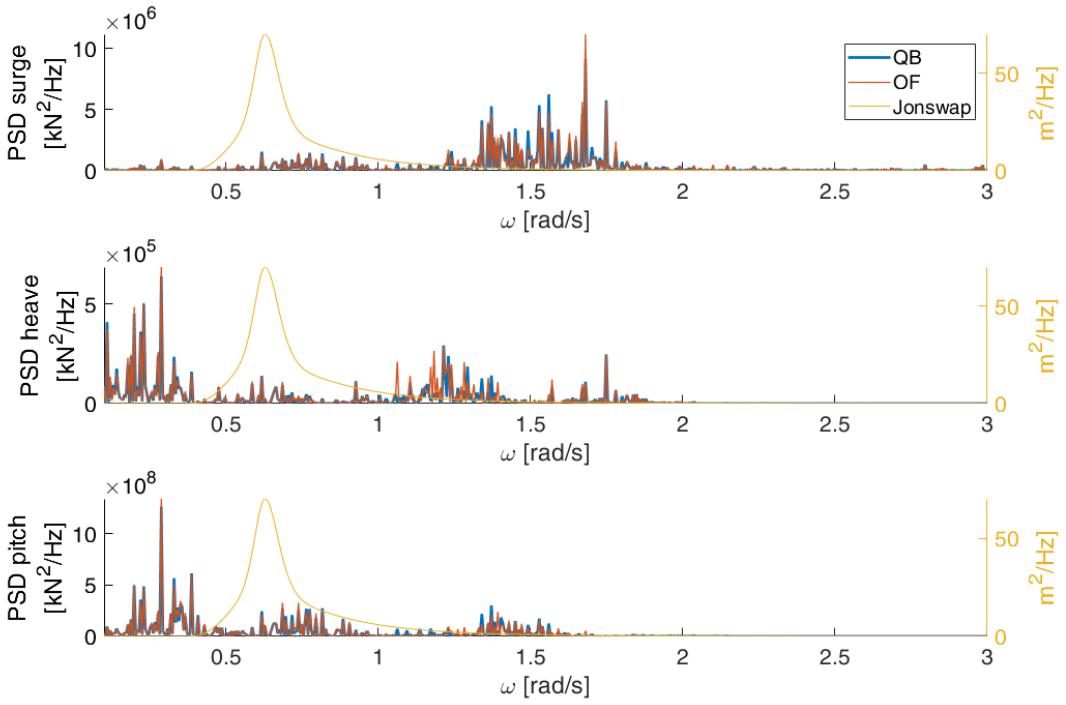

Figure 46 – Second-order hydrodynamic (sum- and difference-frequency) loads in irregular waves, full QTF

From Figure 46 one may clearly observe the similarity in the results between QB and OF. Both tools agree very well in the excited frequencies and also in the respective amplitudes. It can further be seen, that the sum- and difference – frequency loads clearly excite the floater outside of the present frequencies of the JONSWAP spectrum, especially in the pitch and heave DOF.

Figure 47 shows the result of the approximated second-order difference-frequency loads in all 6 DOFs. Again, strong similarities between the used simulation tools become evident. It also can be noted that the difference loads contain energy at frequencies lower than those present in the JONSWAP spectrum.

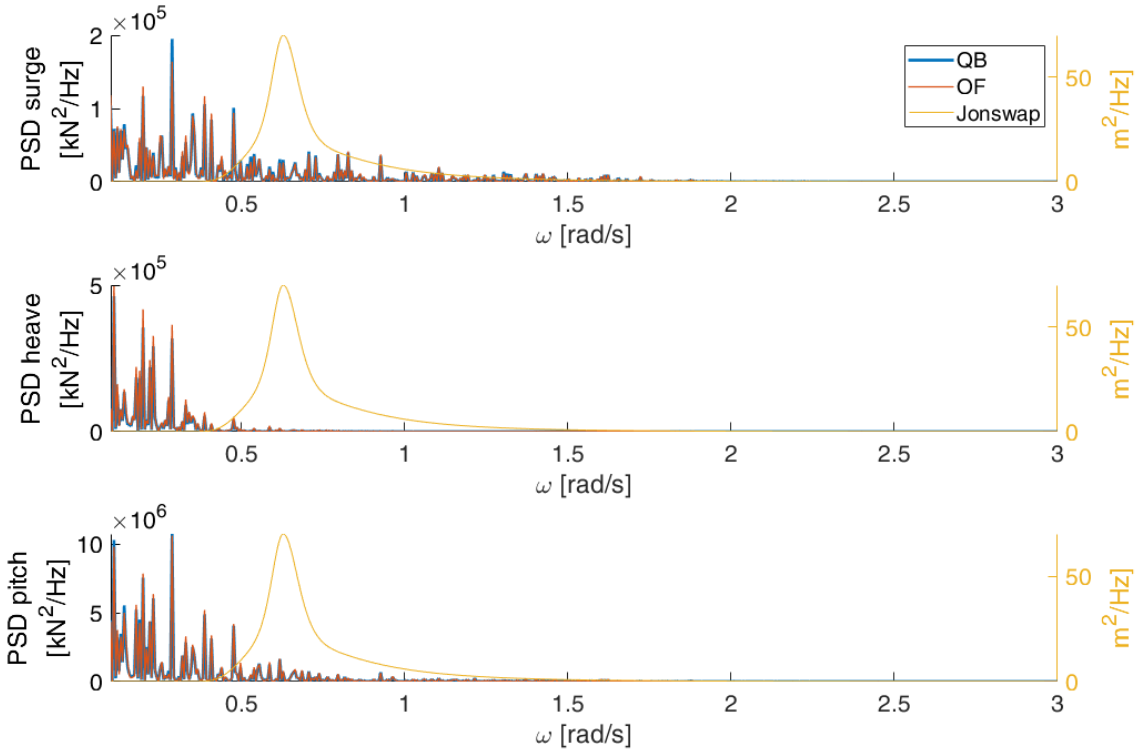

Figure 47: Second-order hydrodynamic difference-frequency loads in irregular waves, Newman approximation.

3.6.3 OC4 ME Model

The OC4 model was also modelled using the Morison equation only. The geometry of the model is the same as for the OC4 LPMD model (Figure 35). The difference between the models is the way the hydrodynamic loads are calculated (see Section 3.2.2 for details). The Morison equation modelling has the advantage of allowing distributed loading during the simulations and hence enable hydroelastic simulations. As a drawback, the hydrodynamic coefficients for the Morison equation are obtained empirically and are constant for all frequencies. This can lead to modelling inaccuracies compared to the LPMD approach, where the radiation, diffraction and excitation matrices are frequency dependent. The hydrodynamic coefficients for the OC4 ME model were taken from [2].

Similar to the previous sections, the OC4 ME model was tested in a series of cases to validate the full Morison model. The test cases include decay tests, regular wave tests and irregular wave tests. Again, the OC4 ME model was considered rigid for these test cases in order to validate the hydrodynamic models. The elasticity will be included in the next subsection.

Free Decay Tests

The first test cases were again free decay tests with still water. To validate the full Morison equation present in the OC4 ME model, an equivalent ME model was setup in OF. The additional hydrodynamic

coefficients were taken from [9]. According to this reference, the ME model in OF is not able to account for distributed buoyancy. Hence, a linearised buoyancy similar to the one from the LPMD was used in the OF calculations.

Figure 48 – Figure 50 show the time series of the surge, heave and pitch decay tests. It can be seen that the models in both codes show a very similar decay behavior. Again, there is a small offset in the heave position due to the different buoyancy models. Also, if comparison is made with the free decay test of the OC4 LMPD model (Figure 36 and Figure 37), it can be seen that the oscillations damp out more slowly in the decay tests with the OC4 ME model. This is because the OC4 ME model does not have radiation damping forces which act as an additional linear damping term.

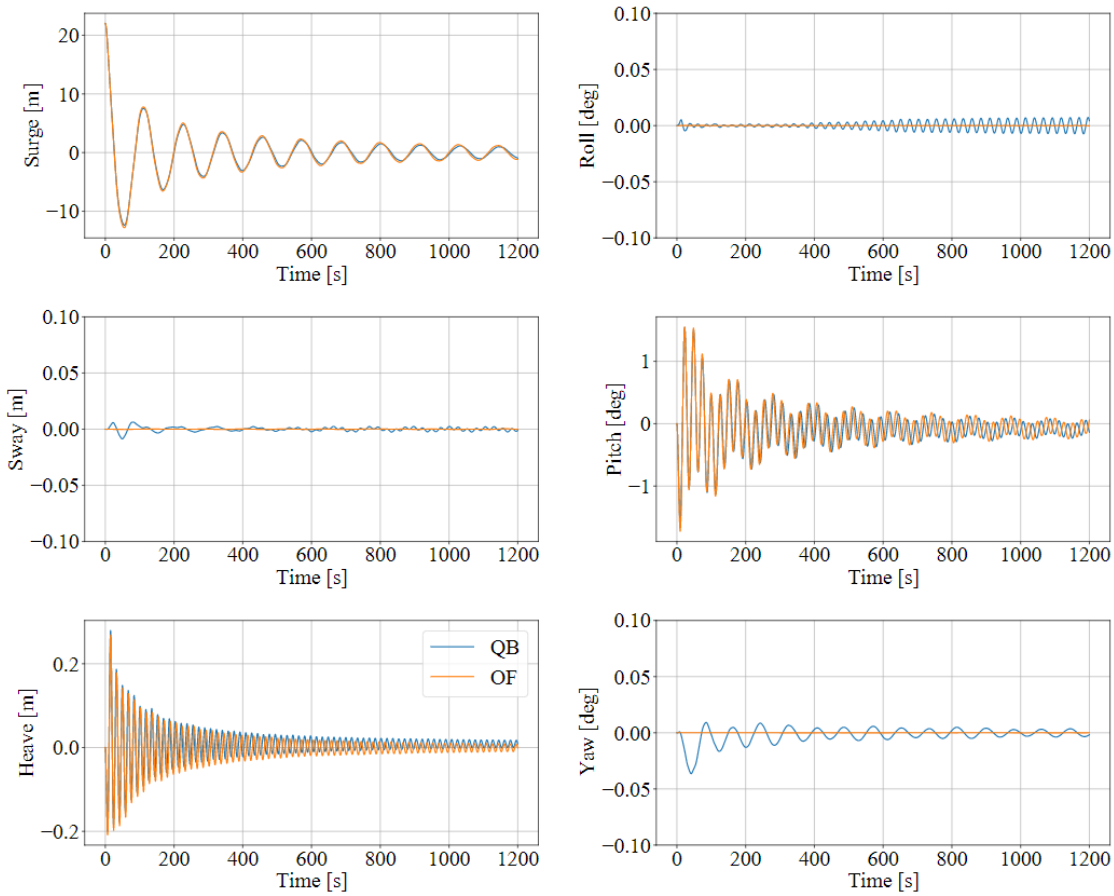

Figure 48: Time series of the surge decay test for the OC4 ME model.

Figure 51 shows the numerical relative values of the eigenfrequencies and damping coefficients of the decay tests for the surge, heave, pitch and yaw DOFs. It can be seen in this figure that the values for the frequencies and damping coefficients are very similar in both codes. There seems to be a discrepancy in the eigenfrequency of the surge DOF. This difference comes from the method used to determine the eigenfrequency. For the surge DOF, the numerical value of the eigenfrequency is low and it is therefore close to the frequency resolution used to determine it. In OF and QB, the peaks in the frequency transform of the signal were shifted in the frequency range by one resolution point. This already accounted for the difference seen in Figure 51. Visual inspection of Figure 48 already gives an empirical proof that the frequencies of the surge decay test are very similar.

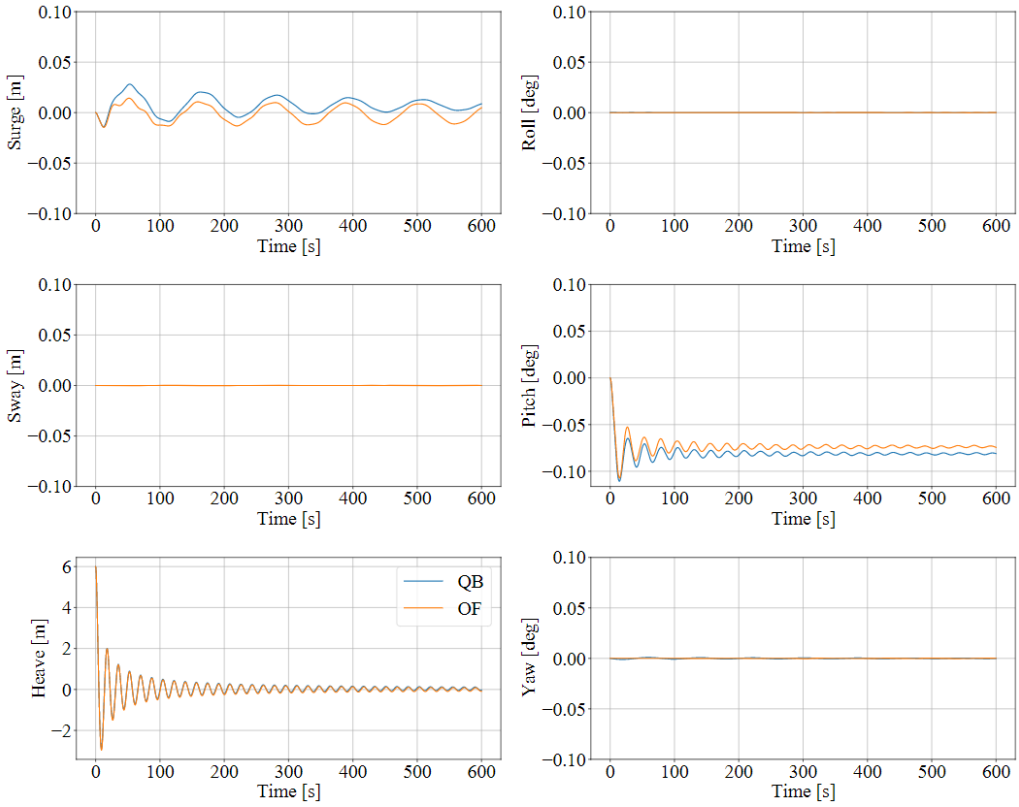

Figure 49: Time series of the heave decay test for the OC4 ME model.

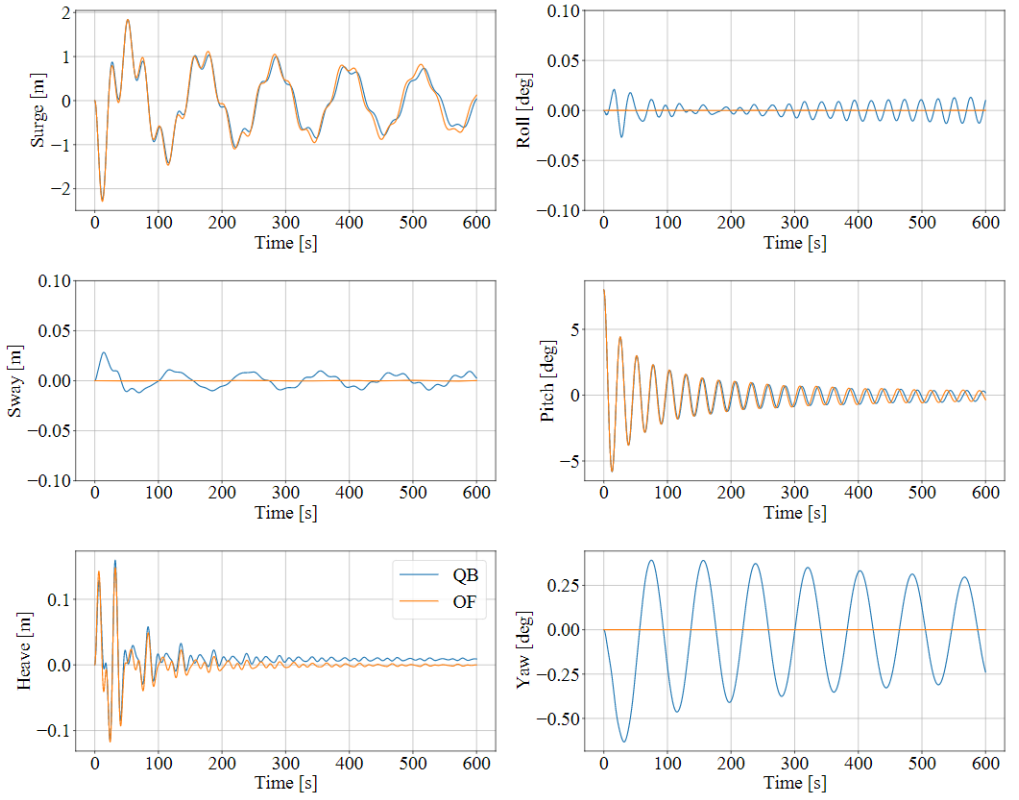

Figure 50: Time series of the pitch decay test for the OC4 ME model.

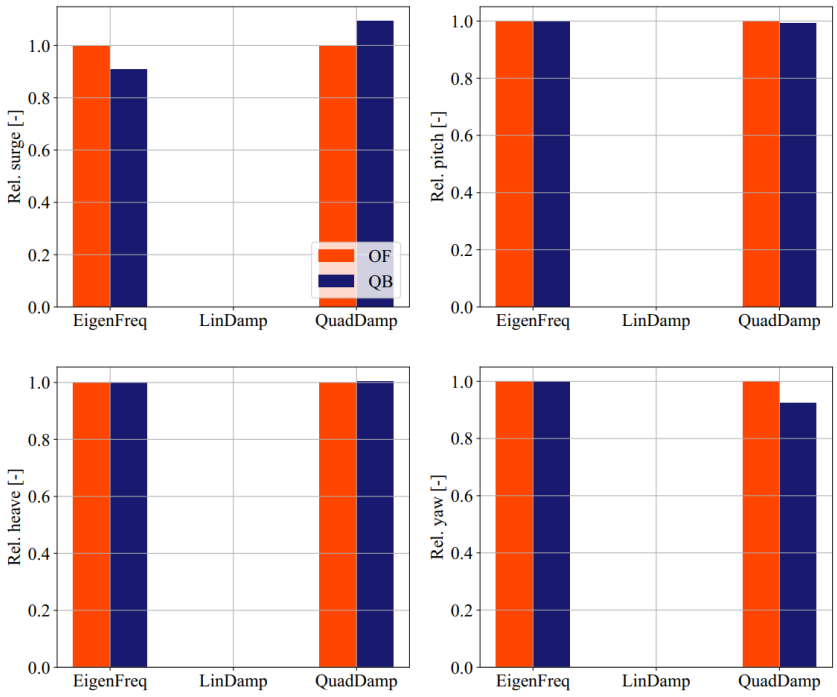

Figure 51: Eigenfrequencies and damping coefficients of the OC4 ME decay tests

Free decay tests were also carried out for the yaw DOF and demonstrates excellent agreement with OF. This has been omitted here for brevity and is included in Appendix A1.3.

Regular Wave Tests

The OC4 ME model was also validated and tested in regular wave tests. As with the OC4 LPMD model, two regular wave tests were considered: one wave with H = 6 m and T = 10 s and another wave with H = 8 m and T = 12 s. For these cases, the OC4 ME was adapted to have a linearised buoyancy model and a linearised mooring system model. Additionally, the wetted surface was considered to go until the mean sea level instead of the local wave elevation. This was done to better compare the QB model with the one present in the OF calculations. From the previous test cases, one can consider the buoyancy and mooring models validated. By aligning the modelling considerations between OB and OF, one can better validate the full Morison model developed in QB.

Diffraction forces will play a role for Morison elements that have a diameter larger than a fifth of the wavelength of the incoming wave [10]. For the OC4 ME model, this would be relevant for the large base and upper columns if the turbine operates at low sea states [2]. In QB, the full Morison model can be extended with the MacCamy-Fuchs correction to take into account the diffraction effects [11].

The regular wave test cases considered three sea states: the first one characterised by H = 0.67 m and T = 4.8 s, the second by H = 6 m and T = 10 s and the third by H = 8m and T =12 s. Again, the wave direction was aligned with the positive surge direction. According to [2], the diffraction forces will be relevant for the first sea state.

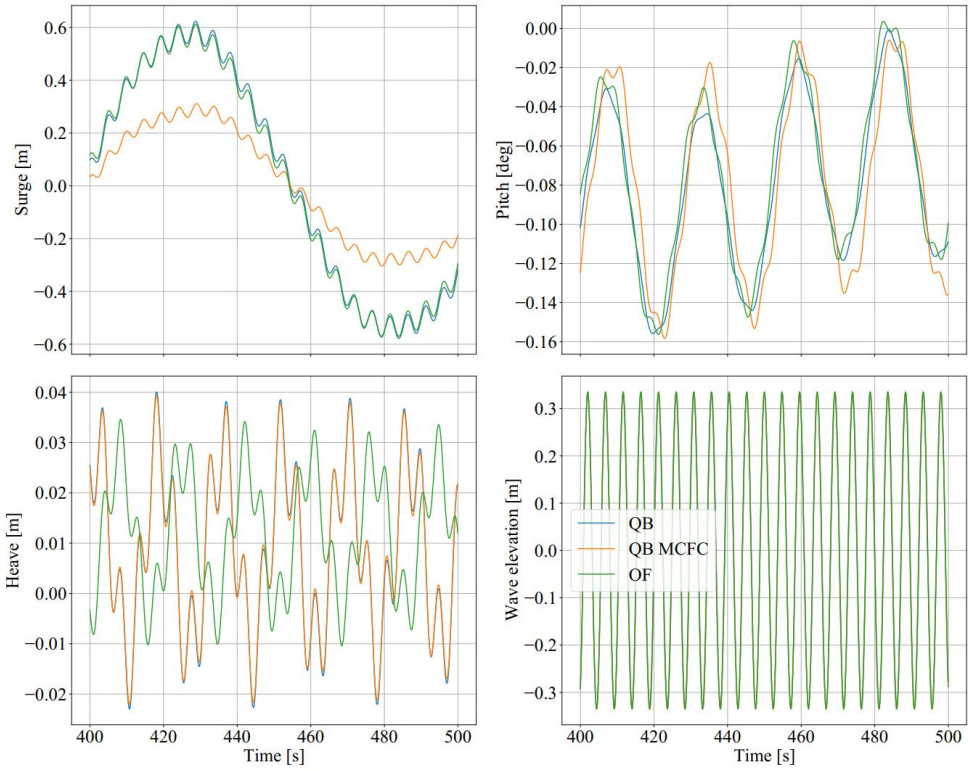

Figure 52: Relevant DOFs and wave elevation for regular sea state with H = 0.67 m and T = 4.8 s. QB MCFC = QB with MacCamy-Fuchs correction.

Figure 52 - Figure 54 show the surge, pitch and heave DOFs and the wave elevation for the three regular sea states. It can be seen in these figures that the results form OF and QB align fairly well in all three sea states. There are some small differences in the heave response in all three cases. When the MacCamy-Fuchs correction is enabled in QB, it can be seen that especially the surge DOF is affected in Figure 52 and Figure 53. For the sea state with the smallest wave height, the largest differences between the models with and without the MCFC are seen. For larger wave heights (Figure 53), there are still some differences between the calculations with and without MCFC. These differences practically vanish for the largest wave height case (Figure 54). This qualitative behavior corresponds to the expected behavior that the MCFC mostly affects sea states where the diameter of the Morison element is comparable to the wave length of the incoming wave.

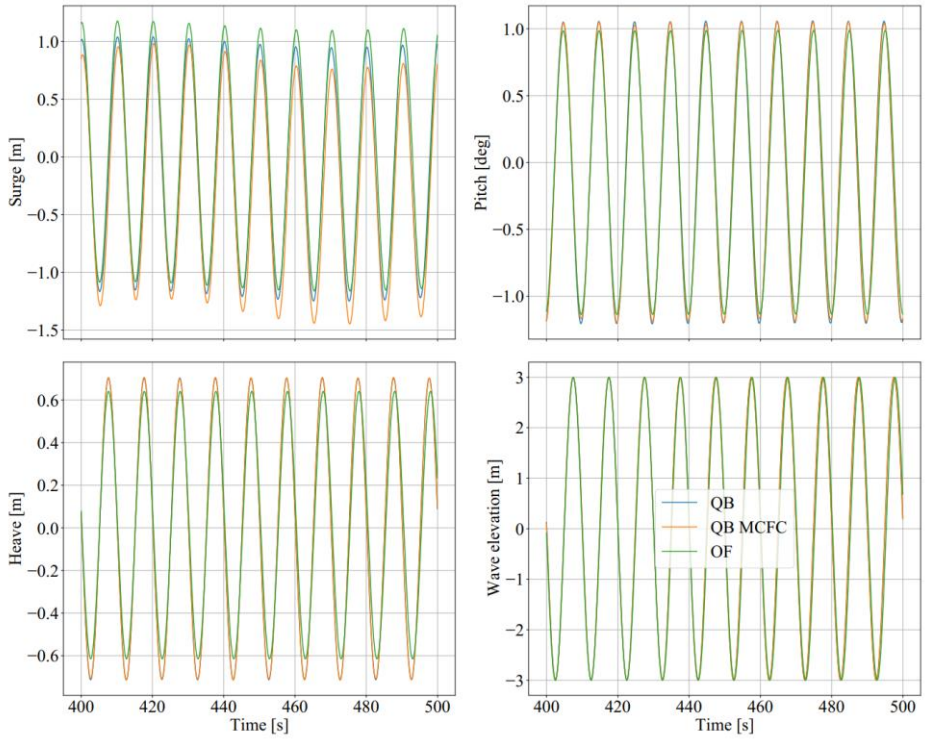

Figure 53: Relevant DOFs and wave elevation for regular sea state with H = 6 m and T = 10 s. QB MCFC = QB with MacCamy-Fuchs correction.

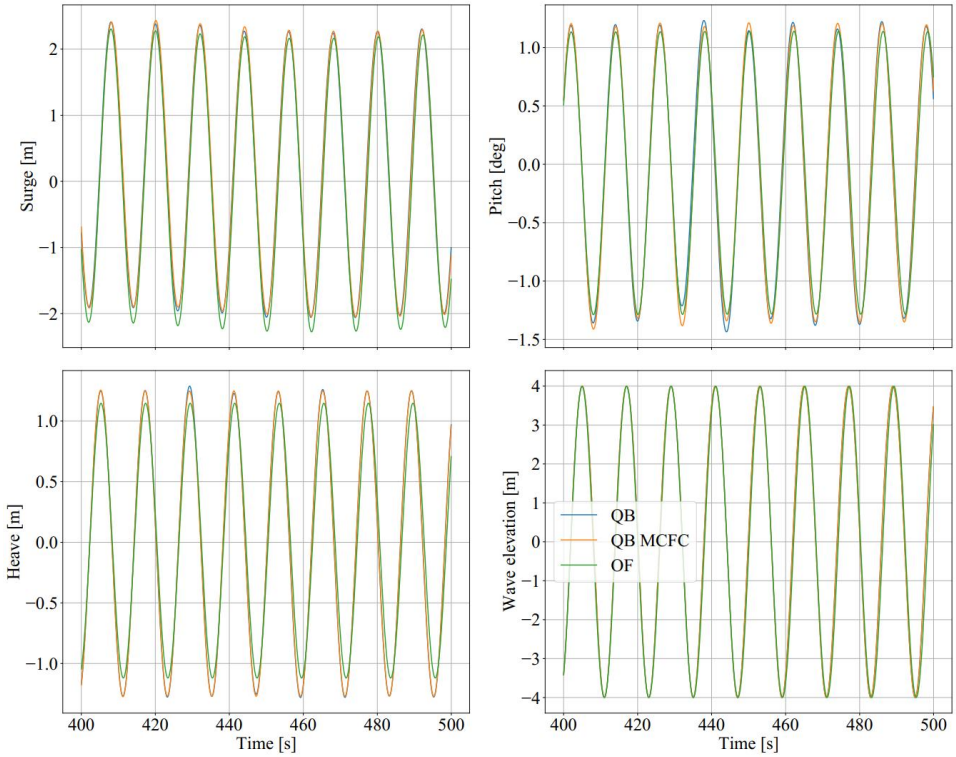

Figure 54: Relevant DOFs and wave elevation for regular sea state with H = 8 m and T = 12 s. QB MCFC = QB with MacCamy-Fuchs correction.

Irregular Wave Tests

The OC4 ME was also tested in sea states with irregular waves and compared to the results from OF simulations. As with the OC4 LPMD model, six stochastic sea states were used with a JONSWAP spectrum (H_s = 6, T_p = 10 s, γ = 3.3) and compared the averaged PSD of all DOFs. To have a good alignment of the modeling assumptions between QB and OF, a linear buoyancy and a linear mooring model were again used. Also, the wetted surface was assumed to go until the mean sea level and no MCFC was used in the QB simulations. For the irregular wave tests, the wave direction was aligned with the positive surge direction and no aerodynamic loads were considered.

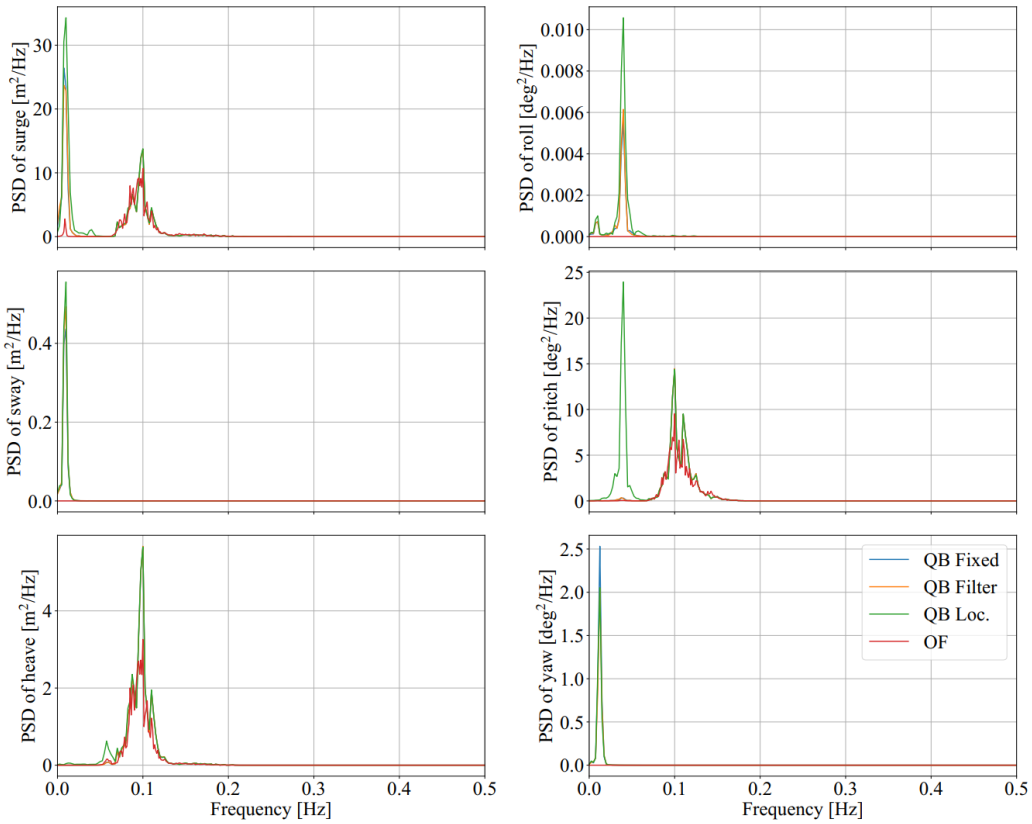

Figure 55: Averaged PSDs of the irregular wave test cases with the OC4 ME model.

The comparison was done in a statistical manner by comparing the six-simulation-averaged PSD for the six DOFs. Figure 55 shows the results of the irregular sea state test cases. It can be seen that the responses of the OF and QB simulations generally agree well. For the QB simulations, simulations with the three ME implementation options (see Section 3.5.3) were considered. The first option, QB Loc., considered the instantaneous local position of the Morison elements to calculate the water particle kinematics. The second option, QB Filter, considered the low-pass filtered position of the Morison elements to determine the water particle kinematics. The third option, QB Fixed, considered the fixed initial position of the Morison elements for the kinematic calculations. The last option is also implemented in OF [7].

It can be seen in Figure 55 that all simulations have a comparable PSD behavior for the wave excitation frequencies (around 0.1 Hz). The higher peaks in the heave and pitch DOFs come from the higher response of the OC4 ME model to wave excitation forces around these frequencies (Figure 53). The strongest

differences are seen for the QB Loc. and OF calculations in the low frequency range. The QB Loc. calculations show a peak in the eigenfrequencies of the pitch and surge DOFs while the OF calculations do not. This nonlinear response in pitch disappears for the QB Filter and QB Fixed simulations. It can therefore be attributed to the local instantaneous approach when calculating the water kinematics. The surge DOF still shows a peak in the surge eigenfrequency even when filtered or fixed approach is used for calculating the water kinematics. Further investigation is required to fully understand this phenomenon.

3.6.4 Hydroelastic Simulations

The OC4 ME model was also modeled with fully elastic members. The elastic members, together with the full Morison equation at each element allow us to have fully hydroelastic simulations within QB. The structural properties of the individual elements were taken from [12].

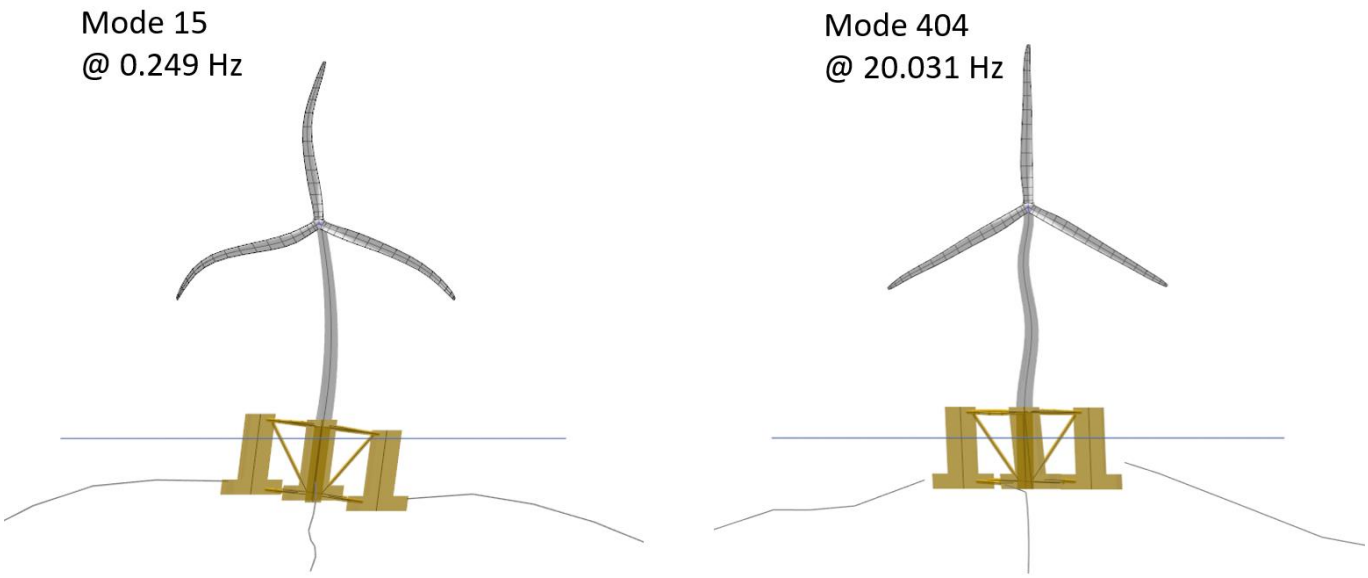

Figure 56: Two exemplary modes of the flexible OC4 ME model.

Figure 56 show two exemplary eigenmodes of the OC4 ME flexible model. Mode 15 on the left side has frequency 0.249 Hz and shows a combination of blade, tower and substructure deflections (exaggerated for visual effect). For the substructure, it is mainly the cross-braces that are deflecting. Mode 404 on the right side of Figure 56 has a frequency of 20.031 Hz. This mode shows a deflection of the three base and upper columns relative to each other. This could be considered as one of the eigenmodes of the substructure. It can be noted that there is also a tower deflection taking place in this mode. The high frequency of Mode 404 is also an argument for simulating the OC4 substructure as a rigid body if the local forces on the substructure are not required. The excitation frequencies from wind and waves are significantly lower than the eigenfrequencies of these modes. It can also be noted that both modes shown in Figure 56 also include the deflection of the mooring cables. All flexible members are taken into account when performing the eigenmode analysis within QB.

To demonstrate the hydroelastic capabilities of QB, the flexible OC4 ME model was simulated in a regular sea state with H = 6 m and T = 10 s. Again, no aerodynamic loads were applied on the turbine and the wave direction was chosen to coincide with the positive surge direction. The local loads for two locations were recorded: the lowest position of the main column and the connection point of the cross brace 1 with the upper column 1 (see Figure 57).

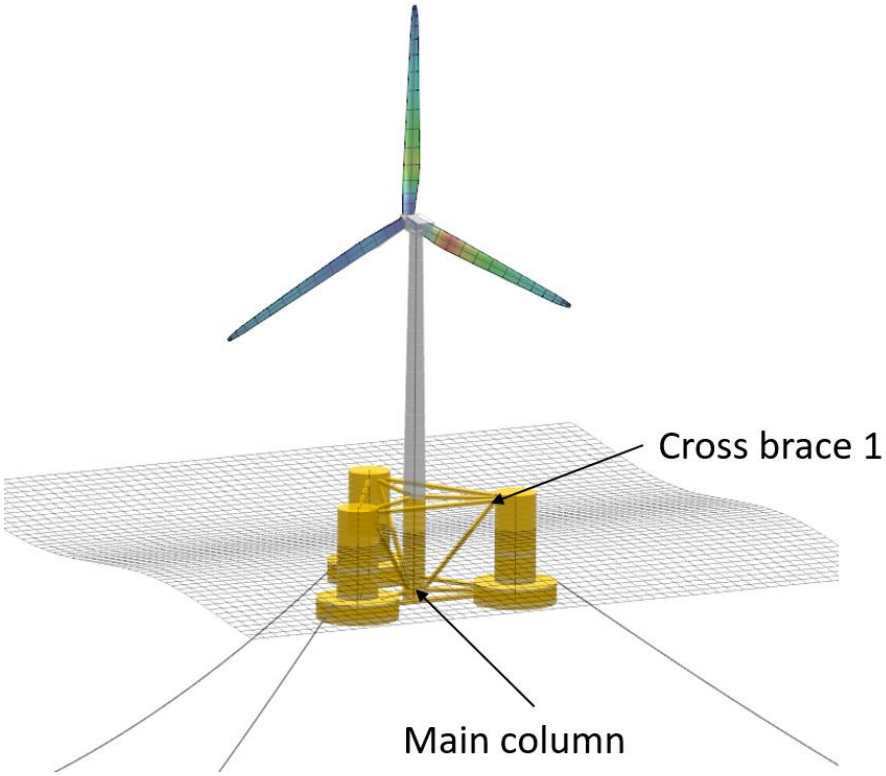

Figure 57: Load sensor locations for flexible OC4 ME calculations.

Figure 58 shows the local forces at the main column and the cross brace for the initial 400 s of the regular sea state simulation. It can be seen that the forces behave as expected. The source of the local forces at the main column bottom location arise mainly from the hydrodynamic and gravitational loads. The local force in the x-direction (surge) has an oscillatory behavior around 0 kN, which can be explained by the oscillatory nature of the hydrodynamic wave loads in surge direction. This also explains the small forces in the y-direction (sway) since no wave loads are acting in this direction. Finally, in z-direction (heave), the oscillatory wave loads have a non-zero mean value. This comes from the gravitational loads acting in the z-direction. These localised loads can be used to design the individual components of a floating wind turbine substructure.

Figure 59 shows the corresponding local deflections of the main column and cross brace. It can be seen in this figure that the substructure deflections at these positions are very small, not even reaching 1 mm. This comes from the large stiff structures that make up the OC4 substructure. Figure 59 shows that the rigid substructure assumption made for this model is a valid. This can change if flexible substructures are considered for floating wind turbines, as is shown in the next subsection. Having hydroelastic modelling capabilities becomes crucial if one wishes to model and simulate flexible substructures.

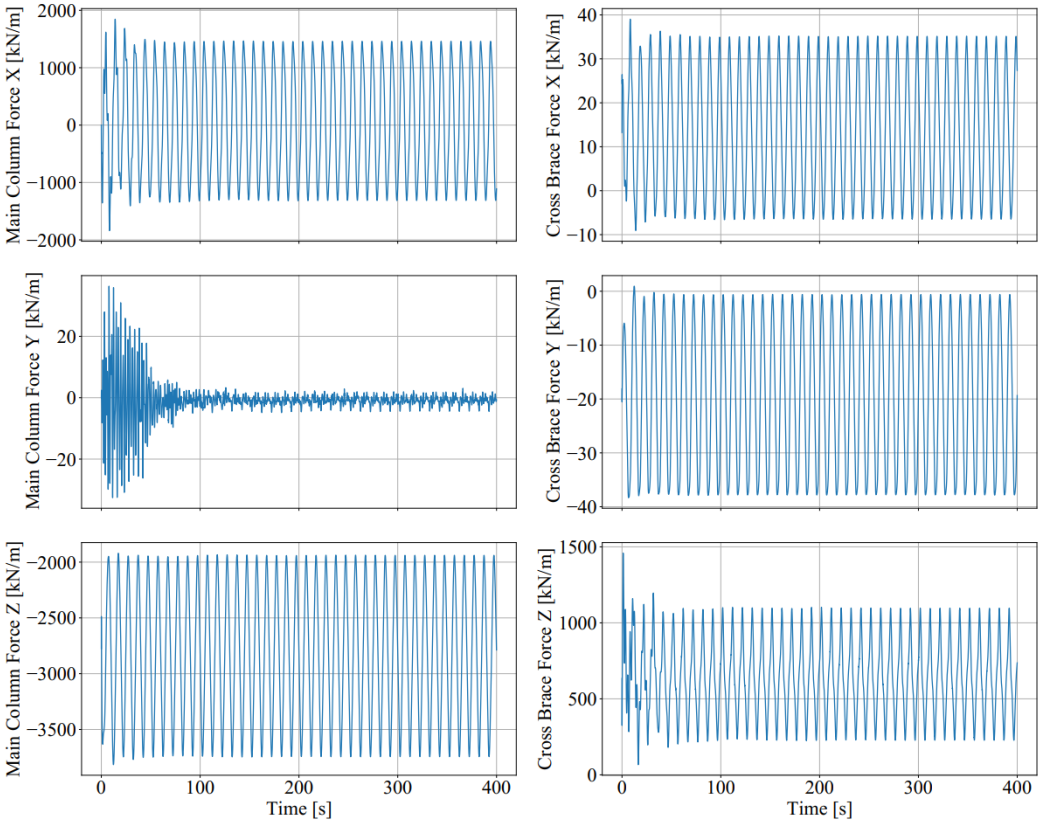

Figure 58: Local forces at two locations of the OC4 ME flexible substructure.

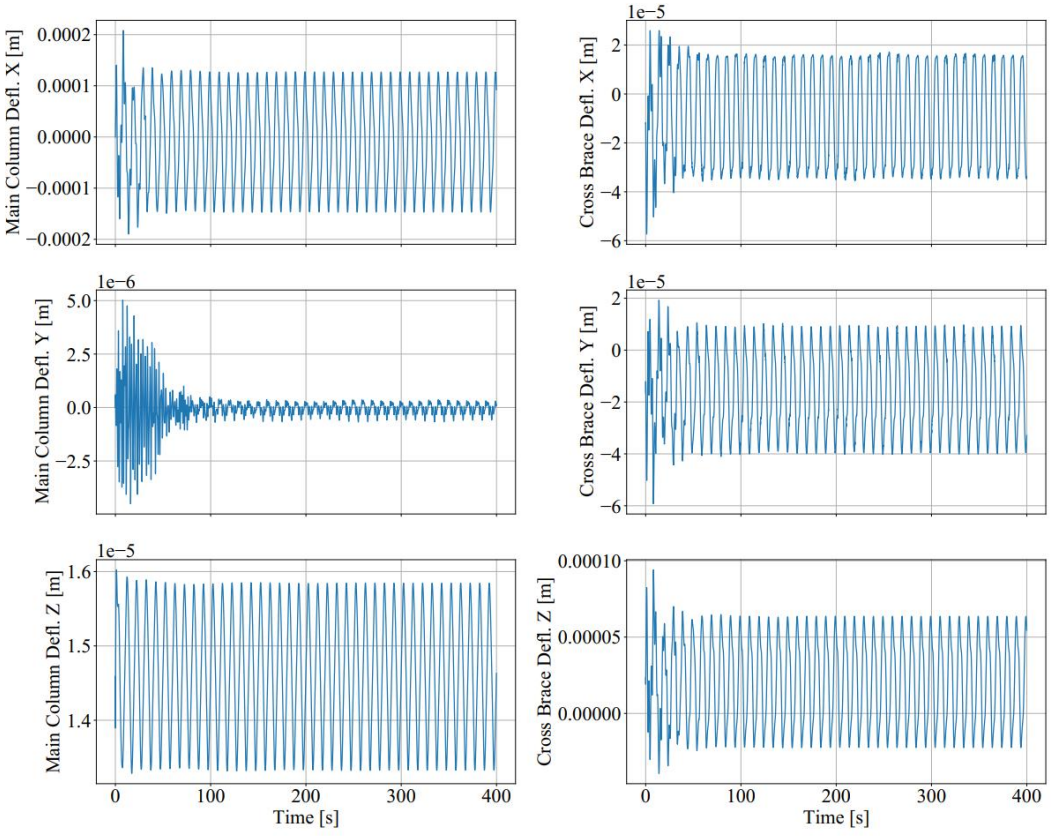

Figure 59: Local deflections at two locations of the OC4 ME flexible substructure.

Exemplary Hydroelastic Models

The hydroelastic capabilities of QB can be used to model also more complicated and flexible substructure geometries. In Figure 60, a hydroelastic model of a 10 MW turbine mounted on an up-scaled TetraSpar substructure is shown [13]. The modelling of this substructure is particularly challenging because it features a flexible suspension between the upper floater structure and the lower keel. Within QB, this suspension system can be modelled as a cable element similar to the mooring system (Section 3.2.3). The TetraSpar model shown in Figure 60 is composed of flexible Morison elements and QB is therefore capable of accurately calculating the local loading on each element even when the substructure model is highly deflected. An example of this is shown on the right hand side of Figure 60. This extreme roll position is unlikely to happen in reality, but being able to simulate such conditions in QB is a good example of the modelling capabilities of the tool.

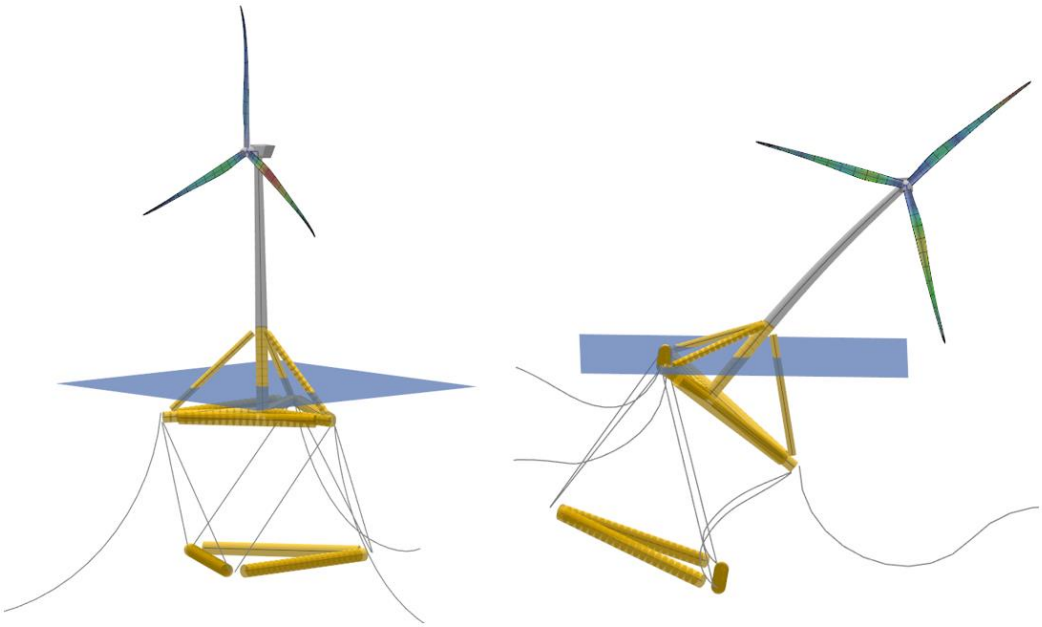

Figure 60: Hydroelastic model of a 10MW turbine on an up-scaled TetraSpar substructure

3.6.5 References

[1] Jonkman, J. and Musial W., Offshore Code Comparison Collaboration (OC3) for IEA Task 23 Offshore Wind Technology and Deployment, Technical Report No. TP-5000-48191, NREL, 2010.

[2] Robertson, A. et al., Definition of the Semisubmersible Floating System for Phase II of OC4, Technical Report No. TP-5000-60601, NREL, 2014.

[3] OpenFAST, available at: https://github.com/OpenFAST/openfast/releases, last access: 10 Nov 2021.

[4] Robertson A. et al., Definition of the OC5 DeepCwind Semisubmersible Floating System, available at: https://a2e.energy.gov/data/oc5/oc5.phase2/attach/oc5.phase2.model.definition-semisubmersible-floating-system-phase2-oc5-ver15.pdf, last access: 11 Nov 2021.

[5] Hall, M. and Goupee, A., Validation of a lumped-mass mooring line model with DeepCwind semisubmersible model test data, Ocean Engineering, 104, pp. 590-603, 2015.

[6] DNV, Environmental Conditions and Environmental Loads, Recommended Practice DNV-RP-C205, 2014.

[7] HydroDyn User Guide and Theory Manual, available at: https://raf-openfast.readthedocs.io/en/docs-all/source/user/hydrodyn/index.html, last access: 16 Nov. 2021

[8] Duarte, T. and Sarmento, JNA., Jonkman, J. Effects of Second-Order Hydrodynamic Forces on Floating Offshore Wind Turbines, 32nd ASME Wind Energy Symposium, 10.2514/6.2014-0361.

[9] Wendt, F. et al., Verification of New Floating Capabilities in FAST v8, Proc. of AIAA SciTech 2015, 2015.

[10] Faltinsen, O. M., Sea Loads on Ships and Offshore Structures, Cambridge University Press, 1990.

[11] IEC Standard 61400-3-1, Wind energy generation systems – Part 3-1: Design requirements for fixed offshore wind turbines, 2019.

[12] HAWC2 OC4 Semisubmersible model, available at: https://www.hawc2.dk/download/hawc2-model, last access: 22 Nov 2021.

[13] Borg, M. et al., Technical Definition of the TetraSpar Demonstrator Floating Wind Turbine Foundation, Energies, 13, p. 4911, 2020.

4. CONCLUSIONS

With the increasing size of floating wind turbines, and for enabling the design and the optimization of the next generation of floating structures, structural flexibility along with hydroelastic effects need to be accounted for in engineering design software. This report presented the numerical developments implemented in the hydrodynamic module of QBlade Ocean, its coupling with the structural solver and preliminary results on the hydroelastic response of a floating wind turbine.

The verification and validation of the developments were presented for different case studies. A full Morison equation model and a Cummin's equation model were verified against OpenFAST. The full Morison equation model was verified for the spar-type OC3 floating wind turbine and the semi-submersible OC4 floating wind turbine. The Cummin's equation model was also verified in the case of the OC4 floating wind turbine where second-order wave loads were also accounted for via Quadratic Transfer Functions. All comparisons were based on free decay tests, regular and irregular waves. The performances of QBlade Ocean were shown to be equivalent to OpenFAST.

Finally, the Morison equation model was tested for a flexible OC4 platform. Preliminary results on the hydroelastic response of the platform under regular waves showed the hydroelastic modelling capabilities of QBlade Ocean.

The present document was a focus on the verification and validation of the hydrodynamic module of QBlade Ocean. Additional verification and validation work are planned in WP2 of the FLOATECH project. Additional floating wind turbine configurations as well as more complex design load cases with aerodynamic loads will be accounted for. A computational performance comparison against OpenFAST will be also carried out and reported in deliverable D2.2.

APPENDICES

A1 FREE DECAY TESTS

Additional free decay tests were carried out the supplement those in Sections 3.6.1, 3.6.2 and 3.6.3. These are shown here.

A1.1 OC3 LPMD Model

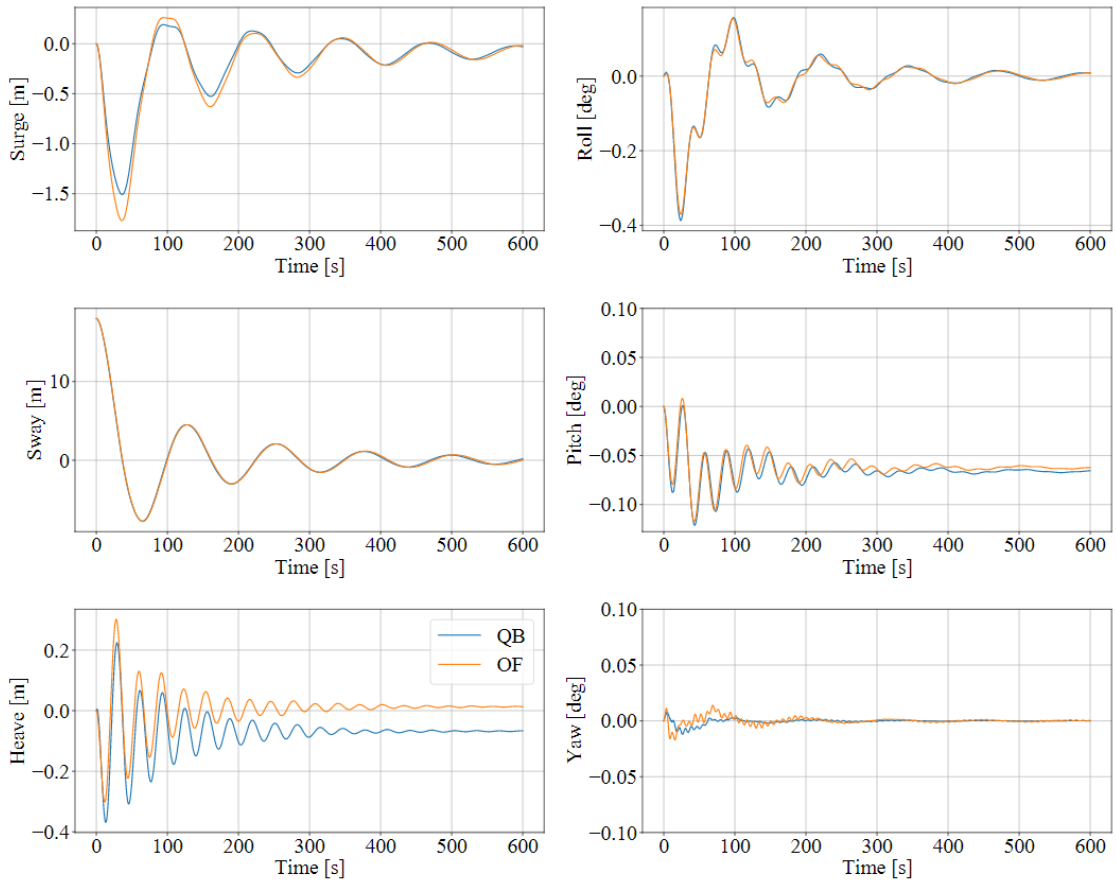

Figure 61: Time series of the sway decay test for the OC3 LPMD model.

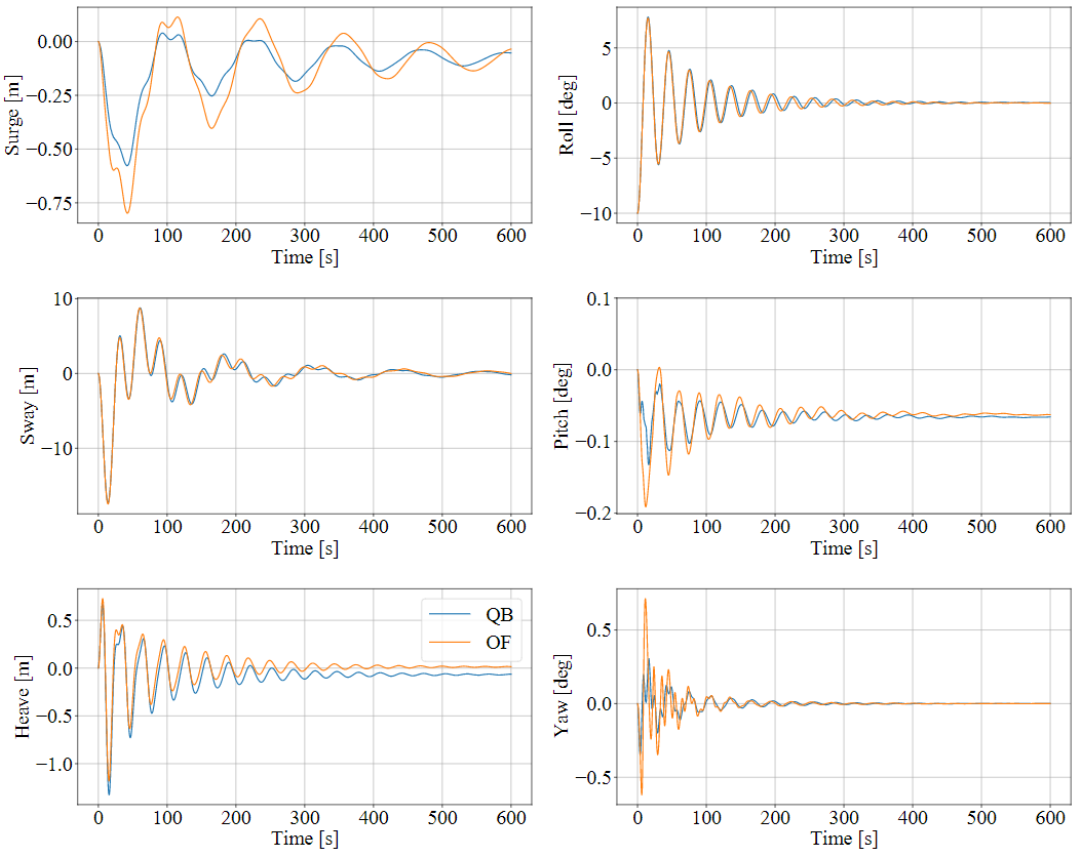

Figure 62: Time series of the roll decay test for the OC3 LPMD model.

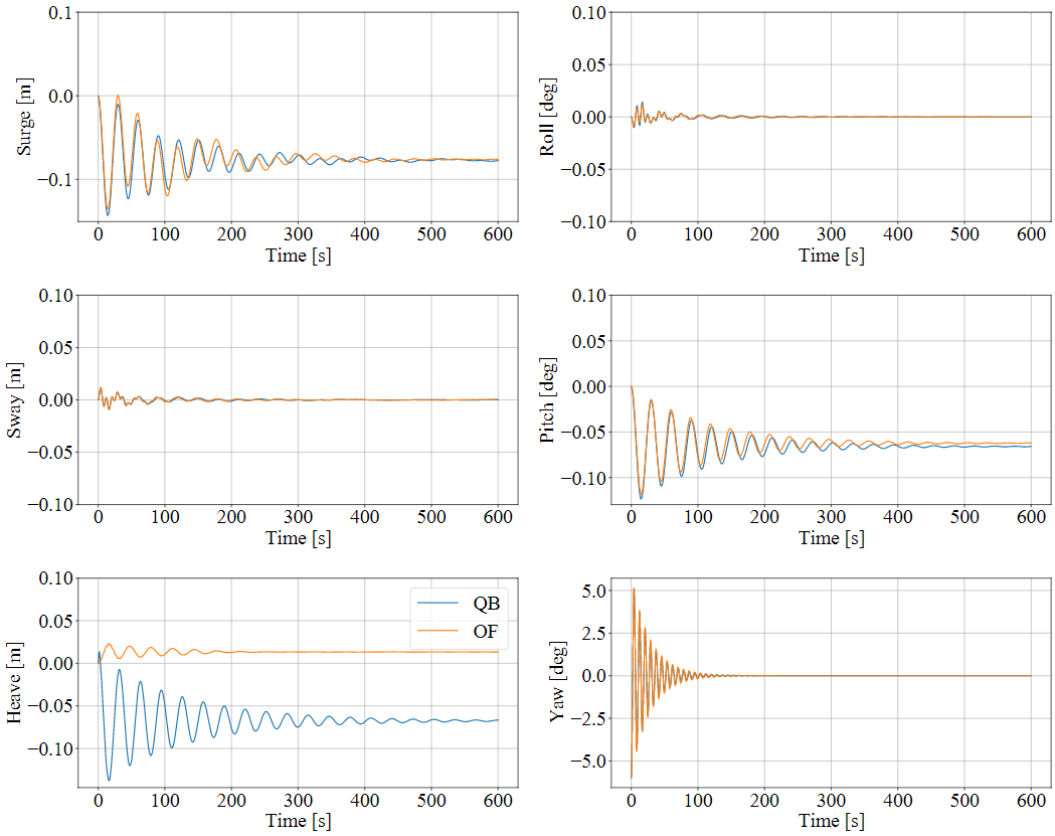

Figure 63: Time series of the yaw decay test for the OC3 LPMD model.

A1.2 OC4 LPMD Model

Only the heave decay test is shown here as it presents a case of interest. The full DOF decay tests were carried out for the OC3 geometry and have been shown above. As excellent agreement was seen here it was deemed superfluous to carry out these tests also for the OC4 geometry.

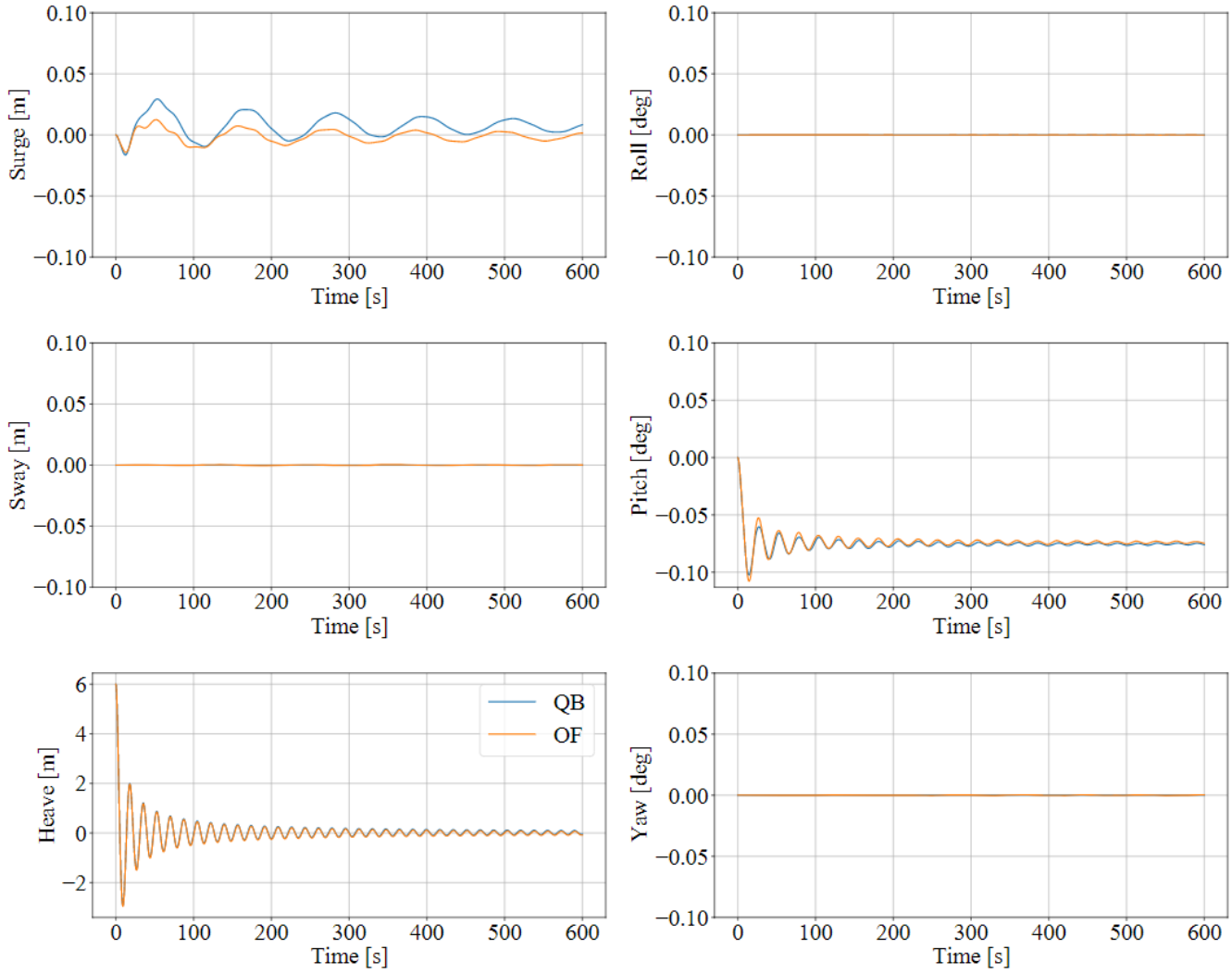

Figure 64: Time series of the heave decay test for the OC4 LPMD model.

A1.3 OC4 ME Model

Only the yaw decay test is shown here as it presents a case of interest. The full DOF decay tests were carried out for the OC3 geometry and have been shown above. As excellent agreement was seen here it was deemed superfluous to carry out these tests also for the OC4 geometry.

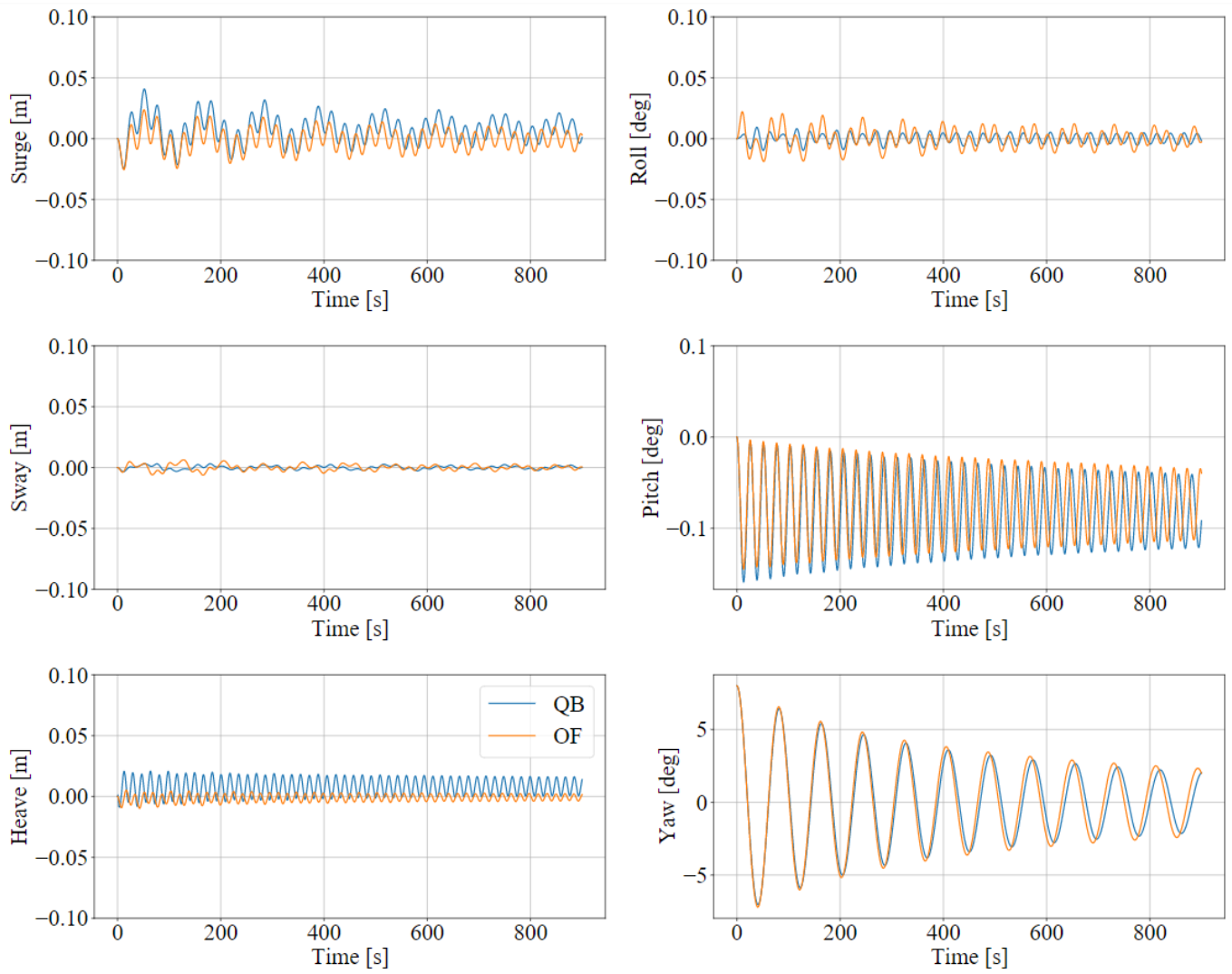

Figure 65: Time series of the yaw decay test for the OC4 ME model.